POLITECNICO
MILANO 1863

SCUOLA DI INGEGNERIA INDUSTRIALE
E DELL'INFORMAZIONE

POLITECNICO DI MILANO

School of Industrial and Information Engineering

Master of Science in Biomedical Engineering
for Cells, Tissues and Biotechnology

Hosting institution

Fondazione IRCCS Istituto Neurologico "Carlo Besta"

Cell Labeling Optimization for Quantitative ^{19}F-MRI Tracking in Glioblastoma Adoptive T-cell Therapy

Supervisor
Prof.ssa Francesca Baldelli Bombelli

Co-supervisor
Dr. Cristina Chirizzi
Prof.ssa Serena Pellegatta

Student
Cecilia Catacchio

Student ID
10928826

Academic Year 2025–2026

"Pensa alle tue cose preferite,
A tutto quello che vuoi diventare."

— "Fare ninna"

Abstract

Chimeric antigen receptor (CAR) T-cell therapy is among the most promising strategies in modern cancer immunotherapy. Although CAR-T therapies have achieved remarkable clinical results in hematological malignancies, their application to solid tumors such as "glioblastoma" remains limited by multiple biological and technological challenges. A critical gap is the lack of non-invasive methods to monitor the fate of therapeutic cells after infusion, including biodistribution, persistence, and capacity for tumor infiltration.

This thesis addresses this need aiming at developing fluorinated nanoparticles for labeling CAR-T cells, enabling their potential tracking by "fluorine-19 magnetic resonance imaging" (^{19}F-MRI). The approach relies on encapsulating a highly fluorinated molecular probe (PERFECTA: suPERFluorinatEd ContrasT Agent) within biodegradable poly(lactic-co-glycolic acid) (PLGA) nanoparticles stabilized with surfactants, including sodium cholate (NaC). Optimized fluorinated nanoparticles, designed to efficiently label CAR-T cells while preserving viability and cytotoxic function, were physicochemically characterized and showed preserved structural integrity and fluorine content in CAR-T cell-conditioned media, despite protein corona formation. This formulation was used to label human B7-H3-directed CAR-T cells, targeting an antigen widely expressed across nearly all glioblastoma subtypes. Flow cytometry confirmed preserved CAR-T cell viability (approximately 95%) and highly efficient nanoparticle uptake across the cell population (>99% NP-positive cells). Quantitative ^{19}F-NMR/MRI revealed a mean intracellular loading ranging from approximately $9,39 \times 10^{11}$ to $1,90 \times 10^{13}$ ^{19}F atoms per cell, markedly overcoming previously reported values for CAR-T cell labeling. This optimization enabled robust detection of labeled cells by ^{19}F-MRI, with a signal-to-noise ratio (SNR) exceeding the detection threshold by approximately five-fold.

Co-culture experiments with U-87 glioblastoma cells confirmed that nanoparticle labeling does not compromise CAR-T cytotoxic activity, with retained ability to eliminate tumor cells and a detectable ^{19}F signal throughout the observation period. These findings indicate that fluorinated PLGA nanoparticles constitute a non-toxic, promising labeling platform for CAR-T cells and for developing quantitative cellular tracking strategies by ^{19}F-MRI.

Beyond MRI tracking, the intracellular fate of nanoparticles was investigated by Raman imaging. From a translational perspective, this approach could be extended beyond CAR-T cells to other cell-based therapies, including stem cells and mesenchymal stem cells (MSCs), providing a versatile platform for non-invasive *in vivo* visualization of cell distribution, persistence, and fate, supplying critical information to more effective personalized immunotherapies.

Keywords: suPERFluorinatEd ContrasT Agent polymeric nanoparticles; CAR-T cell therapy; Glioblastoma; Fluorine-19 Magnetic Resonance Imaging (^{19}F-MRI).

Sommario

La terapia basata su cellule linfocitarie T dotate di recettore chimerico per l'antigene (CAR-T) rappresenta una delle strategie più promettenti dell'immunoterapia oncologica moderna. Sebbene le terapie CAR-T abbiano ottenuto risultati clinici straordinari nelle neoplasie ematologiche, la loro applicazione ai tumori solidi, come il "glioblastoma", è ancora limitata da numerose sfide biologiche e tecnologiche. Una delle limitazioni più critiche è la mancanza di metodi non invasivi in grado di monitorare il destino delle cellule terapeutiche dopo l'infusione, inclusi la biodistribuzione, la persistenza e la capacità di infiltrazione tumorale.

Questa tesi affronta tale problematica sviluppando nanoparticelle fluorurate per la marcatura delle cellule CAR-T, consentendo il loro potenziale tracciamento mediante "risonanza magnetica al fluoro-19" (^{19}F-MRI). L'approccio si basa sull' incapsulamento di una sonda molecolare altamente fluorurata (PERFECTA: suPERFluorinatEd ContrasT Agent) all'interno di nanoparticelle biodegradabili di poli(acido lattico-co-glicolico) (PLGA), stabilizzate con tensioattivi, tra cui sodio colato (NaC). Le nanoparticelle fluorurate ottimizzate, progettate per marcare in modo efficiente le cellule CAR-T, preservandone la vitalità e la funzione citotossica, sono state caratterizzate fisico-chimicamente e hanno mantenuto integrità strutturale e contenuto di fluoro in mezzi condizionati da cellule CAR-T, nonostante la formazione della corona di proteine. Questa formulazione è stata utilizzata per marcare cellule CAR-T umane dirette contro B7-H3, un antigene ampiamente espresso in quasi tutti i sottotipi di glioblastoma. L'analisi tramite citometria a flusso ha confermato una vitalità preservata delle cellule CAR-T (circa 95%) e un uptake altamente efficiente delle nanoparticelle nell'intera popolazione cellulare (>99% di cellule NP-positive). L'analisi quantitativa tramite ^{19}F-NMR/MRI ha evidenziato un carico intracellulare medio compreso tra circa $9,39 \times 10^{11}$ e $1,90 \times 10^{13}$ atomi di ^{19}F per cellula, superando nettamente i valori precedentemente riportati per la marcatura di cellule CAR-T. Tale ottimizzazione ha consentito un rilevamento robusto delle cellule marcate mediante ^{19}F-MRI, con un rapporto segnale/rumore (SNR) 5 volte superiore alla soglia di rilevazione.

Esperimenti di co-coltura con cellule di glioblastoma (U-87) hanno confermato che la marcatura con nanoparticelle non compromette l'attività citotossica delle cellule CAR-T, che mantengono la capacità di eliminare efficacemente le cellule tumorali e un

segnale ^{19}F-MRI persistente durante l'intero periodo di osservazione. Questi risultati dimostrano che le nanoparticelle in PLGA fluorurate rappresentano un simil-agente di contrasto non tossico e promettente per la marcatura delle cellule CAR-T e per lo sviluppo di strategie di tracciamento cellulare quantitativo mediante ^{19}F-MRI.

Oltre al tracciamento basato su MRI, è stato inoltre investigato il destino intracellulare delle nanoparticelle mediante imaging Raman.

Da una prospettiva traslazionale, questo approccio potrebbe essere esteso oltre le cellule CAR-T ad altre strategie di terapia cellulare, incluse le cellule staminali e le cellule staminali mesenchimali (MSCs), fornendo una piattaforma versatile per la visualizzazione non invasiva *in vivo* della distribuzione, della persistenza e del destino cellulare, e offrendo informazioni cruciali per lo sviluppo di immunoterapie personalizzate più efficaci.

Parole chiave: Agente di contrasto superfluorurato in nanoparticelle polimeriche; Terapia cellulare CAR-T; Glioblastoma; Risonanza magnetica al fluoro-19 (^{19}F-MRI).

Contents

List of figures

List of tables

Acronyms

^{18}FFDG	[^{18}F]fluoro-2-deoxy-D-glucose (fluorodeoxyglucose)
^{19}F-MRI	Fluorine-19 Magnetic Resonance Imaging
^{19}F-NMR	Fluorine-19 Nuclear Magnetic Resonance
ACT	Adoptive Cell Therapy
ALL	Acute Lymphoblastic Leukemia
BBB	Blood Brain Barrier
BCMA	B-cell Maturation Antigen (TNFRSF17 gene)
BME	Basal Medium Eagle
BSA	Bovine serum albumin
CAR-T	Chimeric Antigen Receptor T-cells
CAs	Contrast agents
CLL	Chronic Lymphocytic Leukemia
CNS	Central Nervous System
CO_2	Carbon dioxide
CRS	Cytokine Release Syndrome
CS	Chitosan
CSPG4	Chondroitin Sulfate Proteoglycan 4 (NG2)
DFO	Desferrioxamine (deferoxamine)
DLS	Dynamic Light Scattering
DLVO	Derjaguin–Landau–Verwey–Overbeek
DMSO	Dimethyl sulfoxide
D_2O	Deuterium oxide
DOTA	1,4,7,10-tetraazacyclododecane-1,4,7,10-tetraacetic acid
EDTA	Ethylenediaminetetraacetic acid
EGFR	Epidermal Growth Factor Receptor
EGFRvIII	Epidermal Growth Factor Receptor variant III
EphA3	EPH Receptor A3

EtOAc	Ethyl acetate
FBS	Fetal bovine serum
FDA	U.S. Food and Drug Administration
FFT	Fast Fourier Transform
FID	Free Induction Decay
FRET	Fluorescence resonance energy transfer
FTLA	Finite Track Length Adjustment
GBM	Glioblastoma Multiforme
GSC	Glioma Stem Cell
HER2	Human Epidermal Growth Factor Receptor 2
HSV1-tk	Herpes Simplex Virus Type 1 Thymidine Kinase
ICANS	Immune Effector Cell-Associated Neurotoxicity Syndrome
IDH	Isocitrate Dehydrogenase
IFFT	Inverse Fast Fourier Transform
IL-13Rα2	Interleukin-13 Receptor Subunit Alpha-2
ITAM	Immunoreceptor Tyrosine-based Activation Motif
MEM	Minimum Essential Medium
MHC	Major Histocompatibility Complex
MRI	Magnetic Resonance Imaging
MSD	Mean Squared Displacement
NaC	Sodium cholate
NaF	Sodium fluoride
NEAA	Non-essential amino acids
NHL	Non-Hodgkin Lymphoma
NIS	Sodium–Iodide Symporter
NMR	Nuclear Magnetic Resonance
NOTA	1,4,7-triazacyclononane-1,4,7-triacetic acid
NP	Nanoparticle
NTA	Nanoparticle Tracking Analysis
o/w	Oil-in-water
PBMCs	Peripheral blood mononuclear cells
PC	Protein corona
PDL	Poly-D-lysine
PEG	Poly(ethylene glycol)

PERFECTA	suPERFluorinatEd ContrasT Agent
PET	Positron Emission Tomography
PFA	Paraformaldehyde
PFC	Perfluorocarbon
PFCE	Perfluoro-15-crown-5-ether
PFOB	Perfluorooctyl bromide
PFPE	Perfluoropolyether
PLGA	Poly(lactic-co-glycolic acid)
P/S	Penicillin–Streptomycin
PVA	Poly(vinyl alcohol)
REP	Rapid Expansion Protocol
RF	Radiofrequency
RH	Relative humidity
SNR	Signal-to-noise ratio
SPECT	Single-Photon Emission Computed Tomography
SPIO	Superparamagnetic Iron Oxide Nanoparticles
TCM	T cell medium
TE	Echo time
TERT	Telomerase Reverse Transcriptase
TFA	Trifluoroacetic acid (CF_3COOH; ^{19}F-NMR/^{19}F-MRI reference standard)
MSCs	Mesenchymal Stem Cells
TNF-α	Tumor Necrosis Factor-alpha
TTFields	Tumor Treating Fields
UV-light	Ultraviolet light
WHO	World Health Organization

Chapter 1

Introduction

1.1 Nanomedicine and Theranostics

Nanomedicine is defined as the science and technology for diagnosing, treating, and preventing diseases and traumatic injuries, relieving pain, and preserving and improving human health through molecular tools and molecular knowledge of the human body [1]. In this framework, five major disciplines were identified: analytical tools, nanoimaging, nanomaterials and nanodevices, novel therapeutics and drug-delivery systems, and clinical, regulatory, and toxicological issues [1].

This definition highlights the close relationship between nanomedicine and nanotechnology, generally used to design and apply materials at the atomic and molecular scale, within a dimensional range below 1 μm. Materials with characteristic dimensions below 1 μm can include natural nanostructures, such as protein aggregates, and synthetic systems, such as engineered nanoparticles used in drug delivery [2]. Representative length scales are illustrated in Figure 1.1.

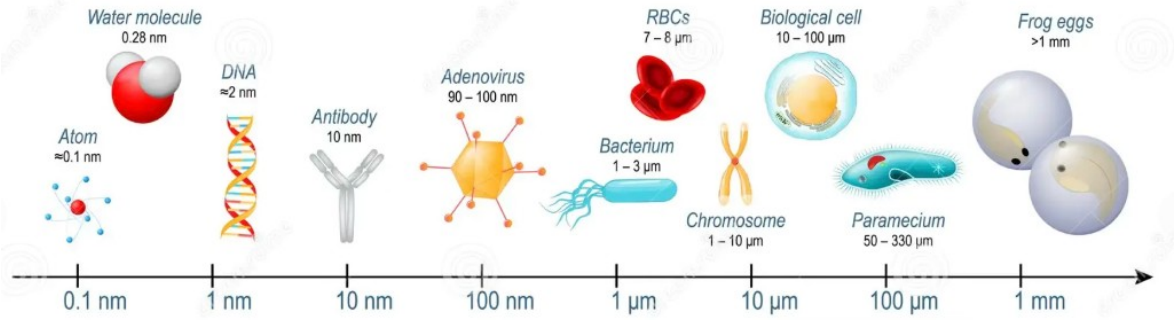

Figure 1.1: Dimensional scale of representative biological and chemical structures, from atomic dimensions (about 0.1 nm) through macromolecules, viruses, bacteria, blood cells and larger cells up to objects in the range of 1 mm [3]. Illustration reproduced under license from Alamy contributor: Tetiana Zhabska; image ID 2DHY2XH;

In biomedicine, nanostructures have become key tools for both therapy and diagnosis. For instance, they can enable controlled delivery of chemotherapeutic agents with

more selective action toward tumor cells [2]. In diagnostics, nanostructures can encapsulate or carry contrast agents compatible with multiple imaging modalities, including Positron Emission Tomography (PET), Computed Tomography (CT)-scan, X-ray and magnetic resonance imaging (MRI) [4].

The use of nanostructures is not limited to diagnostic or therapeutic functions separately. These two approaches can be integrated into single multifunctional platforms able to both identify and treat disease. This field is known as "theranostics", from the fusion of “therapy” and “diagnostics,” and represents a major step toward personalized medicine by combining molecular diagnosis with targeted intervention [2, 4]. Among human diseases, cancer has emerged as one of the principal fields of application for nanomedicine, improving the targeted delivery of chemotherapeutics or enabling multimodal tumor imaging, and supporting integrated theranostic strategies that increasingly underpin precision oncology.

1.2 Glioblastoma and Current Therapeutic Challenges

Glioblastoma (GBM) is the most frequent and most aggressive primary malignant tumor of the adult central nervous system. Under the 2021 World Health Organization (WHO) Classification of Tumors of the Central Nervous System (CNS), 5th Edition (WHO CNS5), the designation “glioblastoma” is specifically reserved for diffuse astrocytic tumors that are IDH (Isocitrate Dehydrogenase) wildtype (without *IDH1*/*IDH2* mutation) and that show either high grade histologic features (microvascular proliferation and/or necrosis) and molecular hallmarks, such as *TERT* (Telomerase Reverse Transcriptase) promoter mutation or *EGFR* (Epidermal Growth Factor Receptor) amplification, and combined chromosome 7 gain with chromosome 10 loss [5, 6]. In simple terms, IDH status is now a key diagnostic separator: IDH wildtype tumors correspond to canonical GBM and usually show a more aggressive clinical behavior, whereas IDH mutant tumors represent a biologically distinct disease pathway and are currently classified as astrocytoma, even when they reach grade 4. This definition at the molecular level has improved diagnostic consistency across centers and has clarified prognostic stratification, because IDH mutant gliomas generally show a more favorable clinical course than IDH wildtype GBM.

From an epidemiological perspective, GBM shows a relatively stable but clinically relevant burden in industrialized countries, with incidence rates commonly reported around 3–5 cases per 100,000 person/years, a peak in older adults, and a modest male predominance [7, 8]. Although it remains a comparatively rare cancer in population terms, it contributes to neurological disability related to cancer and the mortality is disproportionately high, because of rapid progression and limited long-term survival. Even with modern multimodal treatment, median overall survival for newly diagnosed

patients generally remains in the 14–20 month range in trial populations, and outcomes are often less favorable [9, 10].

The etiology of GBM is multifactorial and only partially understood. Ionizing radiation is the only well established environmental risk factor consistently associated with gliomagenesis in humans [11]. Most cases, however, occur sporadically, without a clearly identifiable external exposure. A minority is associated with hereditary cancer predisposition syndromes, such as Li–Fraumeni syndrome (*TP53*), neurofibromatosis type 1 (*NF1*), Turcot syndrome, and constitutional mismatch repair deficiency, supporting the role of genomic instability and DNA repair defects in glioma susceptibility [11, 6]. At the tumor level, GBM is characterized by marked genomic and epigenomic heterogeneity, dynamic evolution, and high cellular plasticity, all of which contribute to therapeutic escape.

The glioblastoma microenvironment is a central determinant of disease behavior and treatment resistance. Rather than a passive scaffold, it is an active tissue composed of neoplastic cells, glioma stem cells, astrocytes, endothelial cells, pericytes, extracellular matrix components, and abundant myeloid populations (resident microglia and infiltrating macrophages), which can represent a major fraction of the tumor mass [12, 13]. This compartment is shaped by regional hypoxia, aberrant angiogenesis, blood–brain barrier (BBB) disruption, and strong immunoregulatory signaling (TGF-β, IL-10, CSF-1), promoting T-cell dysfunction and a broadly immunosuppressive milieu [12, 13]. The crosstalk between tumor cells and the immunosuppressive microenvironment fosters tumor cell infiltration into adjacent tissues. Accordingly, tumor cells acquire stem properties ("stemness"), enabling them to self-renew (i.e., proliferate while retaining an undifferentiated state), undergo differentiation into more mature progeny, evade therapeutic pressure and reconstitute the tumor mass in new locations from a small pool of migrating cells.

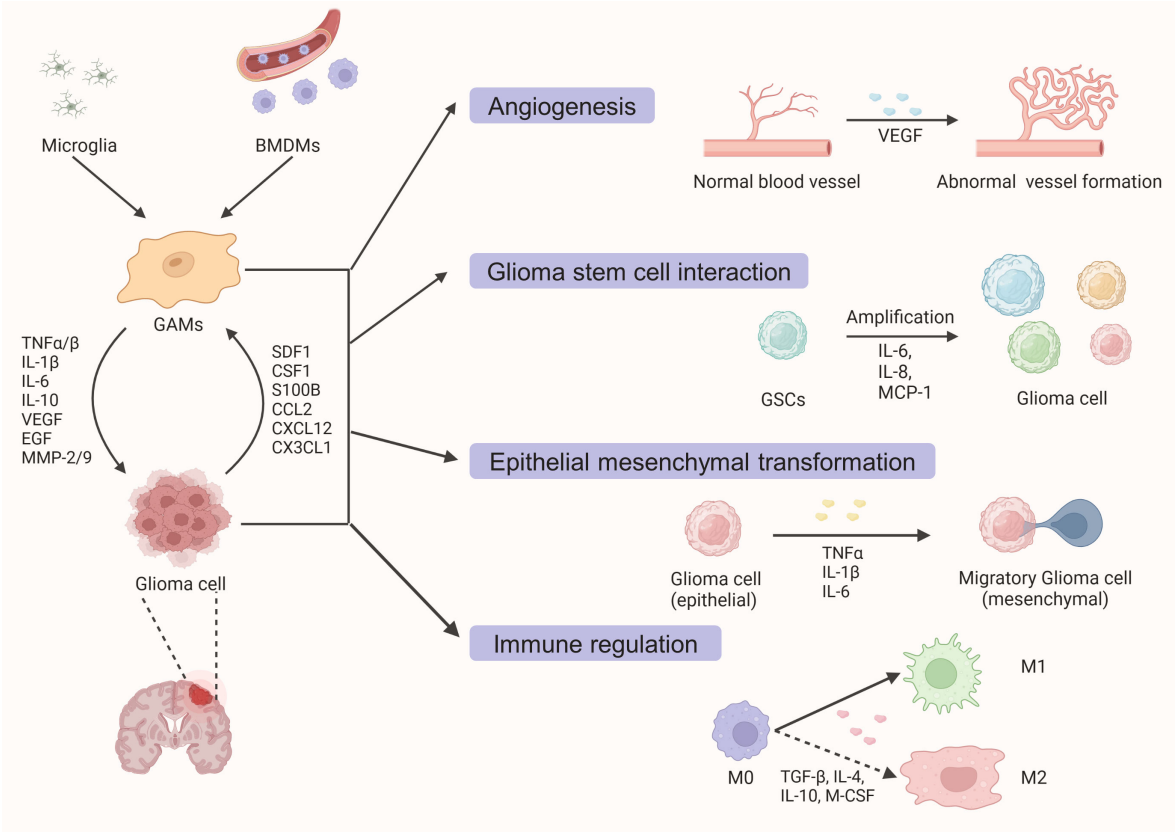

Figure 1.2: Representative schematic of microglia and macrophage interactions (GAMs) in glioblastoma, within the tumor microenvironment. Under the action of various cytokines and chemokines secreted by tumor cells, resident microglia, and peripheral blood-derived macrophages are recruited into the tumor parenchyma. Activated GAMs interact with tumor cells to promote glioma growth and invasion through various mechanisms such as angiogenesis promotion, GSCs proliferation, epithelial-mesenchymal transformation, and tumorigenic immune regulation. Reproduced from Lin et al. (2023). [13].

Current clinical management is based on maximal safe surgical resection followed by radiotherapy with concomitant and adjuvant temozolomide (the Stupp regimen), with additional benefit, in selected patients, from tumor treating fields (TTFields) during maintenance therapy [9, 10, 14]. They are an external device (electrodes placed on the scalp) that generates low intensity electric fields to interfere with tumor cell division. Nonetheless, recurrence is nearly universal, and options at progression (re-operation, re-irradiation, bevacizumab in selected settings, clinical trials) provide modest and often temporary disease control.

Within this context, immunotherapy for GBM has gained major translational interest, especially adoptive cellular strategies. A relevant antigenic target is B7-H3 (CD276), an immune checkpoint family member that is frequently overexpressed in glioblastoma cells and associated vasculature, while being comparatively limited in normal brain tissue, making it an attractive target for selective immune redirection [15, 16]. Functionally, B7-H3 contributes to immune evasion, tumor aggressiveness and adverse biological behavior [17]. Preclinical studies have shown that anti-B7-H3 CAR-T cells can mediate robust cytotoxicity against GBM cell lines and patient-derived neu-

rospheres, supporting clinical development of these approaches in solid tumors, such as GBM [15, 16]. Therefore, the convergence of a profoundly suppressive microenvironment and a highly expressed surface antigen such as B7-H3 provides a strong rationale for combining antigen-specific cell therapy with technologies that allow *in vivo* tracking of therapeutic cell distribution, persistence, and tumor infiltration.

1.3 Adoptive Cell Therapy

The Adoptive cell therapy (ACT) focuses on leveraging the patient's own natural immune defenses, with the aim of modifying the immune balance established within the tumor microenvironment.

The ACT is based on the reinfusion into patients of immune effector cells with anti-tumor activity, which can be naturally occurring (for example tumor infiltrating lymphocytes, TILs, expanded *ex vivo* and then reinfused) or genetically engineered *ex vivo* (for example CAR-T cells) [18]. The biological rationale is to overcome quantitative and qualitative limitations of endogenous anti-tumor immunity: ACT enables the selection, expansion, functional programming and genetic engineering of lymphocytes outside the immunosuppressive tumor environment and then returns to the host a large, activated, and potentially persistent "living drug" [18, 19]. The "living drug" definition reflects a key ACT feature: transferred cells can expand *in vivo* and maintain anti-tumor activity, so that the effective dose of the "biological living drug" can evolve after infusion.

From a translational perspective, ACT now includes multiple platforms with different recognition logics and manufacturing differences:

- **T-Cells Receptor (TCR) Engineered**, in which T lymphocytes are genetically modified through *in vitro* gene transfer to express a synthetic T-cell receptor able to recognize MHC complexes peptide (MHC-I-dependent) on tumor cells; a key limitation is that many tumors reduce surface MHC-I presentation, which can markedly impair TCR-mediated recognition and cytotoxicity [20];

- **Chimeric Antigen Receptor (CAR) T-cells**, in which T lymphocytes are genetically engineered to express a synthetic Chimeric Antigen Receptor (CAR), through viral transduction or non-viral transfection approaches, enabling direct surface antigen recognition, in an MHC-I-independent manner;

- **Tumor Infiltrating Lymphocytes (TILs)**, based on *ex vivo* expansion of autologous T cells infiltrating the tumor area, isolated from resected tumor tissue.

The strongest clinical proof-of-concept (POC) to date remains CAR-T therapy in hematological malignancies, where several therapeutical products, targeting CD19

or BCMA, have produced high response rates and durable remissions in relapsed or refractory disease [21]. However, extension to solid tumors is still limited by major barriers: heterogeneous target expression, poor trafficking through abnormal tumor vasculature and BBB, physical stromal barriers, chronic antigen exposure for T-cells, which causes their dysfunction and exhaustion, and a profoundly immunosuppressive microenvironment [19, 22].

These limitations are particularly relevant in glioblastoma, where tumor heterogeneity and spatially variability of antigen expression coexist with alterations of blood–brain barrier (BBB), myeloid immunosuppression and rapid local recurrence. In this context, ACT remains highly attractive but must be coupled with advanced engineering strategies and robust *in vivo* monitoring tools to understand where therapeutic cells traffic, how long they persist, and whether they effectively reach and kill tumor tissue over time.

1.3.1 Engineering Chimeric Antigen Receptor T-Cells (CAR-T)

CAR-T cells are autologous (or, in development, allogeneic) T lymphocytes genetically modified to express a synthetic receptor, that combines antibody-antigen recognition with T-cell activation signaling [21].

A chimera, in molecular biology, is an engineered protein that combines functional domains derived from different biological molecules. A CAR is considered chimeric because it merges into a single membrane protein two functions that naturally belong to two distinct cell types:

- **Antibody recognition (Extracellular domain).** Normally, T lymphocytes recognize antigens only when they are presented as peptides on the MHC-I complex (they are "MHC-restricted"). In contrast, B lymphocytes recognize antigens directly on the cell surface without requiring MHC presentation. CARs are designed to reproduce this B-cell recognition capability in an MHC-I-independent manner. The extracellular domain of the CAR consists of an scFv (single-chain variable fragment), composed of the variable regions V_H and V_L of a monoclonal antibody connected by a flexible linker. This scFv binds directly to a tumor-associated surface antigen (e.g., CD19, BCMA, B7-H3) in an MHC-I-independent manner.

- **T-cell activation signaling (Intracellular domain).** Once the antigen is recognized, the cell must become activated and kill the target. This requires an intracellular signaling cascade characteristic of T lymphocytes, which is normally triggered by the TCR. In CARs, this signaling machinery is directly incorporated into the receptor itself through cytoplasmic signaling domains:

- **CD3ζ (zeta):** the signaling chain of the TCR complex, containing ITAM motifs (Immunoreceptor Tyrosine-based Activation Motifs), which, once phosphorylated, initiate the activation signaling cascade (signal 1).
- **Co-stimulatory domains (signal 2),** typically CD28 or 4-1BB (CD137), and sometimes OX40. These domains are essential to achieve full T-cell proliferation, persistence, and effector function, as the absence of co-stimulation would lead to anergy. [23, 24].

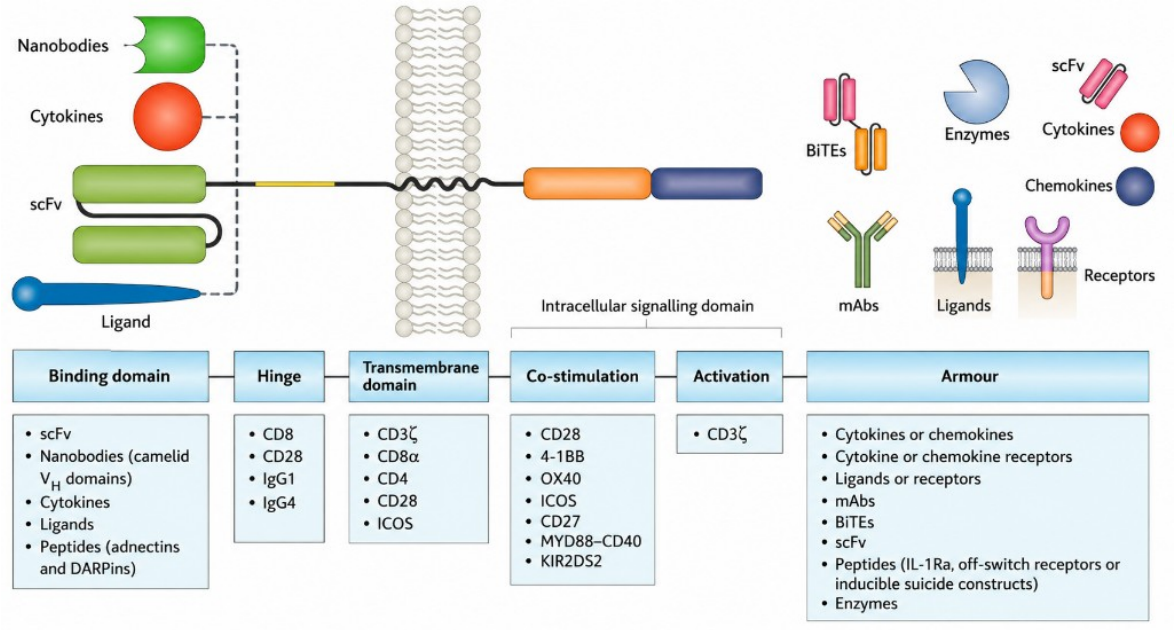

Figure 1.3: Blueprint of CAR design, showing (i) an extracellular single-chain variable fragment (scFv) specific for tumor surface antigen recognition; (ii) a hinge/spacer domain influencing receptor flexibility and immunological synapse geometry; (iii) a transmembrane domain; and (iv) intracellular signaling modules, including CD3ζ as a primary activation domain, plus one or more co-stimulatory domains (most commonly CD28 or 4-1BB). Reproduced from Rafiq et al. [19].

CAR architectures have evolved through different generations. First generation CARs contained only the CD3ζ signaling domain. Second generation CARs added a single co-stimulatory domain, such as CD28 or 4-1BB, and are currently the most widely used in approved therapies. Third generation CARs combine two co-stimulatory domains, while fourth and fifth generation CARs include additional features, such as cytokine secretion systems or logic gates, that function like AND/OR/NOT gates used in electronic circuits to simultaneously switch on/off different signal, with the aim of improving their activity within the immunosuppressive tumor microenvironment [19, 22].

From a processing point of view, CAR-T cell production is a strictly regulated and multistep manufacturing chain in which each operation can influence final product potency, safety, and *in vivo* persistence. The workflow is conceptually represented in Figure 1.4 (adapted from Hartmann et al., 2017 [23]).

1. **Leukapheresis.** The process begins with the collection of the patient's peripheral blood mononuclear cells (PBMCs) by leukapheresis, an extracorporeal procedure that separates the mononuclear fraction (mostly T and B lymphocytes, monocytes, and NK cells) from erythrocytes and granulocytes by centrifugation. The composition of this starting material are highly variable between patients and strongly influence the T-cell expansion and longer *in vivo* persistence [23, 19].

2. **T-cell activation.** Once isolated, T-cells need a signal to enter the cell cycle and become receptive to gene transfer. This is achieved *ex vivo* by stimulating CD3 together with CD28, typically using paramagnetic beads coated with anti-CD3/anti-CD28 antibodies (for example Dynabeads) or feeder cells [23, 19].

3. **Gene transfer.** The activated T cells are then genetically modified to stably express the CAR transgene. The most clinically established platforms rely on integrating viral vectors: γ-retroviral vectors and lentiviral vectors (HIV-1 derived and inactivated), which can transduce slowly proliferating cells; all currently approved CAR-T products use one of these two systems [21, 23]. Non-viral alternatives are under investigation to reduce manufacturing cost and complexity. Integrating platforms include transposon systems based on DNA plasmids and a transposase to integrate the CAR cassette, while transient strategies employ *in vitro* transcribed mRNA delivered by electroporation or, more recently, by ionizable lipid nanoparticles (LNPs), which encapsulate and protect the mRNA cargo, improving cellular uptake with reduced cytotoxicity. More recently, CRISPR/Cas9-mediated targeted integration has been explored to obtain uniform CAR expression between cells, because Cas9 (an endonuclease, a protein that cuts double-stranded DNA) targets a "safe" and biologically relevant locus (e.g., the TCR gene) and, through HDR (Homology-Directed Repair), inserts the CAR cassette there instead of allowing the vector to integrate randomly.[19, 25].

4. ***Ex vivo* expansion.** After transduction, cells are cultured for typically 7–14 days to reach a clinically relevant dose, generally on the order of 10^6–10^8 CAR-T cells per kilogram of body weight. Culture conditions are tuned to limit terminal differentiation: short expansion times and cytokine cocktails enriched in IL-7/IL-15 are strategies designed to preserve stemness, which correlate clinically with deeper and more durable responses [23, 26, 19].

5. **Quality control.** Before infusion, the final product must pass a panel of quality control assays covering identity, purity, viability, potency, vector copy number or transgene expression and microbiological safety [23, 21].

6. **Infusion.** The CAR-T product is then administered intravenously (or, in selected solid tumor protocols, by intracavitary, intratumoral, or intraventricular delivery),

followed by a structured monitoring window for the early management of emergent toxicities [21, 22].

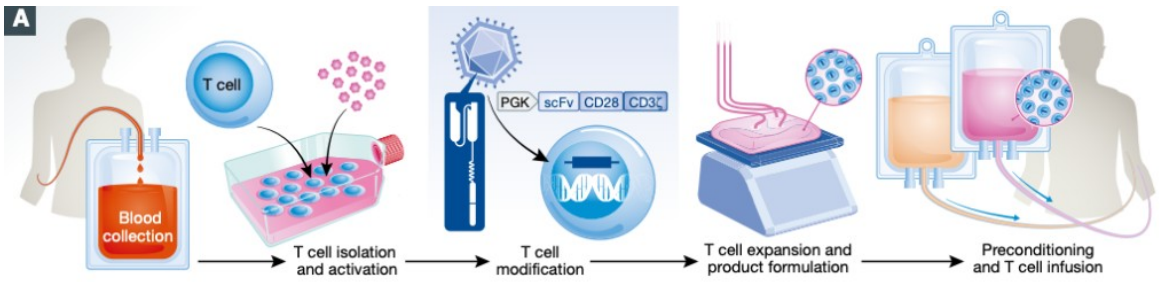

Figure 1.4: Schematic overview of the autologous CAR-T manufacturing and clinical use chain ("vein-to-vein"): PBMC collection by leukapheresis; *ex vivo* T-cell isolation and activation; genetic modification, typically by viral-vector transduction of a CAR cassette; expansion and formulation into the drug product; lymphodepleting preconditioning and reinfusion of engineered T cells. Figure adapted from Hartmann et al. [23].

Major limitations of CAR-T cell therapy include:

- **Manufacturing complications,** because CAR-T production is patient-specific, expensive, and requires several weeks, while differences in lymphocyte quality between patients can strongly affect the final therapeutic efficacy [23, 25].
- **Toxicity,** because CAR-T therapy can induce severe side effects such as cytokine release syndrome (CRS), Immune Effector Cell-Associated Neurotoxicity Syndrome (ICANS), and damage to healthy tissues expressing low levels of the target antigen [21, 22].
- **Limited efficacy in solid tumors.** In tumors such as glioblastoma, CAR-T cells face major barriers including poor trafficking to the tumor site, restricted access through the blood–brain barrier (BBB) and a strongly immunosuppressive tumor microenvironment that promotes T-cell exhaustion [19, 22, 12].
- **Antigen heterogeneity and tumor escape.** Solid tumors are highly heterogeneous, with antigen-negative cells, limiting the effectiveness of single-target CAR-T strategies [19, 22].

1.3.2 Current status of CAR-T therapy

Chimeric antigen receptor (CAR) T-cell therapy is now a validated therapeutic class in oncohematology, for several B-cell malignancies and multiple myeloma. The clinical story begins with autologous T cells engineered to recognize CD19, a lineage antigen broadly expressed on malignant and normal B cells. Early phase studies established CAR-T cells as a pharmacologically "living" drug class in relapsed or refractory acute

Table 1.1: Representative CAR-T programs: publication years, tumor context, antigen target, study stage, and references.

Year	Tumor type	Target	Study stage	References
2011–2015	B-cell leukemia / lymphoma (ALL, NHL, CLL)	CD19	Early clinical trials (phase 1–2)	[27, 28, 29]
2017	Diffuse large B-cell lymphoma	CD19	Phase 2 trial; approved therapy (multiple regions)	[31]
2021	Multiple myeloma	BCMA	Approved therapy (pivotal trials)	[21, 22]
2024	Solid tumors (murine models)	Multiple + IL-10	Preclinical (in vivo)	[32]
2024	Glioblastoma	EphA3	Preclinical (in vivo)	[33]
2025	Glioblastoma	EGFR + IL-13Rα2	Clinical trial (phase 1)	[34]
2024	Gastrointestinal adenocarcinomas	Claudin 18.2	Clinical trial (phase 1)	[35]

lymphoblastic leukemia (ALL), chronic lymphocytic leukemia, and aggressive B-cell lymphomas [27, 28, 29, 30].

Within neuro-oncology, glioblastoma has become a key tumor for testing these innovative therapy. The field has moved from first generation feasibility studies (e.g., EGFRvIII, IL13Rα2, HER2) toward more adaptive designs and alternative targets such as B7-H3, chosen for their high prevalence in the tumor tissue, the strong antigen expression across a large proportion of tumor cells and the ability of the therapy to selectively target malignant cells while sparing healthy CNS cells such as neurons and glia, which must not be damaged. [15, 16, 17]. The pillar of this strategy is **B7-H3** (CD276), a member of the B7 immune checkpoint family, that is frequently overexpressed on glioblastoma cells, perivascular tumor niches and tumor-associated vasculature, while remaining comparatively low in normal brain parenchyma [15, 17]. Beyond its value as a CAR target, B7-H3 contributes to immune evasion and adverse tumor behavior within the immunosuppressive glioblastoma microenvironment [17]. Preclinical works demonstrated that B7-H3 is overexpressed across molecular GBM subtypes, with high protein expression in approximately 76% of patient specimens and ubiquitous expression on patient-derived neurospheres (tumoral stem cells model) [16]. For this purpose, anti-B7-H3 CAR-T cells mediated robust cytotoxicity against GBM cell lines and neurospheres *in vitro* [16, 15] and are currently being explored as a potential immunotherapeutic approach for glioblastoma treatment. Nevertheless, single-antigen CAR-T cells can lose recognition of the tumor, when antigen expression drops or when only a subset of cells strongly expresses the target [19, 16]. One useful design pattern is therefore a *dual* CAR-T product, that recognizes two surface molecules on tumor cells. An example of a specific dual-target class is **B7-H3 paired with CSPG4** (also called NG2). Sometimes this pairing is written as "B7 + CS" or "B7zCS, " where "CS" refers to the chondroitin sulfate proteoglycan CSPG4. [36]. **CSPG4**, is a membrane proteoglycan associated with glioma invasion, plasticity, angiogenesis, and stromal interactions

[36, 37].

1.3.3 Need for non invasive in vivo monitoring of therapeutic cells: Rationale of the thesis

Despite major progress in cellular engineering, the development of ACT in solid tumors remains partly "blind" after infusion: common clinical endpoints used to evaluate therapy, such as patient survival, tumor response, adverse toxicity and neurological clinical status, do not directly reveal where transferred cells migrate and how they localize, whether they expand *in vivo* at the tumor site, how long they persist over time in the target compartment or to what extent they infiltrate active tumor regions. This lack of spatiotemporal information limits interpretation of therapeutic failure and refinement of therapy in terms of dose optimization, route of administration and treatment scheduling.

Clinical development of immunotherapy against glioblastoma is oriented toward locoregional routes of administration, specifically intracatheter delivery after tumor surgical resection. This administration makes it possible to reduce the occurrence of GBM recurrences, since the presence of CAR-T cells would target residual tumor cells that escaped surgical removal, especially given the particularly highly infiltrative behavior of GBM. In this way, exposure at the central nervous system level is improved and systemic toxicity is potentially reduced. Although this thesis focuses on CAR-T cells for glioblastoma, the same need for non-invasive longitudinal monitoring applies broadly to other cell-based therapies, including stem cells and mesenchymal stem cells (MSCs), whose therapeutic efficacy also depends on their biodistribution, persistence, survival, and interaction with the target tissue after administration.

These needs make the translational gap even more evident: without quantitative, *in vivo*, non-invasive and longitudinal cell tracking, it is difficult to distinguish true biological resistance to treatment from inadequate cell distribution and persistence. A treatment may fail, for example, because CAR-T cells lose functionality but also because they do not reach sufficient numbers in relevant tumor niches. Conversely, local inflammatory changes due to exposure to ACT therapy may be confused with tumor progression on conventional magnetic resonance imaging, complicating interpretation of therapeutic response.

In this scenario, molecular imaging represent a non-invasive approach that allows us to follow the fate of a target cell in vivo, in real time and, in some cases, it might also be used to predict therapy response. [38]. In fact, ^{19}F-MRI offers a negligible endogenous background, with a linear relationship between signal and fluorine content, that enables potential quantitative estimation of labeled cell *in vivo*, provided that the signal derives from truly internalized nanoparticles and not from free or superficially

associated nanoparticles.

Integrating this approach with ACT could help answer clinically relevant questions:

- Do infused CAR-T cells persist and function correctly in the tumor compartment?
- How does distribution evolve over time after locoregional administration?
- What is poor anti-tumor efficacy associated with?

Therefore, the rationale of this thesis is to optimize the labeling process for ACT products and to contribute to a broader paradigm shift: from evaluation based exclusively on clinical endpoints to monitoring of adoptive cellular therapies in glioblastoma guided by a genuine understanding of biological mechanisms.

1.4 Imaging Strategies for Cell Tracking

To address the need for non-invasive monitoring of adoptive cell therapies, several molecular imaging modalities have been developed in both preclinical and clinical settings. Strategies can be broadly divided into *direct* labeling and *indirect* labeling. Direct labeling involves the *ex vivo* loading of cells with an imaging agent that is retained within or associated with the cells, followed by administration of the labeled cells to the patient. However, the labeling agent is progressively diluted as cells divide and proliferate, resulting in a loss of sensitivity. [38, 39]. Indirect labeling, on the other hand, refers to the *in vivo* targeting of specific antigens expressed by particular immune subtypes or to the use of reporter genes. The limitations of this approach arise from the expression of the target antigen by other cellular subpopulations as well as from the physiological uptake of the tracer by major organs. [38, 39]. The principles of indirect and direct cell labeling used for cell tracking are summarized in Figure 1.5.

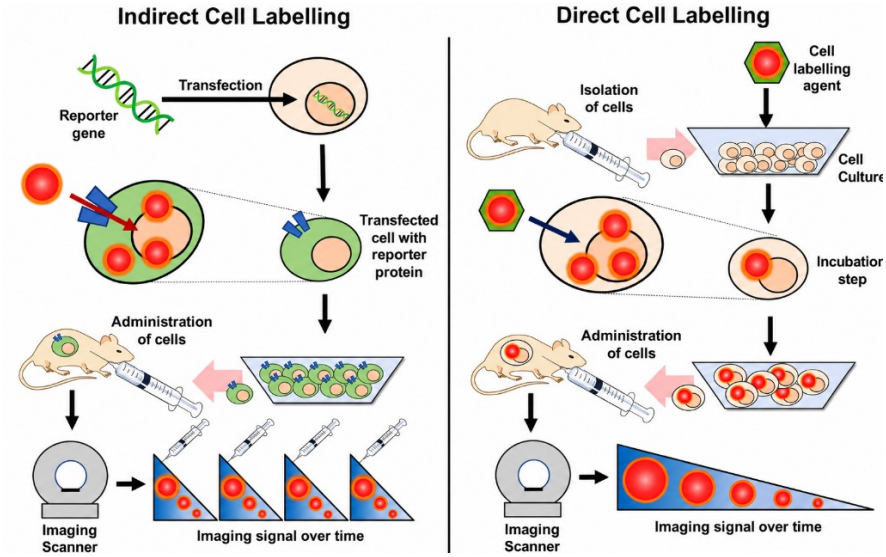

Figure 1.5: Principles of indirect and direct cell labeling used for cell tracking. (A) Indirect cell labeling. Cells are genetically modified with a reporter gene, enabling them to express a reporter protein, which allows binding or uptake of the imaging label *in vivo*. The cells can then be administered into the subject and imaged over time by repeated injections of imaging label that binds specifically to cells expressing the reporter gene. In principle, the gene expression persists over the lifespan of the cell and can be passed on to daughter cells. (B) Direct cell labeling. Cells are isolated from the subject, donor or culture and labeled *in vitro*. The labeled cells are then administered into the subject and can be imaged repeatedly for as long as the half-life of the imaging label allows (from hours to days). Reproduced from Gawne et al. [39].

1.4.1 Radiolabeling platforms for in vivo cell tracking with PET and SPECT

Nuclear medicine techniques based on positron emission tomography (PET) and single-photon emission computed tomography (SPECT) are among the most sensitive and clinically translatable options for whole body cell tracking [39, 40]. Nuclear medicine imaging exploits the physical decay of radionuclides incorporated into radiotracers administered to the patient. For cell-tracking applications, the radionuclide is either carried by the therapeutic cells themselves (direct labeling) or by a separate probe that reports on cell location (indirect labeling) [39, 38]. In both cases, emitted radiation is detected externally and reconstructed into three-dimensional (3D) images that reflect tracer distribution in the body.

SPECT relies on radionuclides that decay by emission of gamma (γ) photons of characteristic energy. Each isotope exhibits one or more characteristic energy peaks ("chemical fingerprint") that the detector can discriminate, enabling distinction between different tracers (multiplexing). [41, 40].

For cell tracking, SPECT offers very high detection sensitivity (concentrations of radiotracer as low as picomolar or nanomolar can be visualized) and, with appropriate calibration, can quantify radionuclide activity in a given region to assess radiotracer biodistribution and, indirectly, cellular distribution. Furthermore, because

infused cells migrate over extended time scales (hours to days), SPECT is compatible with radionuclides of medium to long physical half-life, matched to the biological time scale of cell trafficking: half-lives long enough that the signal does not decay too rapidly, yet short enough to limit prolonged patient exposure [39, 42]. Clinically relevant SPECT radionuclides include technetium-99m (^{99m}Tc; $t_{1/2} \approx 6.0\,\mathrm{h}$), indium-111 (^{111}In; $t_{1/2} \approx 2.8\,\mathrm{d}$), and radioiodine isotopes such as ^{123}I and ^{131}I. Indium-111 is particularly important for direct cell labeling because its half-life supports imaging over several days after infusion of labeled cells. [42, 39].

PET uses radionuclides that decay by β^+ (positron) emission. The emitted positron travels a short distance in tissue (positron range, typically sub-millimeter to a few millimeters depending on nuclide) before annihilating with an electron. Each annihilation event produces two collinear γ photons emitted in opposite directions [41, 40]. Only events in which two opposing detectors register photons within a narrow timing window are retained as true coincidences. For this reason, PET has intrinsically higher sensitivity than conventional SPECT and generally achieves somewhat better spatial resolution in clinical systems (approximately 4–6 mm for whole body PET versus 8–15 mm for clinical SPECT) [41, 39].

The most widely used clinical PET tracer is [^{18}F]fluoro-2-deoxy-D-glucose ([^{18}F]FDG), reflecting enhanced glycolysis in many tumors and inflammatory cells; ^{18}F has a half-life of approximately 110 minutes [40]. For longitudinal cell tracking over hours to days, longer lived PET radionuclides are preferred, including ^{64}Cu ($t_{1/2} \approx 12.7\,\mathrm{h}$) and ^{89}Zr ($t_{1/2} \approx 3.3\,\mathrm{d}$), which are typically introduced via chelating ligands such as DOTA, NOTA, or desferrioxamine (DFO), that stably bind the metal to enable a predictable and diagnostically useful biodistribution. [39, 43].

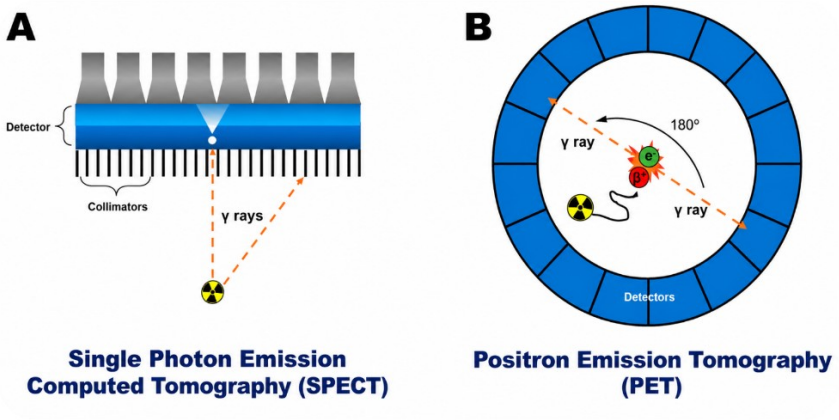

Figure 1.6: Schematic representation of (A) single photon emission computed tomography (SPECT) and (B) positron emission tomography (PET). (A) SPECT: a γ-emitting radionuclide decays within the body and emits γ photons isotropically; a collimator transmits only photons travelling nearly perpendicular to the detector, so that each detector element is sensitive to radiation from a narrow spatial cone. Rotating the γ camera around the subject yields multiple two-dimensional projections that are reconstructed into a three-dimensional tomogram. (B) PET: a β^+-emitting radionuclide produces positrons that annihilate with electrons, generating two collinear 511 keV γ photons emitted in opposite directions; only coincident detection by opposing detectors within a narrow timing window is retained, defining a line of response without physical collimation. Adapted from Man et al. [44]. Figure reproduced via Gawne et al. [39].

PET/SPECT versus MRI in cell tracking. Both modalities provide whole body, tomographic readouts with excellent sensitivity compared with MRI or optical methods, but they differ in instrumentation, radionuclide tracers and operational constraints [39, 38]. PET benefits from higher sensitivity and more accurate attenuation correction, whereas SPECT is often more widely available, less expensive and allows multiplexed imaging of multiple γ-emitting isotopes with distinct energies. A shared limitation is the use of ionizing radiation, which imposes dosimetry constraints on patients and staff and requires GMP compliant radiochemistry. Spatial resolution remains inferior to MRI and the imaging signal, after direct labeling, can be confounded by radiotracer efflux, phagocytic clearance of dead cells and dilution of label upon cell division [39, 38]. Nevertheless, both modalities have been applied to immune cell tracking in clinical and translational studies. For direct labeling, autologous leukocytes loaded *ex vivo* with ^{111}In-oxine or ^{99m}Tc-hexamethylpropyleneamine oxime (^{99m}Tc-HMPAO) and reinfused remain the reference SPECT paradigm for infection and inflammation imaging [42, 39]. Direct PET cell tracking has been demonstrated after metabolic or chelator-based *ex vivo* labeling of cytotoxic T lymphocytes and CAR-T cells, illustrating the potential of nuclear imaging for monitoring adoptive immunotherapy in the central nervous system [38]. Together, these examples establish nuclear medicine as a translational reference for whole body cell tracking [38].

Magnetic resonance imaging (MRI) represents a complementary approach to nuclear medicine for cell tracking in the central nervous system [40, 39]. Unlike PET and SPECT, MRI does not rely on ionizing radiation and offers superior soft tissue con-

trast and spatial resolution, enabling more precise anatomical localization of labeled cells within the brain and peritumoral parenchyma, an advantage that is particularly relevant in glioblastoma, where therapeutic cells must be distinguished from complex post treatment changes on conventional scans [14, 39]. Cell tracking by MRI is typically implemented through direct labeling, in which cells are loaded *ex vivo* with contrast agents before reinfusion [38, 45]. Two main classes of MRI compatible labels have been explored: superparamagnetic iron oxide nanoparticles (SPIO), which shorten T_2/T_2^* relaxation and generate negative (hypointense) contrast [45, 4], and fluorine-based reporters detected by proton decoupled ^{19}F-MRI, which exploits the near absence of endogenous fluorine in tissues to provide a background free and quantitative readout [46, 47]. The following subsections review these strategies and their relevance to adoptive cell therapy monitoring, with particular emphasis on ^{19}F-MRI cell labeling.

1.4.2 Magnetic Resonance Imaging (MRI) and Contrast Agents

Magnetic resonance imaging (MRI) is a tomographic modality that exploits the interaction between nuclear spins of atoms and both static and variable magnetic fields in time. [40, 48]. The detected signal arises from radiofrequency (RF) emission by selected nuclei, most commonly the protons of water in tissues in clinical proton ^{1}H-MRI, following controlled excitation and relaxation within a strong main magnetic field [48, 49]. For adoptive cell therapy monitoring, MRI is particularly attractive because it combines a detailed anatomical reference provided by ^{1}H-MRI with direct or indirect cellular labeling exploiting by ^{19}F-MRI [45, 39, 38].

Physical Principle of MRI

Magnetic resonance imaging (MRI) focuses on specific useful nuclei, characterized by a non-zero nuclear spin angular moment I, so that they are NMR active [48, 49]. By definition, the nuclear spin angular moment (I) indicates the amount of "intrinsic rotation" of the nucleus.

Every atomic nucleus possesses, also, a magnetic moment $\boldsymbol{\mu}$, defined as the magnetic behavior of the nucleus [48].

The magnetic moment of an atom is calculated as $\boldsymbol{\mu} = \gamma I$, where γ is the gyromagnetic ratio, which differs for each isotope [48, 49]. In biological tissues, the dominant signal source is the proton (^{1}H, $I = 1/2$, $\gamma/2\pi \approx 42.58\,\mathrm{MHz\,T^{-1}}$), present in abundance in free and bound water, lipids, and macromolecules [48]. Only nuclei with $I \neq 0$ are NMR active; this includes, among others, ^{19}F ($I = 1/2$, $\gamma/2\pi \approx 40.08\,\mathrm{MHz\,T^{-1}}$) [46, 50].

In the absence of an external field, nuclear magnetic moments are randomly oriented and the net magnetization of a voxel is zero [48]. When the sample is placed in a strong,

homogeneous static magnetic field $\mathbf{B}_0$ (typically from 1.5 to 7 T), each nuclear magnetic moment precesses about $\mathbf{B}_0$ at the Larmor frequency

$$\omega_0 = \gamma B_0 \qquad \text{or} \qquad f_0 = \frac{\gamma B_0}{2\pi}, \tag{1.1}$$

with a small excess population that aligns parallel with $\mathbf{B}_0$. Summing all nuclear magnetic moments within a voxel (a small 3D volume of tissue), the small excess no longer cancels, yielding a net magnetization M_0 aligned along $\mathbf{B}_0$, (conventionally the z axis), proportional to spin density and field strength [48, 49]. At the equilibrium, M_0 is directed along B_0 and cannot be detected directly; MRI therefore requires a resonance frequency (RF) excitation to create a detectable transverse component [48].

Indeed, a brief RF pulse applied perpendicular to $\mathbf{B}_0$ at the Larmor frequency f_0 delivers energy resonantly to the nuclear spin and tips M_0 away from the z axis, creating transverse magnetization M_{xy}, that precesses coherently and induces a voltage in the receiver coil [48, 49]. The flip angle α depends on pulse duration, B_1 amplitude, and γ; in spin-echo and gradient-echo sequences, α is typically chosen between 90° and 180° for excitation or refocusing [48]. After the RF pulse is switched off, the magnetization vectors relax back toward equilibrium: the longitudinal component (M_z) recovers toward M_0, while the transverse component (M_{xy}) decays as the spins dephase with one another. This time-domain signal, coming from the decaying transverse magnetization (M_{xy}), is often referred to as the free induction decay (FID) [48]. In most clinical sequences, however, the data used for imaging are acquired at an echo (spin-echo or gradient-echo) at a chosen echo time TE, when the signal is stronger and more stable [48, 40]. During readout, magnetic field gradients (G_x, G_y, G_z) encode spatial information into k-space by making the Larmor frequency and phase position-dependent, so that each sampled signal point corresponds to a location in k-space (not yet to an anatomical image). Inverse Fourier transformation (IFFT) of the complete k-space dataset reconstructs the anatomical image [48, 40, 49].

Once excited, magnetization returns to equilibrium through two independent relaxation mechanisms [48, 49]:

- **Longitudinal (spin–lattice) relaxation (T_1)** restores M_z toward M_0. T_1 measures how quickly longitudinal magnetization recovers alignment with $\mathbf{B}_0$: a short T_1 indicates rapid recovery and a long T_1 indicates slow recovery [48, 49]. On T_1-weighted images, tissues with short T_1 appear bright, whereas fluids with long T_1 remain dark [48, 49]. T_1-weighted scans are widely used for anatomical and structural assessment [40, 48].

- **Transverse (spin–spin) relaxation (T_2)** dephases M_{xy} with time constant T_2 [48, 49]. T_2 characterizes how rapidly transverse magnetization (M_{xy}) dephases as

spins lose phase coherence during return toward equilibrium; T_2 is always less than or equal to T_1 [48, 49]. On T_2-weighted images, fluids with long T_2 appear bright, as in vasogenic edema and many inflammatory processes [48, 49, 40]. The apparent decay constant T_2^* is closely related to T_2 but additionally includes dephasing from static main field inhomogeneities and local magnetic susceptibility variations, with $T_2^* \leq T_2$ [48, 49].

The figure 1.7 shows an overwie of the physical principles.

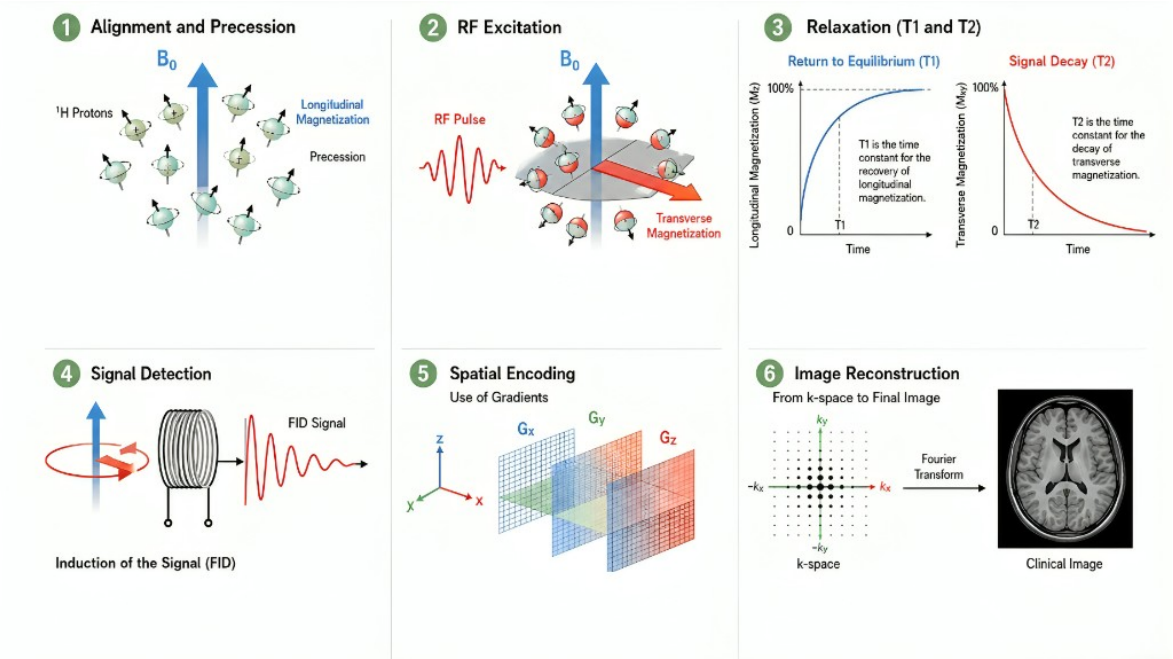

Figure 1.7: Overview of the MRI process: alignment in $\mathbf{B}_0$, RF excitation, T_1/T_2 relaxation, FID detection, gradient encoding, and image reconstruction.

Once the k-space data are reconstructed, image quality is commonly described by the signal-to-noise ratio (SNR) and by tissue contrast. The SNR quantifies how much larger the useful MRI signal is than the random fluctuations (noise) that limit detectability [48, 49]. In a region of interest it is estimated as

$$\mathrm{SNR} = \frac{S}{\sigma_n}, \tag{1.2}$$

where S is the mean signal intensity and σ_n is the standard deviation of the noise, often measured in a signal-free background region [48]. Image contrast, in turn, is defined as the difference in signal intensity between a region of interest and its surroundings [49]. A large contrast between tissues is clinically useful only if both signals are sufficiently above the noise level; otherwise, differences cannot be distinguished reliably. In MRI, contrast is therefore not a single physical parameter: the signal in each voxel depends on intrinsic tissue properties (proton density ρ, T_1, T_2, apparent diffusion coefficient D,

magnetic susceptibility χ) and on extrinsic acquisition choices (α, B_0, coil configuration) [40, 49, 51]. For adoptive cell tracking, limited SNR remains a frequent bottleneck when labeled cells are sparse, even when contrast agents are used to enhance tissue differences [45, 52].

When intrinsic differences in ρ, T_1, or T_2 are insufficient to distinguish tissues, exogenous contrast agents (CAs) are introduced to shorten relaxation times in their microenvironment [49, 51, 53]. Most clinical CAs do not emit signal themselves; they alter the relaxation of surrounding water protons through dipolar and susceptibility interactions at the molecular or particulate scale [49, 40]. The effect is quantified by longitudinal and transverse relaxivities r_1 and r_2 ($\mathrm{mM}^{-1}\,\mathrm{s}^{-1}$), defined through

$$\frac{1}{T_1} = \frac{1}{T_{1,0}} + r_1[\mathrm{CA}], \qquad \frac{1}{T_2} = \frac{1}{T_{2,0}} + r_2[\mathrm{CA}], \tag{1.3}$$

where $T_{1,0}$ and $T_{2,0}$ are relaxation times in the absence of agent and [CA] is the local effective concentration [49, 53].

Gadolinium-based contrast agents (GBCAs). Gadolinium(III) ions, Gd^{3+}, are strongly paramagnetic and, when chelated to macrocyclic or linear poly-amino-poly-carboxylate ligands (e.g., DTPA, DOTA), form stable, water-soluble complexes approved for intravenous use [51, 53]. Chelates reduce free-ion toxicity because Gd^{3+} is a strongly electropositive heavy metal that can interfere with cellular channels and bind to endogenous proteins or phospholipids. The stable complex with Gd^{3+}, conferring both thermodynamic and kinetic stability. Furthermore, by selecting the appropriate chelator, biodistribution can be controlled by tuning the physicochemical properties of the complex, according to the intended application. GBCAs are classified by distribution: *extracellular* agents (rapid distribution in plasma and interstitium, renal elimination) for CNS tumor enhancement and angiography; *blood* agents (e.g., albumin binding formulations) for prolonged intravascular contrast; and *hepatobiliary* agents with partial hepatic uptake for liver lesion characterization [51, 40].

Mechanistically, Gd^{3+} increases r_1 and r_2 of nearby water protons by modulating fluctuating local magnetic fields, shortening both T_1 and T_2 [53, 51]. On standard T_1-weighted sequences at clinical concentrations, the T_1 effect dominates: tissues with higher Gd^{3+} concentration appear *hyperintense* (positive contrast) [51, 49]. Limitations include the enhancement which is indirect and nonspecific, quantification which is difficult and usually requires subtraction imaging. High cellular loading raises safety concerns; these constraints have motivated alternative reporters such as SPIO and ^{19}F probes for quantitative adoptive cell tracking [45, 4, 39]. Nevertheless, in clinical neuro-oncological imaging, GBCAs remain essential for lesion detection and delineation, as illustrated in Figure 1.8. [54].

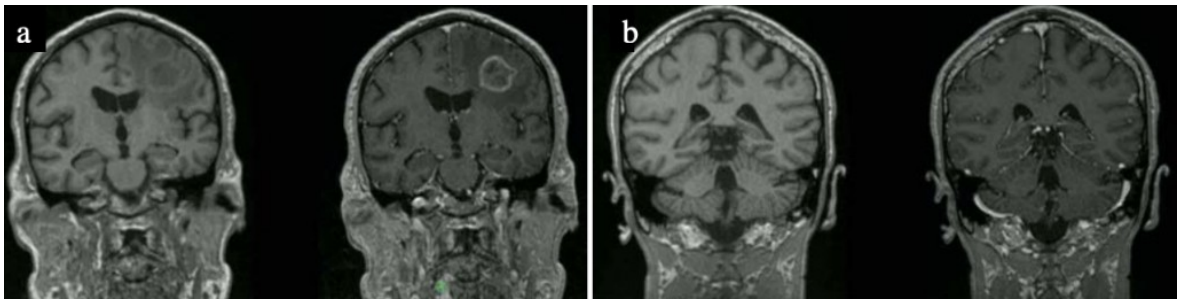

Figure 1.8: Glioblastoma (a) and metastasis (b) on coronal T_1-weighted MRI before (left) and after (right) administration of gadolinium-based contrast agent (Gd-CA). Post-contrast enhancement delineates pathological regions that are poorly visible on pre-contrast images. Reproduced from [54].

1.4.3 Cell Labeling with Superparamagnetic Iron Oxide Nanoparticles (SPIO, USPIO, MPIO)

Superparamagnetic iron oxide nanoparticles (SPIO) are nanometric particles with magnetite or maghemite cores (magnetic iron oxides) stabilised by dextran, carboxydextran or related coatings, for colloidal stability. [55, 56, 57]. They are the classical *negative* (T_2/T_2^*) contrast agents for MRI cell tracking, where labelled regions appear darker (hypointense). [57, 45].

Because MRI signal depends on how rapidly water proton magnetisation relaxes, SPIO are used chiefly to accelerate T_2 and T_2^* relaxation in their microenvironment, quantified by elevated transverse relaxivities r_2 and r_2^* [49, 55]. When the magnetic core is smaller than the size of bulk iron, the energy barrier for reorienting the particle magnetic moment becomes comparable to thermal energy at body temperature; the moment therefore fluctuates stochastically in direction, a regime termed *superparamagnetism* [55, 57]. This behaviour generates microscopic field gradients around nearby water protons, which rapidly dephase the transverse magnetisation (M_{xy}) and shorten T_2 and T_2^*; on T_2- or T_2^*-weighted images, labelled tissue consequently appears hypointense [57, 45].

Formulations are commonly grouped by hydrodynamic size and biodistribution: **SPIO** ($\gtrsim$50 nm; strong T_2^* contrast, hepatic, splenic and macrophage imaging), **USPIO** ($\sim$20–50 nm; prolonged blood half-life), and micron-scale **MPIO** (high iron payload per particle but limited uptake by non-phagocytic cells, such as lymphocytes) [57, 55]. In adoptive immunotherapy, cells are usually labelled *ex vivo* by endocytosis [45, 4]. As reviewed by Mali *et al.*, proton MRI detects iron indirectly through relaxation effects, so cell number is difficult to quantify, label is diluted with proliferation, hypointense voids can confound interpretation by mimicking haemorrhage or susceptibility artefacts (Figure 1.9) [57, 45, 58], motivating direct ^{19}F reporters treated in the next subsection.

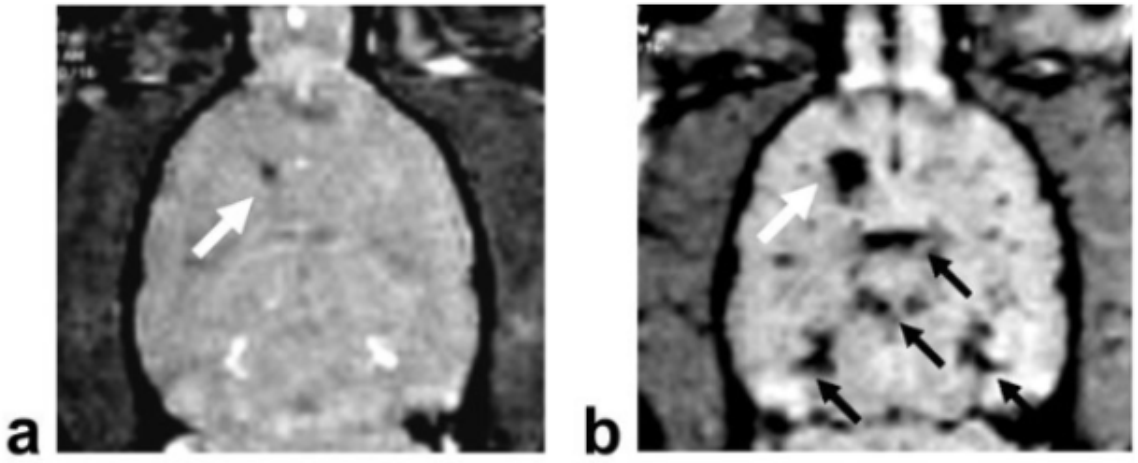

Figure 1.9: MRI findings of BBB opening and brain hemorrhage. Pictures were drawn from a rat sonicated with an acoustic pressure of 1.9 MPa. **a**: T_2^*-weighted images before SPIO injection showing the occurrence of brain hemorrhage (arrow). **b**: T_2^*-weighted images with SPIO enhancement showing an extensive region of BBB disruption (arrow). Reproduced from [58].

The use of iron oxide nanoparticles has been among the earliest and most established approaches to cellular labelling for MRI-based monitoring.

1.4.4 ^{19}F-MRI

Fluorine-19 magnetic resonance imaging (^{19}F-MRI) is a variant of MRI, in which the detected signal originates from the ^{19}F nucleus, rather than from the protons of tissue water that dominate clinical ^{1}H-MRI [50, 46, 52]. Natural fluorine comprises a single stable isotope, ^{19}F ($I = 1/2$, 100% abundance), which is NMR active and possesses a gyromagnetic ratio close to that of the proton ($\gamma/2\pi \approx 40.08\,\mathrm{MHz\,T^{-1}}$ for ^{19}F versus $\approx 42.58\,\mathrm{MHz\,T^{-1}}$ for ^{1}H) [46, 48]. In biomedical applications, ^{19}F-MRI is almost always performed after administration of an *exogenous* fluorinated contrast agent or after *ex vivo* loading of cells with a fluorinated probe; the resulting images map the spatial distribution of fluorine introduced into the body, typically as perfluorocarbon (PFC) emulsions, highly fluorinated small molecules or fluorinated nanoparticles [46, 59, 57].

At the level of nuclear magnetic resonance physics, ^{19}F-MRI does not rely on a different imaging mechanism from ^{1}H-MRI: in both cases, spins align along the main field $\mathbf{B}_0$, are tipped into the transverse plane by an RF pulse at the Larmor frequency $f_0 = \gamma B_0/(2\pi)$ (Equation 1.1), undergo T_1 and T_2 relaxation and are spatially encoded by magnetic field gradients before Fourier reconstruction [48, 46]. What changes is the observed nucleus and, consequently, the origin of image contrast. Clinical ^{1}H-MRI exploits the enormous proton pool of water and macromolecules, with contrast shaped by ρ, T_1, T_2, diffusion D and susceptibility χ; exogenous ^{1}H contrast agents (gadolinium chelates, SPIO) modulate the proton signal *indirectly* through relaxation of neighbouring water molecules [49, 45]. In ^{19}F-MRI, by contrast, the imaged signal

belong to the administered fluorinated probe itself: signal intensity reflects the local concentration of ^{19}F nuclei (and their relaxation behaviour), not the modulation of tissue water [46, 59].

Operationally, several differences follow from this distinction [52, 46]. First, dedicated RF hardware is required because the ^{19}F resonance frequency differs from that of protons at the same field strength (for example, at 3 T, $f_0 \approx 123$ MHz for ^{1}H and ≈ 117 MHz for ^{19}F). Second, ^{1}H decoupling or selective excitation is often applied during ^{19}F readout to simplify spectra when probes contain many chemically equivalent fluorines. Third, intrinsic sensitivity per nucleus is slightly lower for ^{19}F than for ^{1}H because of the smaller gyromagnetic ratio, but the dominant limitation in vivo is the extremely low concentration of endogenous fluorine in soft tissues, typically in the micromolar range or below for free fluoride, with most signal arising from insoluble deposits in bone and teeth. [46, 52]. Detectable ^{19}F-MRI therefore requires high local fluorine payload in labeled cells or concentrated nanoemulsions; Amiri *et al.* estimate that, for human studies at 1 cm^3 resolution, tissue concentrations on the order of a few millimoles per litre of ^{19}F per voxel may be needed within reasonable scan times [52]. Fourth, unlike SPIO-based tracking, ^{19}F-MRI does not create susceptibility voids on ^{1}H images: labeled cells appear as discrete positive signal on the fluorine channel, while anatomy is read from the proton channel in a dual-nuclei examination [45, 46].

Advantages and limitations. The principal advantages of ^{19}F-MRI for cell tracking are summarized in Table 1.2 [46, 60, 57, 52]. (*i*) **Negligible endogenous background** in soft tissues yields high specificity. Indeed, signal above the detection threshold is attributable to the fluorinated label rather than to native tissue chemistry, avoiding false positives from haemorrhage, calcification or air–tissue interfaces that confound SPIO hypointensities [46, 45]. (*ii*) **Direct quantitative detection**, because ^{19}F signal is linearly related to the number of fluorine atoms in a voxel after coil sensitivity correction and calibration against a reference phantom, enabling estimation of cell number or fluorine load *in vivo*, which is a capability that ^{1}H-MRI indirect labels only approximate semi-quantitatively [60, 52, 59]. (*iii*) **No baseline subtraction** is required, unlike many Gd^{3+}-based strategies. (*iv*) **No ionizing radiation** is involved, supporting repeated longitudinal imaging in the same subject. (*v*) **Multiplexing (Wide chemical shift range(> 350 ppm))** is possible when probes with distinct ^{19}F chemical shifts (e.g., different PFCs) are used, allowing simultaneous tracking of multiple cell populations in one session [46, 61]. (*vi*) **Compatibility with clinical MRI infrastructure** is improving through dual-tuned coils and combined ^{1}H/^{19}F sequences, as demonstrated for CAR-T and dendritic cell tracking in recent preclinical and translational work [47, 52].

Important limitations must also be acknowledged. Sensitivity remains the main

hurdle towards routine clinical use, such as achieving adequate signal-to-noise ratio (SNR) in lymphocytes and other non-phagocytic cells, which demands efficient *ex vivo* labeling, high fluorine content per cell, developing more performing fluorinated tracer, optimized T_1/T_2 properties of the probe and tailored acquisition schemes (dedicated coils, short echo times or spectroscopic imaging approaches and recent advances in MRI technology) [52, 57]. Moreover, label is diluted with cell division, shortening the window for detection [45, 39]. Residual extracellular nanoparticles or free probe can generate spurious ^{19}F signal that mimics intracellular label, because co-acquired anatomical ^{1}H-MRI by itself does not distinguish intracellular from extracellular fluorine. For this reason, in the context of *ex vivo* cell labeling, purification from free nanoparticles is rigorous. [52].

Table 1.2: Comparison of ^{19}F-MRI with proton-based cell labeling for adoptive cell tracking (adapted from [46, 45, 52, 57]).

Feature	**^{1}H-MRI with SPIO/Gd labels**	**^{19}F-MRI with fluorinated probes**
Signal source	Indirect: modulation of tissue water ^{1}H signal	Direct: ^{19}F spins in the label
Endogenous background	Strong proton signal from all tissues	Negligible in soft tissues at liquid state concentrations
Image appearance	Hypointense voids (SPIO) or hyperintense enhancement (Gadolinium) on ^{1}H images	Positive "hot spots" on ^{19}F channel; anatomy from co-acquired ^{1}H
Quantification	Semi-quantitative, confounded by indirect detection	Signal $\propto$ number of ^{19}F atoms
Typical artefacts	Susceptibility blooming, confusion with haemorrhage or post-operative changes	Low SNR if under-loaded; extracellular label; dilution with proliferation
Radiation	None	None

The central motivation for ^{19}F-MRI in adoptive cell therapy is to obtain a specific, potentially quantitative readout of labeled therapeutic cells without the confounders that limit proton-based negative or positive contrast strategies [45, 60, 52]. After direct labeling, cells internalize a fluorinated cargo that remains intracellular for a finite period; only sites containing sufficient ^{19}F atoms generate signal, producing "hot spot" maps of cell localization that can be co-registered with anatomical ^{1}H images acquired in the same session [46, 47, 39]. This approach has been applied to dendritic cells, macrophages, stem and progenitor cells, and, more recently, CAR-T and other lymphocyte products, both in preclinical models and in early translational studies or for clinical use (Clinical Trial ID: NCT05366179). [59, 61, 47, 57]. In the following Figure 1.10, it is shown fluorinated probes that have been widely used for imaging inflammatory activity by in *in vivo* labeling following systemic administration. Indeed, nanoformulations of fluorinated probes are avidly taken up by phagocytes as leukocytes that are highly present in injured tissues or organs with an immune reaction [62, 59, 52].

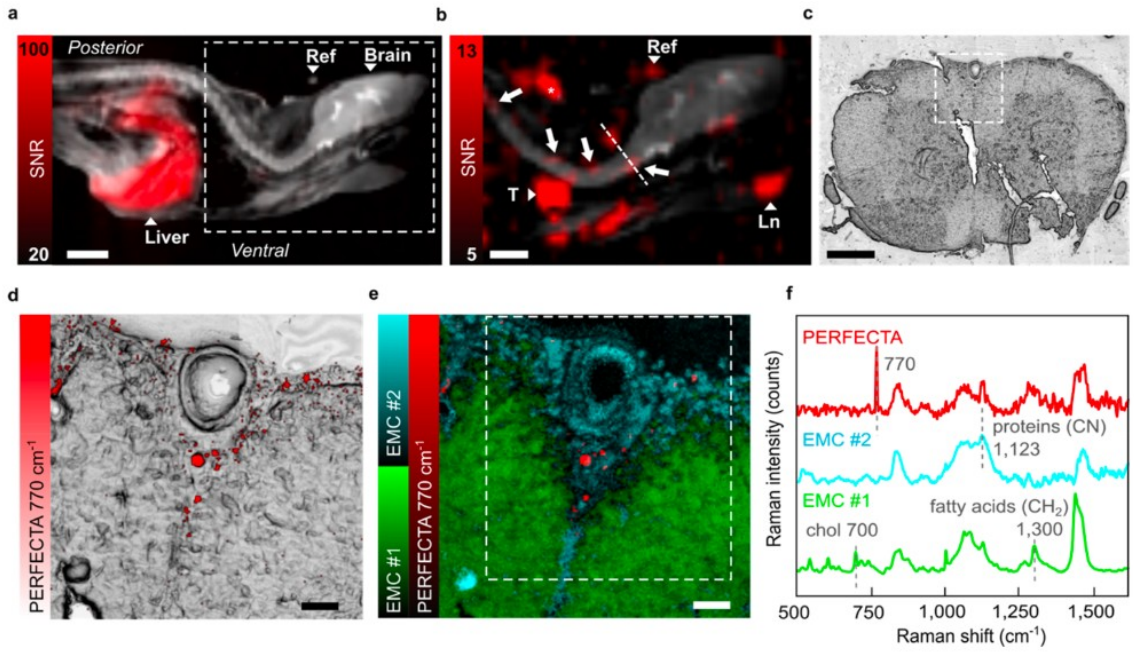

Figure 1.10: A Bioorthogonal Probe for Multiscale Imaging by ^{19}F-MRI and Raman Microscopy (Chirizzi *et al.* [63]). **(a–b)** Sagittal mouse overlays of ^{19}F signal (red) on co-acquired ^{1}H anatomy (grey). **(c)** Bright-field image of a tissue section with the dashed box marking the Raman field of view. **(d–e)** Raman maps localizing PERFECTA and a composite view separating probe signal from major endogenous tissue contributions. **(f)** Representative Raman spectra used to assign the probe. The purpose is to bridge *in vivo* MRI localization with micrometre-scale Raman readout on the same fluorinated agent, without a separate fluorescent or radioactive label.

1.5 Fluorinated Probes and Polymeric Nanoparticles

Effective monitoring of adoptive cell therapy by ^{19}F-MRI requires reinfused lymphocytes to carry a high intracellular ^{19}F payload that is retained by viable effector cells throughout purification and after infusion. The choice of probe type, fluorine content per particle, labelling efficiency, cytotoxicity and retention during proliferation, defines how transferred cells can be localized and quantified *in vivo*. The following subsections review the main Perfluorocarbons (PFC)-based platforms and polymeric carriers used for this purpose, with particular focus to PERFECTA and to PLGA-based nanoformulations developed for efficient cell labelling and ^{19}F-MRI detection.

Linear and cyclic PFC molecular tracers. Perfluorocarbons are fully fluorinated compounds with hydrocarbons backbone (in which all hydrogens have been substituted by fluorine), with very low water solubility. For ^{19}F-MRI they are almost always formulated as oil-in-water nanoemulsions or encapsulated in polymer shells [64, 59]. Beyond enabling aqueous dispersion, this class is attractive because very strong carbon–fluorine bonds confer substantial thermal, chemical and oxidative stability, while the high electronegativity of fluorine, low polarizability of C–F motifs and comparatively weak intermolecular interactions jointly support a chemically inert profile at physiological pH.

Moreover, perfluorocarbon liquids dissolve respiratory gases far more efficiently than aqueous media, which has motivated oximetry-oriented protocols in which oxygen-dependent relaxation or spectroscopic signatures are read together with anatomical localization, to define tumor-area variations based on the low oxygen levels. The following molecular PFCs have dominated preclinical cell-tracking studies for decades:

- **Perfluorooctyl bromide (PFOB)** is a linear C_8 perfluoroalkyl-bromide bearing 17 fluorine atoms in several distinct chemical environments. It therefore produces a complex ^{19}F-NMR spectrum with multiple resonances, lower effective sensitivity per unit concentration and broader Raman features than symmetric probes [64, 63]. PFOB emulsions stabilized with phospholipids or Pluronic surfactants (typically 100–280 nm) have been used extensively for macrophage and stem-cell tracking [61, 59].

- **Perfluoro-15-crown-5-ether (PFCE)** is a macrocyclic ether with 20 chemically equivalent fluorine atoms, giving a single sharp ^{19}F-NMR signal (around -92 to -92.5 ppm) and favourable spin-lattice relaxation for imaging [64, 65]. PFCE nanoemulsions (often 150–250 nm) represent one of the best characterized platforms for immune cell labelling and have been formulated with lecithin, Pluronic or semi-fluorinated block copolymers at high fluorine loadings (up to $\sim$35% v/v in advanced preparations) [65, 61]. Multiplexed ^{19}F-MRI is possible when PFCE is combined with probes resonating at a distinct chemical shift, such as PERFECTA [62, 61].

- **Perfluoropolyethers (PFPE)** and related linear fluorinated oils extend the chemical space of PFC tracers and are often incorporated into polymer nanodroplets or micelles for cell labelling and targeted delivery [64, 57]. Across all PFC classes, the common formulation strategy is an oil-in-water emulsion in which the hydrophobic fluorocarbon core is surrounded by a surfactant corona,classically phospholipids (e.g., lecithin), non-ionic block copolymers (Pluronic F-68 or F-127), or mixtures with cholesterol and auxiliary lipids,to confer aqueous stability and control particle size between roughly 100 and 300 nm [64, 59].

1.5.1 PERFECTA as a ^{19}F-MRI molecular probe

PERFECTA (suPERFluorinatEd ContrasT Agent) is a symmetric, hyperbranched molecular probe, reporter with a single, intense NMR resonance peak (-73.4ppm) and a distinctive Raman signature (770 cm^{-1}) [66, 64]. Its systematic name is tetra(perfluoro-*tert*-butyl)pentaerythritol; the molecular formula is $C_{21}H_8F_{36}O_4$ (molecular weight 1008 Da) [62, 63]. The structure consists of a pentaerythritol core bearing four equivalent perfluoro-*tert*-butyl ether arms, yielding **36 magnetically equivalent ^{19}F nuclei** in a highly symmetric arrangement (Figure 1.11).

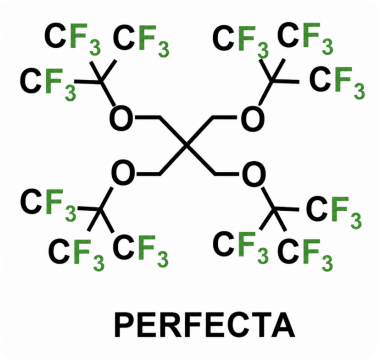

Figure 1.11: Chemical structure of PERFECTA (tetra(perfluoro-*tert*-butyl)pentaerythritol; suPERFluorinatEd ContrasT Agent).

PERFECTA was designed as "superfluorinated" contrast agent combining a high fluorine density with molecular rigidity and symmetry, properties that maximize ^{19}F-MRI sensitivity and simplify spectral detection [66, 64]. Like other PFCs, PERFECTA is hydrophobic and must be formulated as a core in nanovector for aqueous or biological use [67, 68][95, 96, 97].

The key physicochemical properties of PERFECTA compared with PFCE and PFOB are summarized in Table 1.3. PERFECTA exhibits a single sharp ^{19}F-NMR signal at -73.4 ppm (referenced to trifluoroacetic acid, TFA), whereas PFCE resonates near -92.5 ppm and PFOB shows multiple resonances [63, 62]. The integrated signal intensity scales linearly with fluorine concentration and is substantially higher than that of PFCE or PFOB at matched molar doses, because all 36 fluorines contribute coherently to one resonance [63, 64].

In Pluronic F-68 nanoemulsions ($\sim$200–250 nm) [62], PERFECTA nanoformulations display colloidal stability for at least 15 days at 25 °C (PDI < 0.2) and remain stable in biological fluids for at least 72 h at 37 °C [63]. At 7 T and 20 °C, relaxometry on emulsified probes gave $T_1 \approx 690$ ms and $T_2 \approx 202$ ms for PERFECTA, compared with $T_1 \approx 1180$ ms and $T_2 \approx 610$ ms for PFCE at comparable fluorine concentration (4×10^{19} $19F$-atoms/mL) [62]. Shorter T_1 favours faster imaging sequences and improved sensitivity per unit time, an important practical advantage for cell-tracking protocols [67, 52].

A distinctive feature of PERFECTA is its intense, narrow Raman band at $\sim$770 cm^{-1}, assigned to C–F stretching and bending modes of the symmetric perfluoro-*tert*-butyl groups [63]. By contrast, PFOB and PFCE show broader, weaker Raman features (724 and 820 cm^{-1}, respectively) related to conformational flexibility [63]. Because mammalian tissues lack endogenous Raman signals in this region, PERFECTA enables **bioorthogonal multiscale imaging**: the same formulated probe can be detected by ^{19}F-MRI across the whole body and localized at cellular resolution by Raman microscopy on tissue sections, without requiring a second fluorescent or radioactive label [63], as seen in Figure 1.12. Multiplexed Raman/^{19}F-MRI has been demonstrated by

labelling different cell populations with PERFECTA- and PFCE-based nanoemulsions [63, 62], demonstrating the superiority of PERFECTA as a contrast agent.

Table 1.3: Representative properties of common fluorinated ^{19}F-MRI probes (compiled from [64, 62, 63]).

Probe	Formula / type	Equivalent ^{19}F	δ (ppm)	T_1 / T_2 (7 T, 20 °C)
PERFECTA	$C_{21}H_8F_{36}O_4$; branched	36	−73.4	∼690 / ∼202 ms†
PFCE	Macrocyclic ether	20	∼ −92.5	∼1180 / ∼610 ms†
PFOB	Linear C_8 perfluoroalkyl Br	17 (non-equivalent)	Multiple	Variable

†Measured on Pluronic F-68 emulsions at 4×10^{19} $19F$-atoms/mL [62].

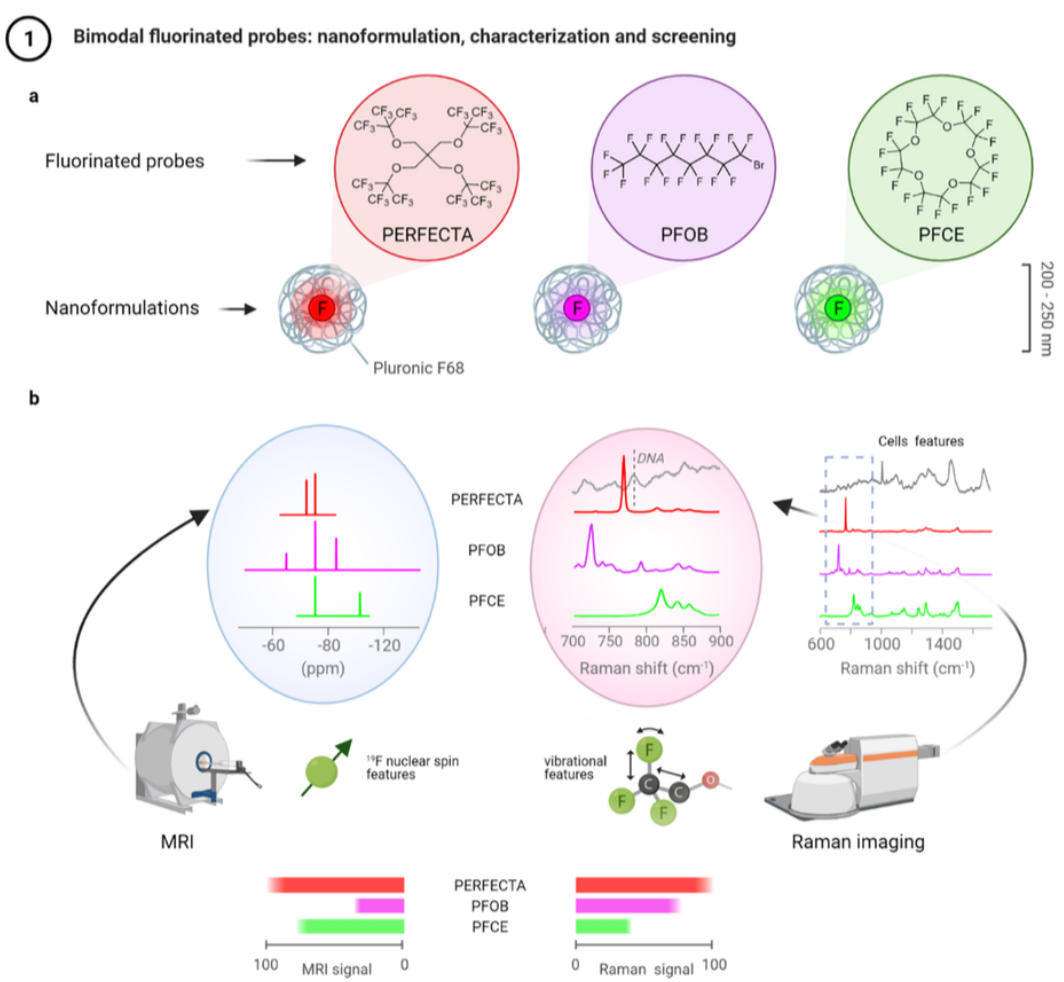

Figure 1.12: Bimodal fluorinated probes: nanoformulation, characterization and screening (Chirizzi *et al.* [63]). **(a)** Chemical structures of PERFECTA, PFOB, and PFCE, and their formulation into Pluronic F-68 nanoformulations with diameters of about 200–250 nm. **(b)** Comparison of imaging properties: ^{19}F-MRI spectra (left) and Raman spectra highlighting probe vibrational features versus cellular background (right), with bar charts summarizing relative MRI and Raman signal strengths across the three probes.

1.5.2 PLGA-based nanoformulations for ^{19}F-MRI Imaging

Poly(lactic-co-glycolic acid) (PLGA) is the most widely used polyester because it is biodegradable, FDA-approved in several device and drug formulations [67, 69]. Chem-

ically, PLGA is a random copolyester obtained by ring-opening polymerization of lactide and glycolide, with a backbone of ester repeat units derived from lactic acid (−[O-CH(CH_3)-CO]−, $C_3H_4O_2$) and glycolic acid (−[O-CH_2-CO]−, $C_2H_2O_2$). Its hydrolytic degradation produces biocompatible lactate and glycolate metabolites, limiting long-term retention of the carrier after labelling or administration. The lactide/glycolide ratio can be tuned to modulate hydrophobicity, glass-transition temperature and degradation kinetics, so that release of a hydrophobic cargo such as PERFECTA can be matched ^{19}F-MRI-acquisition time and clereance request. Unlike liquid perfluorocarbon emulsions, the polymeric core defined a matrix that can protect the fluorinated cargo, modulate release and clearance and tune biodistribution, through polymer chemistry and surface coating [57, 60]; different coating types are used for optimize control of colloidal stability, charge and cellular uptake, without chemically modifying the fluorinated payload [67, 70, 57, 69].

For adoptive cell therapy, the ideal fluorinated carrier must deliver a high intracellular ^{19}F load without compromising viability or effector function of cells.

Upon contact with biological fluids, nanoparticles rapidly adsorb proteins from the surrounding medium; this adsorbed layer is termed the **protein corona (PC)** because it forms a protein shell around the particle surface. The PC confers a biological behaviour to the nanocarrier that promotes recognition by cells and can trigger endocytic pathways, thereby modulating nanoparticle uptake [70] (Figure 1.13).

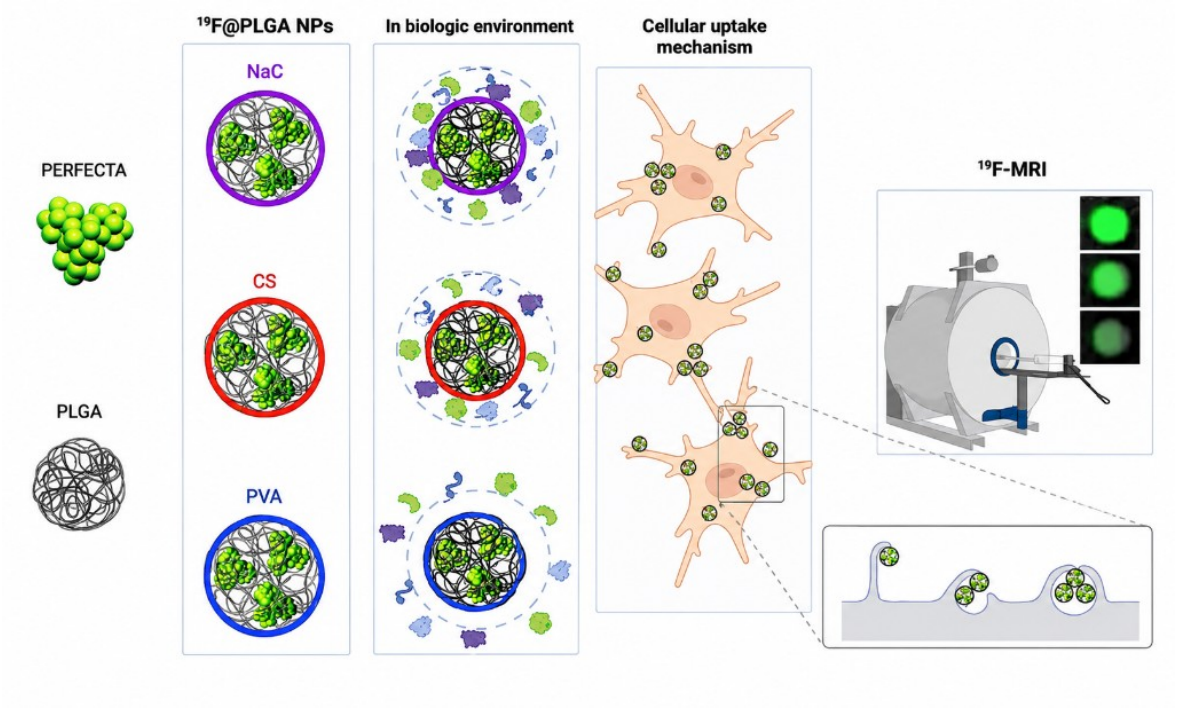

Figure 1.13: Schematic representation of the components used to produce ^{19}F–PLGA NPs containing the superfluorinated probe (PERFECTA) and coated by different stabilizers. The obtained ^{19}F–PLGA NPs show a different behaviour in the biological environment with a diverse tendency to form the protein corona (PC). The PC modulates cell labelling efficiency through different internalization pathways and has a significant impact on ^{19}F-MRI sensitivity (adapted from Chirizzi *et al.* [70]).

Three PERFECTA-PLGA NP formulations based on different biocompatible stabilizers were developed, optimized, and compared to investigate their effects on cellular responses.(Table 1.4) [67, 70].

Table 1.4: Physicochemical properties of PERFECTA@PLGA NPs stabilized with different surfactants (mean ± SD; adapted from [67, 70]).

Formulation	D_H (nm)	PDI	ζ (mV)	Encapsulation (%)
PERFECTA@PLGA–NaC	104 ± 10	0.20 ± 0.03	-49 ± 5	48 ± 10
PERFECTA@PLGA–PVA	206 ± 9	0.12 ± 0.03	-13 ± 1	61 ± 12
PERFECTA@PLGA–CS	215 ± 51	0.16 ± 0.06	$+19 \pm 8$	47 ± 9

Sodium cholate (NaC; formula $C_{24}H_{39}NaO_5$; molecular weight 430.55 g/mol; purity $\geq$ 99%, typically derived from bovine/ovine bile; 0.6% w/v aqueous phase) is an anionic bile salt that produces the smallest NPs ($\sim$100 nm) with strongly negative surface charge. NaC-stabilized particles are preferentially internalized by phagocytic cells (BV-2 microglia, macrophages lines in [67, 70]) through pathways dominated by phagocytosis and clathrin/caveolin-mediated endocytosis, showing the brightest ^{19}F-MRI signal per cell in vitro [67, 70]. NaC formulations also show favourable T_1 relaxation ($\sim$260–350 ms) and long T_2 ($\sim$200 ms), supporting rapid and sensitive acquisition [67, 70]. This enhanced labelling performance is plausibly linked to the ability of these nanoparticles to promote formation of a stable, well-structured protein corona, which in turn favours greater cellular uptake and, consequently, a stronger ^{19}F-MRI signal. The same behaviour has also been validated in other non-phagocytic cell types, including murine and human neural stem cell precursors, cells already explored as an experimental therapeutic strategy in multiple sclerosis [70]. For this reason, NaC-PERFECTA@PLGA is the formulation of choice for *ex vivo* labelling of CAR-T cells and other immune effectors in culture, where maximal intracellular fluorine loading per incubation period is paramount.

Poly(vinyl alcohol) (PVA, 2% w/v aqueous phase) is the classical emulsion stabilizer for injectable PLGA NPs and is widely use for systemic administration [67, 57]. PVA-coated PERFECTA@PLGA NPs are larger ($\sim$200 nm), more neutral in charge ($\zeta \approx -13$ mV), and achieve the highest PERFECTA encapsulation efficiency (up to $\sim$61%), with low PDI [67]. Although cellular uptake is lower than for NaC NPs in static culture, PVA-NPs form a well defined protein corona in serum supplemented media that can enhance phagocytic recognition and improve labelling performance under physiologically relevant conditions [70]. Accordingly, PVA-PERFECTA@PLGA NPs are preferred for *in vivo* studies and for protocols in which nanoparticles are administered systemically before or after cell infusion, whereas NaC NPs are optimized for direct *ex vivo* contact with therapeutic cells.

Chitosan (CS) introduces a mildly positive surface charge and represents an intermediate strategy to promote electrostatic interactions with the cell membrane; uptake

and relaxation properties lie between NaC and PVA formulations [70].

Encapsulated PERFECTA retains its single peak ^{19}F-NMR signature inside PLGA, confirming that the probe is not chemically degraded during fabrication [67]. In vitro labelling of BV-2 cells with NaC-PERFECTA@PLGA at $\sim 10^{14}$ 19F-atoms/cell for 4 h produced clearly detectable cell pellets on 7 T ^{19}F-MRI, with viability comparable to untreated controls [67]. Subsequent work demonstrated that protein-corona formation on PVA- and NaC-coated NPs in cell-conditioned medium, in presence of Fetal Bovine Serum, FBS, can further modulate uptake; emphasizing the need to characterize NPs in the same media used for CAR-T culture. [70] (Figure 1.14).

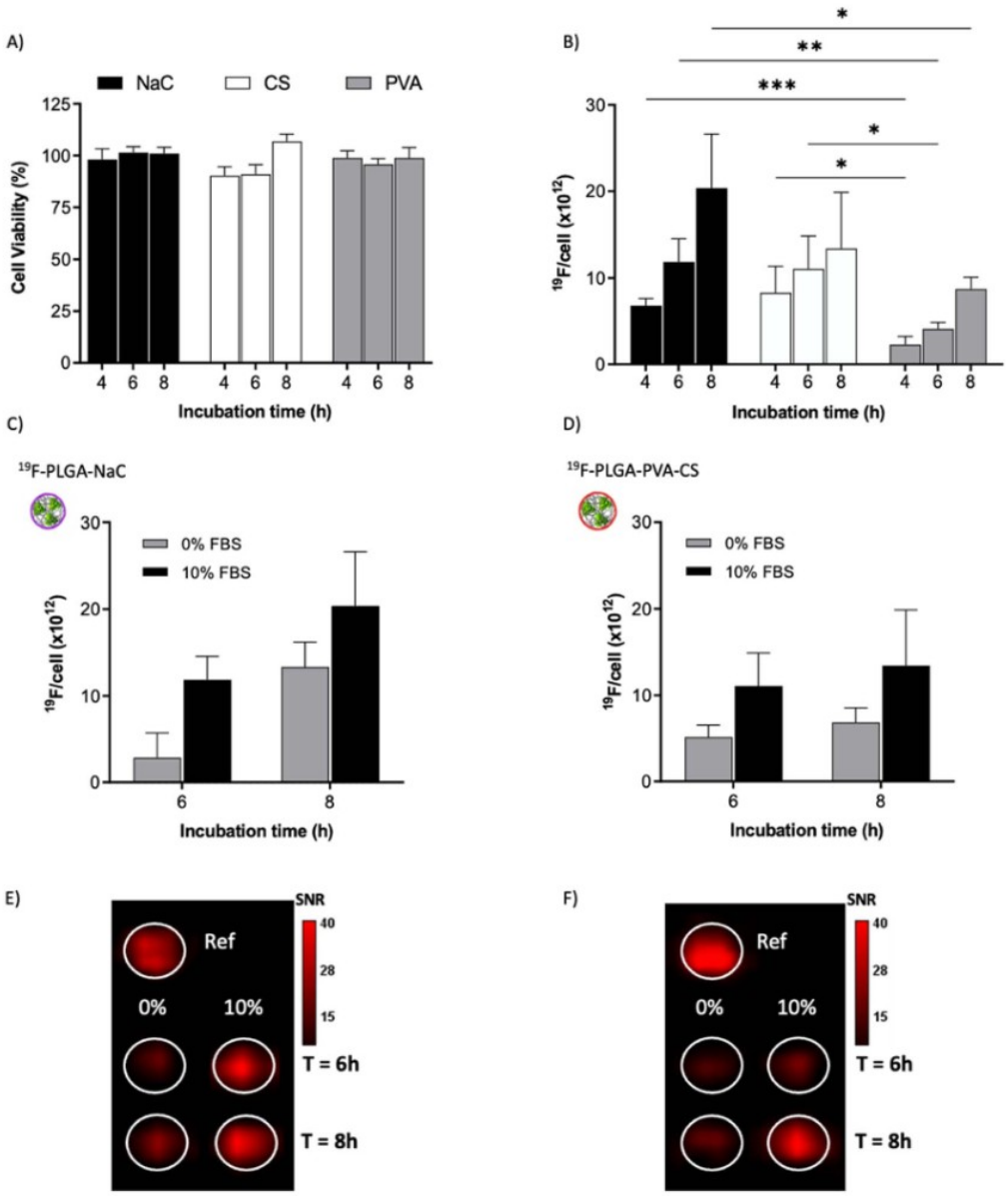

Figure 1.14: In vitro direct cell-labelling study comparing PERFECTA@PLGA nanoparticles stabilized with sodium cholate (NaC), chitosan (CS), or poly(vinyl alcohol) (PVA) in murine BV-2 microglial cells (adapted from Chirizzi *et al.* [67, 70]). **(A)** Biocompatibility assessed by trypan blue exclusion: viability of labelled cells after 4, 6, and 8 h incubation, normalized to unlabeled controls. **(B)** Time-dependent intracellular ^{19}F loading quantified by ^{19}F-MRI (^{19}F atoms per cell). **(C–D)** Labelling efficiency in DMEM supplemented with 0% or 10% fetal bovine serum (FBS) for PERFECTA@PLGA–NaC **(C)** and PERFECTA@PLGA–PVA–CS **(D)**. **(E–F)** Representative ^{19}F-MRI phantoms of cell pellets labelled under the same FBS conditions (250 000 cells per sample; external reference = 5×10^{19} ^{19}F atoms).

The NaC-PERFECTA@PLGA platform developed in these studies to optimize ex vivo CAR-T cell labeling provided the methodological basis for the experimental work described in the Materials and Methods and Results chapters of this thesis.

Chapter 2

Materials and Methods

Experimental activities were distributed between two institutions. Nanoparticle formulation and physicochemical characterization were performed at Politecnico di Milano (Department of Chemistry, Materials, and Chemical Engineering "Giulio Natta"; SupraBioNanoLab, Prof. Francesca Baldelli Bombelli). *In vitro* biological experiments on CAR-T cells were conducted at Fondazione IRCCS Istituto Neurologico Carlo Besta (Milan), Division of Neuro-immuno-oncology (laboratory of Prof.ssa Serena Pellegatta), under the supervision of Dr. Cristina Chirizzi and the scientific guidance of Prof. Serena Pellegatta. ^{19}F-MRI acquisitions at 7 T were performed at the Division of Neuro-radiology and 7T-MRI of the same institution.

2.1 Materials

2.1.1 Chemicals and reagents

Solvents

The solvents used for nanoparticle formulation and physicochemical characterization are listed in Table 2.1.

Table 2.1: Solvents used in this research work.

Material	**Specification**	**Supplier (country)**
Ethyl acetate (EtOAc)	Purity $\geq$ 99.5%	Sigma-Aldrich (Germany)
Ultrapure water (mQ_w)	Type I; 18.2 mΩ/cm	Simplicity® system (Merck, Germany)
Deuterium oxide (D_2O)	99,9 atom %D for ^{19}F-NMR standard	Sigma-Aldrich (Germany)

Nanoparticle formulation

Materials for PERFECTA@PLGA nanoparticle preparation are summarized in Table 2.2.

Table 2.2: Materials for nanoparticle formulation.

Material	Specification	Supplier
Poly(lactide-co-glycolide)(PLGA)	Resomer® 502H; lactide:glycolide 50:50; 7–17kDa; acid terminated	Sigma-Aldrich (Germany)
Sodium cholate (NaC)	0.6% w/v aqueous phase	Sigma-Aldrich (Germany)
PLGA–Rhodamine B	Lactide:glycolide 50:50; 10–30 kDa; 3.12 µg/mg dye	Sigma-Aldrich (Germany)
PERFECTA	Synthesized by SupraBioNanoLab, Politecnico di Milano, according to Tirotta *et al.* [66]	—
Sodium fluoride (NaF)	$M_w = 41,98$ g/mol; Reference for ^{19}F-NMR	Sigma-Aldrich (Germany)
Trifluoroacetic acid (TFA)	CF_3COOH; $M_w = 114.02$ g/mol; $\delta = -75.5$ ppm; Reference for ^{19}F-MRI	Sigma-Aldrich (Germany)

2.1.2 Cell lines and biological materials

Human B7-H3-targeting CAR-T cells were generated at the Division of Neuro-immuno-oncology, Fondazione IRCCS Istituto Neurologico Carlo Besta, from peripheral blood mononuclear cells (PBMCs) of healthy donors [16, 15]. For cytotoxicity assays, U87-MG glioblastoma neurospheres were used as target cells. NIH-3T3 mouse embryonic fibroblasts were used to optimize the protocol for conditioned medium for protein corona stability assays (Table 2.3).

Table 2.3: Cell lines and biological materials used in *in vitro* experiments.

Biological material	Description / Culture conditions	Source
Human CAR-T cells	Anti-B7-H3 CAR; expanded in TCM ± IL-7/IL-15; used 7–12 days post-transfection	FINCB (Pellegatta Group)
U-87 MG cells	Adherent glioblastoma line; expanded in DMEM/F12–GlutaMAX™ + 10% FBS, 1% NEAA, 1% P/S, 0.4% fungizone;	ATCC
NIH-3T3 cells	Adherent mouse embryonic fibroblast line (NIH Swiss); expanded in DMEM Gibco + 10% FBS + 1%P/S + 1%L-Glutamine; used for conditioned-medium preparation in protein corona assays	Cytion (cat. no. 400101)

CAR-T cell culture reagents

Culture media and supplements are listed in Table 2.4. T cell medium (TCM) was prepared as 44% Click's Medium, 44% RPMI-1640, 10% FBS-HyClone, 1% penicillin–streptomycin v/v, and 1% L-glutamine v/v. For T-cell expansion, TCM was supplemented with recombinant human interleukin IL-15 and IL-7 (1:20000 and 1:10000

respectively); labelling and functional assays were performed in TCM without cytokine supplementation.

Table 2.4: CAR-T cell culture reagents.

Material	**Specification**	**Supplier**
RPMI-1640 Medium (1X)	With 2.05 mM L-glutamine; sterile filtered	Cytiva HyClone™ (Logan, UT, USA)
Click's Medium	Eagle's MEM / Ham's amino acid BME; without $NaHCO_3$ and L-glutamine	Sigma-Aldrich (UK)
Fetal bovine serum (FBS)	Characterized; U.S. origin	Cytiva HyClone™ (Logan, UT, USA)
Fetal bovine serum (FBS), Gibco	Endotoxin $\leq$ 10 EU/mL; hemoglobin $\leq$ 25 mg/dL; triple 0.1 µm sterile-filtered	Gibco, Thermo Fisher Scientific (Waltham, MA, USA)
DMEM, Gibco	High glucose (4500 mg/L); without L-glutamine, sodium pyruvate, and HEPES; $NaHCO_3$ buffer ($\sim$44 mM);	Gibco, Thermo Fisher Scientific (Waltham, MA, USA)
Penicillin–streptomycin (P/S)	10 000 U/mL penicillin; 10 000 µg/mL streptomycin	Gibco, Thermo Fisher Scientific (Waltham, MA, USA)
L-Glutamine	200 mM	Gibco, Thermo Fisher Scientific (Waltham, MA, USA)
Human IL-15 and IL-7	For T-cell expansion only	—
Trypan Blue solution	0.4%; viability exclusion assay	Sigma-Aldrich (Germany)
Paraformaldehyde (PFA)	4% v/v in water; cell fixation before MRI analysis	Sigma-Aldrich (Germany)

Labelling, Purification and Staining reagents

Reagents for CAR-T labelling, purification, and flow cytometry staining are summarized in Table 2.5.

Table 2.5: Labelling, purification, and staining reagents.

Material	Specification / use	Supplier
MACS® labelling buffer	Cell staining and flow cytometry	Miltenyi Biotec (Bergisch Gladbach, Germany)
Anti-human CD3	PE-VIO conjugate	Miltenyi Biotec
Anti-human B7-H3 (276)	FITC conjugate	Miltenyi Biotec
Anti-human CSPG4 (NG2)	APC conjugate	Miltenyi Biotec
Viability™ 405/452 Fixable Dye	Viability staining	Miltenyi Biotec
Triton™ X-100	Laboratory grade; $\geq 99\%$; 2.5% in PBS for cell lysis (^{19}F-NMR)	Sigma-Aldrich (Germany)
Ficoll-Paque™	$\rho = 1.077 \pm 0.001\,\mathrm{g/mL}$ at 20 °C; endotoxin $< 0.12\,\mathrm{EU/mL}$; density gradient purification;	Cytiva (Uppsala, Sweden)
Percoll®	Colloidal liquid; $\rho = 1.135\,\mathrm{g/mL}$; low endotoxin ($2\,\mathrm{EU/mL}$); gradient density purification;	Cytiva
Phosphate-buffered saline (PBS)	pH 7.4 (10X)	Gibco, Thermo Fisher Scientic (Waltham, MA, USA)

Analytical and imaging equipment

Flow cytometry and preclinical ^{19}F-MRI were performed with the instruments listed in Table 2.6.

Table 2.6: Analytical and imaging equipment.

Instrument	Configuration / application	Location / supplier
MACSQuant® Analyzer 16	Flow cytometer; 488 nm laser, 579/34 nm filter for Rhodamine B detection; 405 nm laser, 450/50 nm Vio-Blue filter for Viability 405/452 detection; FlowLogic v7.1	Miltenyi Biotec; FINCB
Bruker BioSpec 70/20	Preclinical 7 T MRI; ^{19}F/^{1}H imaging; ParaVision 6	Bruker BioSpin; FINCB
Bruker Avance III HD 400	^{19}F-NMR; SampleXpress; probe 305 K; MestReNova	Bruker BioSpin; Politecnico di Milano

2.2 Nanoparticles Formulation

2.2.1 Emulsification solvent evaporation technique

The emulsification solvent evaporation technique is a widely used approach to prepare polymeric nanoparticles. [67, 69, 57]. The polymer and the hydrophobic cargo are dissolved in a volatile organic solvent to form the dispersed (oil) phase. This phase is emulsified into an aqueous continuous phase containing a surfactant, typically with magnetical stirring and sonication, which reduces droplet size. The stabilizer forms a surface coating on the droplets, which renders the particles dispersible in water as a colloidal suspension, because the outer layer is hydrophilic and charged and can interact favourably with water (e.g. hydrogen bonding). In addition, it imparts steric and electrostatic stabilization with surface charges, so that neighbouring nanoparticles repel each other and aggregation is reduced. PLGA@PERFECTA nanoparticles were fabricated following this general scheme reported below, based on the work of Chirizzi et al. [67, 70].

2.2.2 PERFECTA@PLGA nanoparticles stabilised with sodium cholate

PERFECTA (20 mg) is firstly dissolved in the organic solvent (1.5 mL of EtOAc) and heated up to 65 °C. It is then added to a solution of the same organic phase containing PLGA (20 mg). 24 mg of Sodium Cholate (NaC) are dissolved in 4 mL of aqueous solution. After the complete dissolution of the surfactant, the mixture of the organic solution containing both PERFECTA and PLGA is rapidly mixed by pipetting it up and down and dropwise added to the aqueous solution. The two solutions are then sonicated through a tip sonication at 60W for 25 seconds. The obtained solution is stirred magnetically for 3h at room temperature and then the excess of the organic phase is removed by rotary evaporation setting an initial pressure of 250 mbar and lowering by 10 mbar step until 70 mbar pressure at which it remains for 20 minutes. The suspension is finally washed in milliQ water (mQw) through centrifugation at 10733g for 40 minutes (4 °C), collected and re-suspended in 1 mL of mQw.

2.2.3 Fluorescent PERFECTA@PLGA-Rhodamine B nanoparticles

For uptake and flow-cytometry readouts, fluorescently labelled nanoparticles were prepared following the same protocol, with the addition of 2% (w/w) rhodamine B PLGA (lactide:glycolide 50:50; 10–30 kDa; Sigma-Aldrich, Germany) to the PLGA solution in

the organic phase. At present, this research work focuses on the NaC–PERFECTA@PLGA-RhodamineB formulation for *in vitro* experiments.

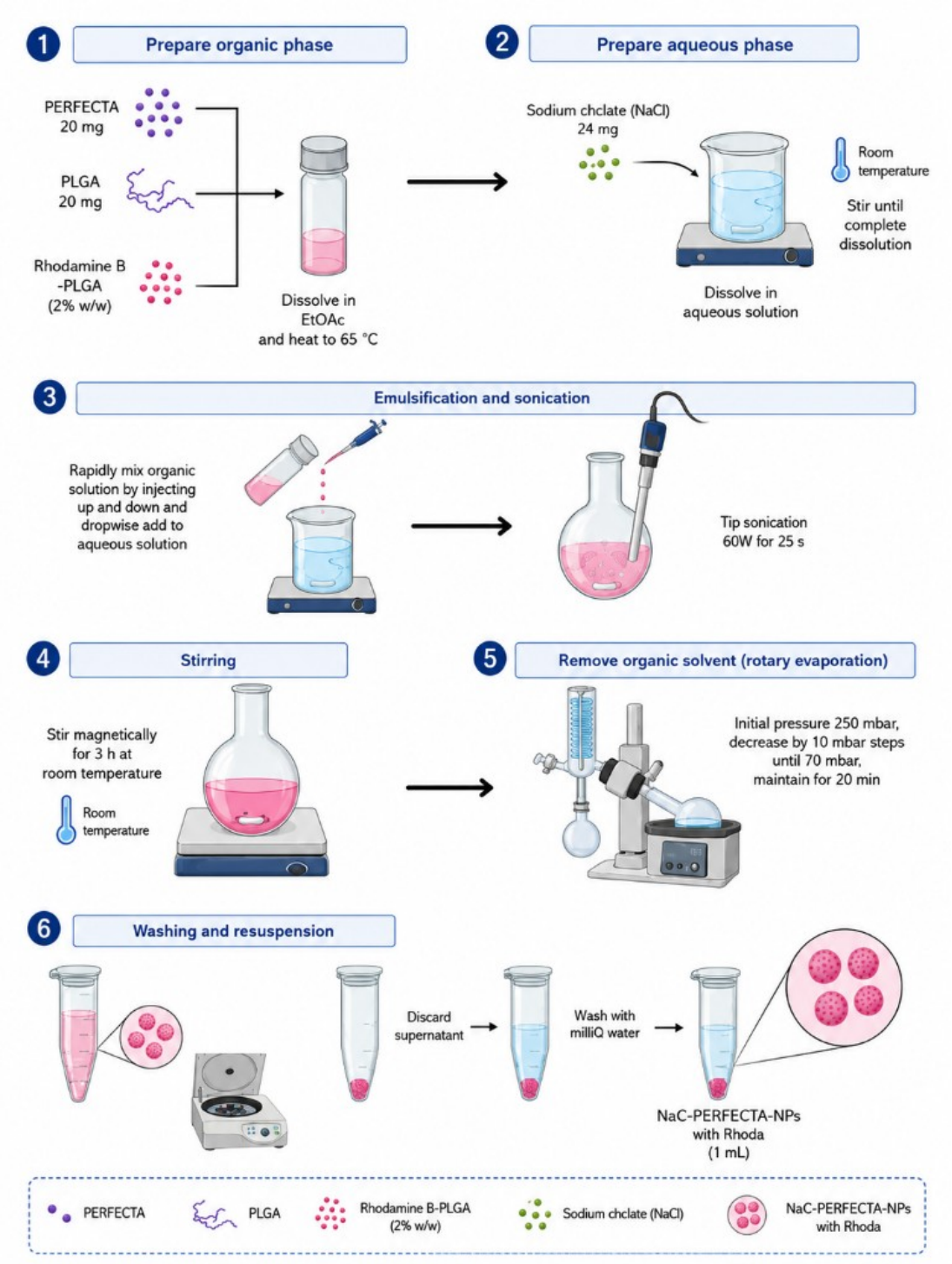

Figure 2.1: Schematic representation of the protocol for NaC–PERFECTA@PLGA nanoparticles: (1) organic phase (PERFECTA, PLGA, and fluorescent PLGA are dissolved in EtOAc, 65 °C); (2)sodium cholate is dissolved in the aqueous phase; (3) add dropwise organic phase in the aqueous phase for emulsification and tip sonication (60 W, 25 s); (4) magnetic stirring for 3 h, room temperature; (5) rotary evaporation of residual solvent (250 to 70 mbar) for 40min; (6) washing step by centrifugation at 10733g and resuspension in ultrapure water (1 mL).

2.3 Nanoparticles Formulation Scaling

To increase batch yield without modifying the established emulsification workflow, nanoparticle production was upscaled by a factor of four relative to the standard 1 mL batch described in Figure 2.1.

As shown in Figure 2.2, two round bottom flasks were processed in parallel, each yielding 2 mL of final nanoparticle suspension. For the NaC–PERFECTA@PLGA–Rhodamine-B formulations used in the *in vitro* experiments reported in this chapter, each flask was prepared as follows. For the organic phase, 40 mg of PERFECTA were dissolved in 3 mL of EtOAc, 39.2 mg of PLGA in 1.5 mL of EtOAc, and 0.8 mg of PLGA–Rhodamine-B in 1.5 mL of EtOAc (40 mg total PLGA, with 2% w/w fluorescent polymer). For the aqueous phase, 48 mg of NaC were dissolved in 8 mL of mQw. Emulsification, sonication, and magnetic stirring were carried out as in the standard protocol.

Before rotary evaporation, the contents of the two flasks can also be combined into a single batch (4mL total of final suspension volume), allowing the evaporation step to be performed in one run rather than separately for each flask, thereby reducing processing time and instrument occupancy. Evaporation was extended to approximately two to three times the standard duration to ensure complete removal of the organic solvent from the larger volume. For the washing step, the suspension was divided into aliquots of at most 8 mL per centrifuge tube to facilitate pellet recovery and resuspension in ultrapure water (mQw). The washed nanoparticles were finally resuspended in mQw and characterized by dynamic light scattering (DLS).

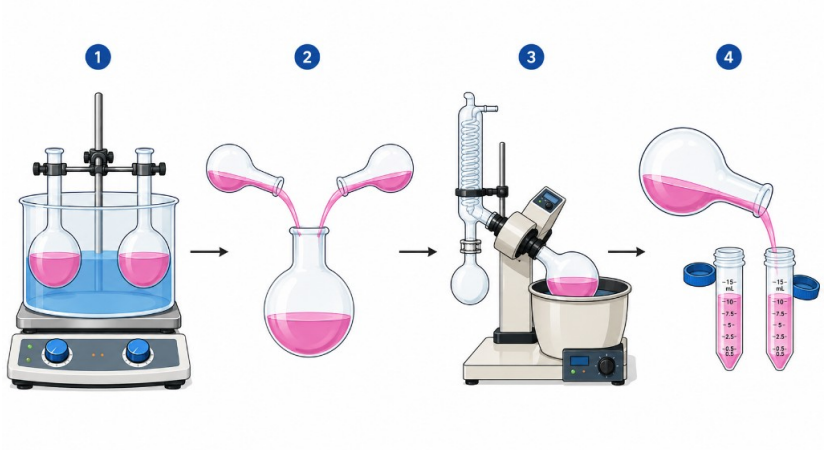

Figure 2.2: Schematic of the upscaled NaC–PERFECTA@PLGA–Rhodamine-B formulation workflow. **(1)** Two round bottom flasks are processed in parallel on a magnetic stirrer in a water bath. **(2)** The contents are pooled into a single flask. **(3)** Residual organic solvent is removed by rotary evaporation. **(4)** The suspension is divided into 15 mL centrifuge tubes prior to the washing step.

2.4 Physicochemical Characterization

Following preparation, nanoparticles intended for *in vitro* studies were characterized for hydrodynamic size and polydispersity (polydispersity index, PdI) by dynamic light scattering (DLS) and nanoparticle tracking analysis (NTA), while PERFECTA encapsulation efficiency is quantified by ^{19}F-NMR spectroscopy. Before the *in vitro* experiments, nanoparticles were sterilized by UV-light of the biological safety cabinet for 30 minutes.

2.4.1 Dynamic Light Scattering (DLS)

Dynamic Light Scattering (DLS), also referred to as Photon Correlation Spectroscopy (PCS), is a non destructive technique that measures the Brownian motion of colloidal particles in suspension and relates it to their hydrodynamic size and polydispersity [71, 72, 73]. Prior to analysis, nanoparticle suspensions were diluted 1:100 in ultrapure water and then loaded into a cuvette.

Physical principles. A coherent laser beam illuminates the sample and a detector records the intensity of light scattered at a fixed angle θ (Figure 2.3). The incident radiation is modelled as a plane electromagnetic wave,

$$\vec{E}_i(\vec{r},t) = \vec{E}_0\, \mathrm{e}^{\mathrm{i}(\vec{k}_i\cdot\vec{r}-\omega t)}, \tag{2.1}$$

where $\vec{E}_0$ is the electric field amplitude, $\vec{k}_i$ is the wave vector of the incident light having magnitude $k_i = 2\pi * n/\lambda_i$ where λ_i is the vacuum wavelength of incident light, ω is the angular frequency and $\vec{r}$ is the position within the scattering volume.

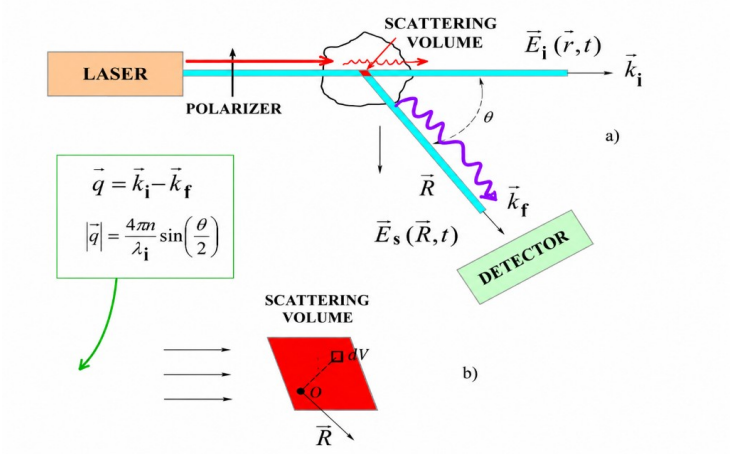

Figure 2.3: Schematic of a DLS experiment: (a) laser, polarizer, scattering volume, and detector at angle θ; (b) expanded view of the scattering volume. The scattering vector $\vec{q} = \vec{k}_i - \vec{k}_f$ and its magnitude $|\vec{q}| = (4\pi n/\lambda_i)\sin(\theta/2)$ will be used in the correlation function. Adapted from Prof. Francesco Cellesi, Lecture slides, Nanomedicine and Pharmaceutical Innovation, 2024.

When many particles scatter coherently within the illuminated volume, their partial waves interfere at the detector. Regions of constructive interference appear bright and regions of destructive interference appear dark, producing a granular *speckle* pattern (Figure 2.4). Because the particles undergo Brownian diffusion, their relative positions fluctuate in time and the speckle pattern evolves accordingly: smaller particles diffuse faster, so the speckle pattern changes more rapidly and the intensity autocorrelation decays on a shorter timescale; larger particles produce slower fluctuations [71, 73].

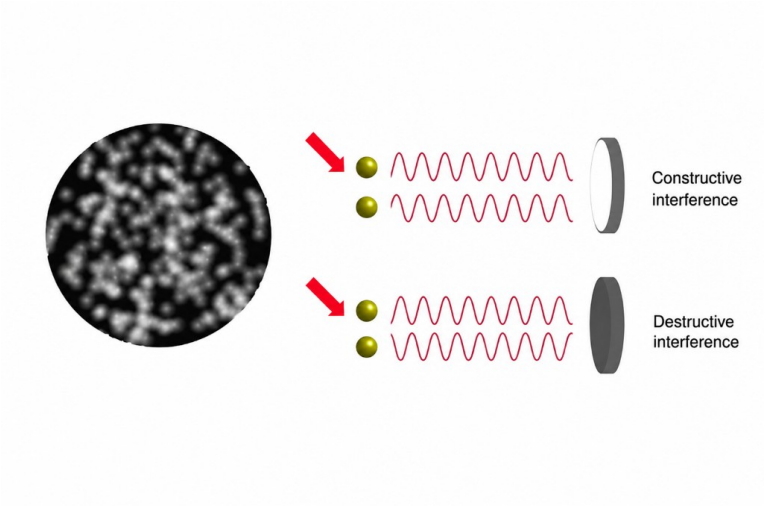

Figure 2.4: Speckle pattern formed by interference of light scattered from many particles (left). Constructive interference yields bright regions; destructive interference yields dark regions (right). Adapted from Prof. Francesco Cellesi, Lecture slides, Nanomedicine and Pharmaceutical Innovation, 2024.

For a large number of monodisperse particles in Brownian motion, the correlation function is an exponential decaying function of the correlation time delay. The normalized time correlation function of the scattered intensity is defined by

$$G^{(2)}(\vec{q},\tau) = \frac{\langle I_S(\vec{q},0)\, I_S(\vec{q},\tau)\rangle}{\langle I_S(\vec{q})\rangle^2}, \tag{2.2}$$

where $I_S(\vec{q},t)$ is the scattered intensity at wave vector $\vec{q}$, τ is the correlation time delay. For monodisperse nanoparticles undergoing translational Brownian diffusion, the correlation function can be fitted to a single exponential decay,

$$G^{(2)}(\tau) = B + A\,\exp(-2\Gamma\tau)\,, \tag{2.3}$$

where A is the baseline of the correlation function, B is intercept of the correlation function and Γ is linked to the translational diffusion coefficient D by

$$\Gamma = D\,|\vec{q}|^2. \tag{2.4}$$

The hydrodynamic diameter d_h is obtained from D through the Stokes–Einstein equa-

tion:

$$D = \frac{k_{\mathrm{B}} T}{3\pi\eta\, d_{\mathrm{h}}}, \tag{2.5}$$

where k_{B} is the Boltzmann constant. It is important to note that d_{h} is not necessarily identical to the geometric diameter measured by electron microscopy: it corresponds to the diameter of an equivalent hard sphere of solvent including the nanoparticle. Non-spherical nanoparticles are therefore described by an effective hydrodynamic diameter rather than a true geometric size [71, 72].

Figure 2.5 illustrates how different regions of the autocorrelation curve map to physical information. [73].

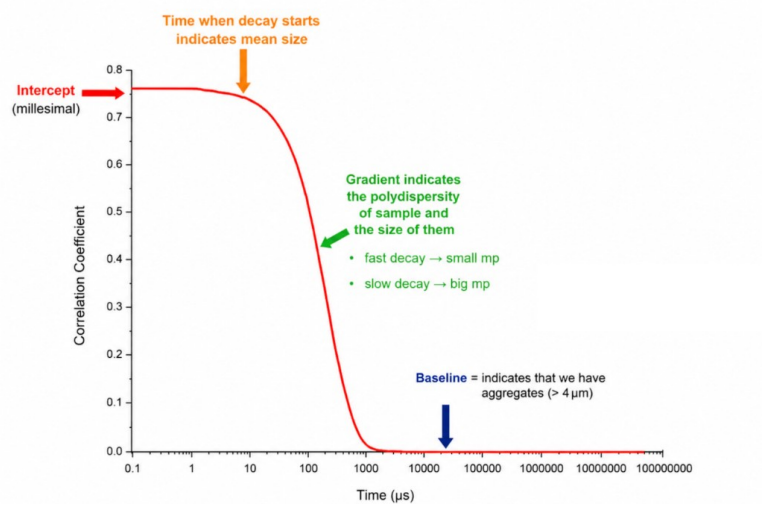

Figure 2.5: Correlation function in semi-log plot. The intercept (red) reflects signal quality; the onset of decay (orange) is related to the mean particle size; the gradient of the decay (green) reports polydispersity (fast decay → smaller particles; slow decay → larger particles); the baseline at long times (blue) should approach zero unless large aggregates are present. Adapted from Prof. Francesco Cellesi, Lecture slides, Nanomedicine and Pharmaceutical Innovation, 2024.

For a polydisperse suspension the autocorrelation function $G(\tau)$ is a sum of all exponential decay containing in the correlation function

$$G^{(\tau)} = A[1 + Bg^{(1)}(\tau)^2] \tag{2.6}$$

In the *cumulants* analysis, the exponential fitting expression is expanded as a power series in τ about the origin,

$$\ln[C(\tau)] = a + b\tau + c\tau^2, \tag{2.7}$$

where b is proportional to the z-average diffusion coefficient and the polydispersity index is defined as

$$\mathrm{PdI} = \frac{2c}{b^2}. \tag{2.8}$$

In practice, PdI values are interpreted as follows [73]: PdI $\approx$ 0–0.05 indicates a

highly monodisperse sample; 0.05–0.08 corresponds to a nearly monodisperse colloid; 0.08–0.7 is a moderate polydispersity; PdI > 0.7 signals a very broad or multimodal distribution.

For heterodisperse or multimodal systems that cannot be adequately described by cumulants, inverse Laplace transform algorithms such as CONTIN [74] or multi-exponential nonlinear least-squares fitting can recover the full distribution of decay rates $G(\Gamma)$.

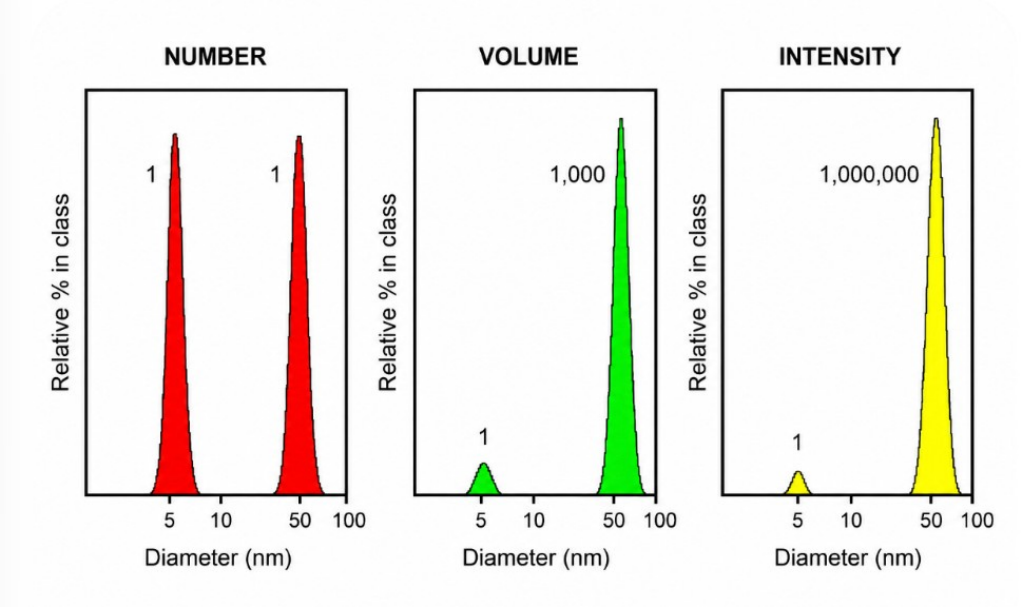

Figure 2.6: Illustrative bimodal mixture of 5 nm and 50 nm particles represented as number (left), volume (centre), and intensity (right) distributions. Equal numbers of both populations (1 : 1) yield equal number peaks; volume weighting emphasizes the larger population (1 : 1000); intensity weighting (1 : 10^6, Rayleigh d^6 scaling) is dominated by the 50 nm fraction, explaining why DLS is highly sensitive to traces of large aggregates.Adapted from Prof. Francesco Cellesi, Lecture slides, Nanomedicine and Pharmaceutical Innovation, 2024.

2.4.2 Nanoparticle Tracking Analysis (NTA)

Nanoparticle tracking analysis (NTA) is one of the few methods to visualize and measure nanoparticles in suspension in the range from 10-1000 nm, based on the analysis of Brownian motion. The size is the translational diffusion coefficient of the particles, which is related to the hydrodynamic diameter by the Stokes-Einstein equation 2.5, [75]. In this work, nanoparticle suspensions, after diluition 1:5000 in ultrapure water, were analyzed with a NanoSight instrument and NS Xplorer analysis software.

Physical principles. NTA is a fast single particle analysis tool to visualize and quantify size and concentrations of nanoparticles. NTA is based on the analysis of Brownian motion of the particles in suspension, through the observation of a video sequence of the particles in suspension. Particles are visualized by the illumination with a laser beam. The scattered light of the particles is recorded with a light sensitive

CCD or CMOS camera, which is arranged at a 90° angle to the irradiation plane. The 90° arrangement, also known as Ultra microscopy allows detection and tracking of the Brownian motion of 10 to 1000 nm sized vesicles.[75].

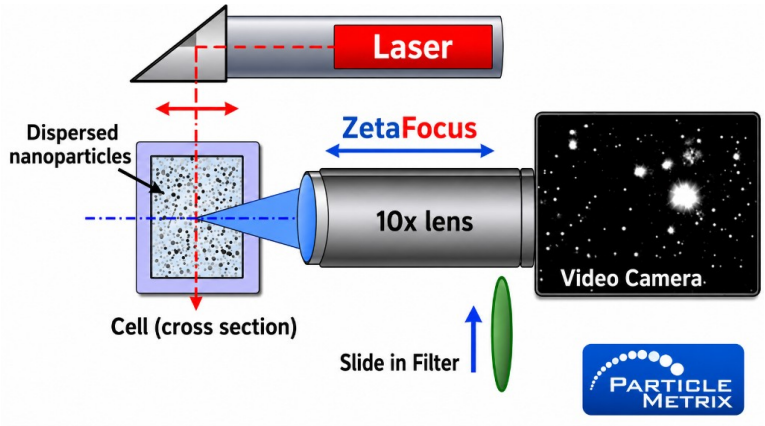

Figure 2.7: Schematic setup of a nanoparticle tracking analyzer. [75].

In the NS Xplorer software, particles are observed undergoing Brownian motion within the field of view; videos of typically 25–60 s duration are recorded while the software simultaneously identifies and tracks the centres of visible particles. For each trajectory, the mean displacement along the x and y axes in the observation plane is used to calculate the mean squared displacement (MSD), which is subsequently converted into a hydrodynamic diameter (d_{h}) through the Stokes–Einstein relation (Eq. 2.5) [76, 77]. Accurate sizing requires that each particle be followed through a sufficient number of Brownian steps to estimate reliably the mean step length. Small particles, however, are limited both by their short time they remain in the field of view, which can artefactually broaden the size distribution. To compensate for such truncated trajectories, NS Xplorer apply a *finite track length adjustment* (FTLA) model based on two-dimensional Brownian-dynamics simulations [78]. FTLA corrects for broadening due to short tracks and recovers a distribution width appropriate for monodisperse samples or polydisperse systems with discrete, resolvable populations [77, 78].

The movement of the particles per time interval is recorded and quantified as the mean square displacement $\langle x^2 \rangle$. Depending on the number of dimensions (one, two or all three dimensions), the diffusion coefficient, can be calculated as follows:

$$D = \frac{\langle x^2 \rangle}{2t} \qquad D = \frac{\overline{\langle x, y \rangle^2}}{4t} \qquad D = \frac{\overline{\langle x, y, z \rangle^2}}{6t} \tag{2.9}$$

Via the Stokes-Einstein relationship the particle diameter d can be calculated as function of the diffusion coefficient D at a temperature T and a viscosity η of the liquid

$$D = \frac{4k_B T}{3\pi\eta d} \tag{2.10}$$

In NTA, the particle fluctuation of a single particle is registered in two dimensions. After combining the Stokes-Einstein relationship and the two dimensional mean square displacement, the equation can be solved for the particle diameter d with:

$$d = \frac{4k_BT}{3\pi\eta t} \cdot \frac{4t}{\overline{\langle x, y\rangle^2}} = \frac{16k_BT}{3\pi\eta\,\overline{\langle x, y\rangle^2}} \tag{2.11}$$

By simultaneously tracking several particles their diameters can be determined in parallel.

Prior to analysis, nanoparticle suspensions were diluted 1:5000 in ultrapure water. Measurements acquired determine the hydrodynamic size distribution and total particle concentration of each formulation. For each batch, at least three independent measurements were recorded.

2.4.3 NPs-Protein Corona (PC) Stability Assays by NTA

An experiment was performed to assess the stability of the protein corona formed on nanoparticles, by monitoring changes over time in nanoparticle hydrodynamic diameter as a function of protein adsorption. NPs were incubated in CAR-T culture medium (TCM) supplemented with fetal bovine serum (FBS), at different time points (5 min, 1 h, 6 h and 24 h).

Conditioned medium was prepared before the assay by incubating 3.33×10^6 CAR-T cells in their TCM culture medium at 1×10^6 cells/mL for 6 h. At the end of incubation, the entire culture volume was collected and subjected to a cell wash (centrifugation at 1500 rpm for 5 min). The resulting supernatants constituted the conditioned medium.

The formulation tested was NaC–PLGA@PERFECTA nanoparticles, with a stock concentration of 2.33×10^{20} ^{19}F/mL.

For incubation in CAR-T-conditioned TCM, nanoparticles were diluted to a final concentration of 3.13×10^{19} ^{19}F/mL (dilution factor 1.6), matching the required concentration used when nanoparticles are incubated directly with CAR-T cells in the labelling protocol.

After 6 hours of incubation, each sample was further diluted 1:5000 in DMEM without phenol red, to not interfere with the NTA laser and to avoid altering the stability of the protein corona on nanoparticles. The hydrodynamic diameter of nanoparticles was then measured by nanoparticle tracking analysis (NTA).

This assay was repeated under identical conditions to a previous experiment, in order to confirm the initial observations. Result are reported in the Chapter 3.

NPs-PC Stability Assays by NTA with NIH-3T3 cells . In parallel, the same protein corona stability assay was performed on NaC–PLGA@PERFECTA nanoparti-

cles, with identical composition, to optimize the NPs-PC Stability assay protocol.

Nanoparticles were incubated in culture medium conditioned by NIH3T3 cells, both with and without 10% FBS. The conditioned medium was obtained by seeding 3.64×10^5 cells/mL for 6 hours. After conditioning, cells were washed with centrifugation step and the supernatants constituted the conditioned culture medium.

Nanoparticles ($C_{\text{stock}} = 2.33 \times 10^{20}$ ^{19}F/mL) were diluted 1:7.5 for incubation, yielding a required concentration of 3.33×10^{19} ^{19}F/mL. This concentration matches the standard NPs-concentration used in fibroblast uptake experiments for loading of approximately 1×10^{14} ^{19}F atoms per cell.

Prior to NTA, samples incubated in conditioned medium were diluted 1:5000 either in mQw or in DMEM without phenol red.

2.4.4 Zeta Potential

Colloidal stability is a prerequisite for both the shelf-life of nanoparticle suspensions and their behaviour after administration. In buffer media, nanoparticles undergo continuous Brownian motion and collide; if attractive interactions dominate, aggregation can occur. Collisions can give rise to two aggregation modes: coagulation, in which particles stick together with forces strong enough to make redispersion difficult and flocculation, in which particles form loose, open structures that are typically reversible and temporary. Aggregates not only alter the effective surface area and physicochemical properties of the dispersion, but may also compromise injectability and biodistribution (e.g. vascular occlusion upon intravenous injection) [79, 80, 57]. For this reason, nanoparticles must be rendered *kinetically* stable by engineering a sufficiently high energy barrier against close approach, typically through electrostatic repulsion (surface charge) and steric stabilization (polymer coatings such as PVA or PEG) [79, 67].

The theoretical basis of colloidal stability is provided by DLVO theory (Derjaguin–Landau and Verwey–Overbeek), which describes the interaction between two bodies with $V(tot)$, which is the sum of the attractive potential $V(A)$, given by the van der Waals forces and repulsive contributions $V(R)$, given by the electrostatic potential.

$V(tot)$, as a function of interparticle distance d, exhibits a secondary minimum, where particles can flocculate: particles will stick with relatively weak binding energy but can be redispersed applying mechanical forces. Then V_{tot} rises to a maximum, V_{max}, which defines the energy barrier that particles must not overcome, if irreversible aggregation is to be avoided. If Brownian collisions supply sufficient energy to surmount V_{max}, the system can descend into the primary minimum, where van der Waals attraction dominates and irreversible coagulation occurs; in this regime, redispersion of the nanoparticles is essentially impossible. It is therefore essential to engineer nanoparticle formulations so as to maximize this barrier, preventing barrier crossing and preserving

colloidal stability. (Figure 2.8).

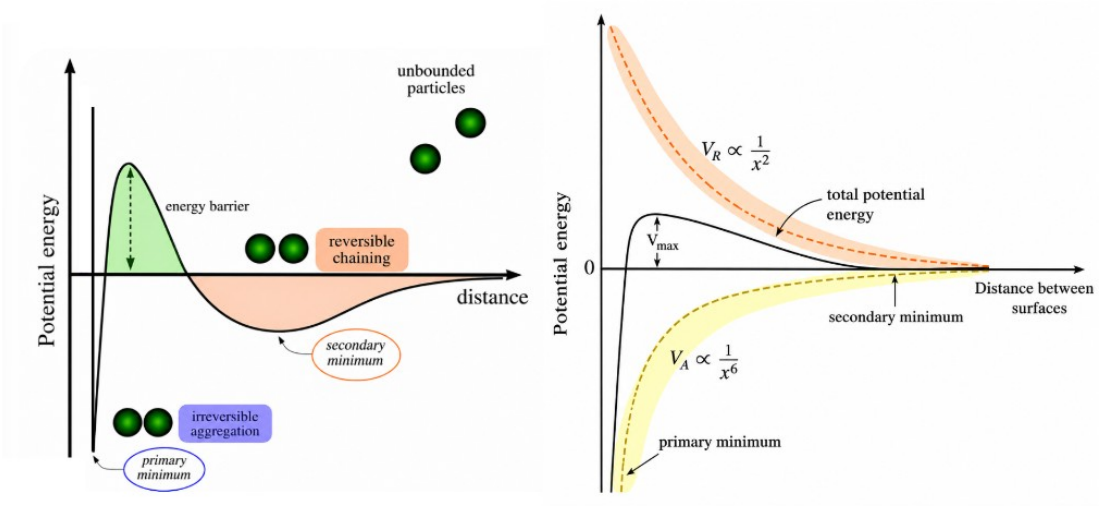

Figure 2.8: Schematic DLVO interaction potential between two colloidal particles as a function of distance. The repulsive branch V_R (electrostatic) and attractive branch V_A (van der Waals) combine into a total curve with a primary minimum (irreversible aggregation), an energy barrier $V_{\max}$, and a secondary minimum (reversible association). Adapted from DLVO theory [81, 82, 80, 79].

When a nanoparticle is immersed in electrolytes, dissociable surface groups (e.g. carboxylates on polyester matrices) establish a net surface charge balanced by ions in solution [83, 80, 84, 79]. Ions in the Stern layer are strongly adsorbed at the interface, whereas the diffuse layer contains more loosely associated ions. The *zeta potential* (ζ) is defined as the electrostatic potential at the *slipping plane* (plane of zero shear): the boundary within which the fluid moves with the same diffusion coefficient and the same Brownian motion of particles. It must be distinguished from the surface potential Ψ_0 at the particle interface and from the Stern-layer potential Ψ_d; neither Ψ_0 nor Ψ_d is directly accessible in routine measurements on nanoparticle suspensions, because the determined quantity reflects the *hydrodynamic* behaviour of the particle together with its associated solvent and ions bounded. For these reasons, only ζ can therefore be obtained experimentally and is used as a practical approximation for the effective surface charge that governs interparticle electrostatic repulsion in the DLVO framework [80, 84, 79].

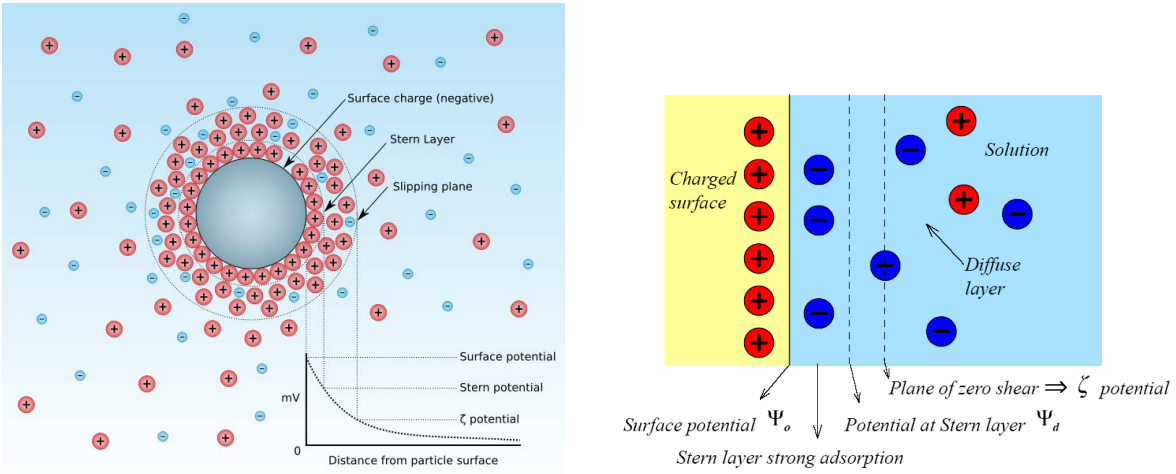

Figure 2.9: Electrical double layer around a negatively charged spherical particle: Stern layer, slipping plane, and decay of Ψ_0, Ψ_d, and ζ with distance. Reproduced from [80, 83, 84].

Guidelines relate $|\zeta|$ to colloidal behaviour as follows [84, 80, 79]: $|\zeta| < 5\,\text{mV}$, rapid coagulation or flocculation; $|\zeta|$ between 10 and 30 mV, incipient instability; $|\zeta|$ between 30 and 40 mV, moderate stability; $|\zeta|$ between 40 and 60 mV, good stability; $|\zeta| > 60\,\text{mV}$, excellent stability. The commonly adopted operational window for stable injectable dispersions is $|\zeta| > 30\,\text{mV}$, whereas values near zero favour aggregation [84, 79, 67].

Zeta potential is commonly determined by electrophoretic light scattering (ELS): an electric field is applied across the sample, which induces charged particles to move, and the electrophoretic mobility u_E of particles (i.e. the velocity of the particles in the electric field) is measured from their directed motion [80, 84, 79], under the following Henry equation,

$$u_\text{E} = \frac{2\varepsilon\,\zeta\,f(\kappa a)}{3\eta}, \tag{2.12}$$

where ε is the dielectric constant of the medium, η its viscosity, κ the Debye parameter, a the particle radius, and $f(\kappa a)$ Henry's function (equal to 1.5 in the Smoluchowski limit, in aqueous solution of moderate electrolyte concentration) [80, 84, 79].

In previous work, ζ potential measurements were performed with a Zetasizer Nano ZS (Malvern Instruments, UK), equipped with a 633 nm He–Ne laser, at a constant temperature of 25°C. Measurements were performed using folded capillary cells, which incorporate two gold-plated beryllium/copper electrodes to apply the electric field. Prior to measurement, the cells were carefully washed with mQw, and filled with the sample ensuring full immersion of the electrodes and absence of air bubbles. NPs were diluted 1:5 v/v in mQw, and each measurement was performed in triplicate to ensure reproducibility. [85].

These measurements confirmed adequate colloidal stability of the nanoparticle dispersions and enabled subsequent biological experiments on CAR-T cell labeling.

2.4.5 Quantitative ^{19}F-NMR

Nuclear magnetic resonance (NMR) spectroscopy exploits nuclei with non-zero nuclear spin ($I \neq 0$), such as ^{19}F ($I = 1/2$), placed in a strong, homogeneous static magnetic field $\mathbf{B}_0$ [48, 46]. Unlike ^{19}F-MRI, which encodes spatial information through magnetic field gradients, ^{19}F-NMR is an analytical technique: nuclear spins precess at the Larmor frequency $f_0 = \gamma B_0/(2\pi)$ (Eq. 1.1), are selectively excited by a radiofrequency pulse at f_0, and the resulting free induction decay (FID) is detected by a receiver coil and Fourier transformed into a one dimensional spectrum, in which the integrated intensity of each resonance is proportional to the number of chemically equivalent fluorine nuclei [48, 46, 50]. In this work, Quantitative ^{19}F-NMR was used to characterize the nanoparticle formulations by determining the encapsulation efficiency and total PERFECTA content before cell labeling. Following labeling, cell lysis and sample preparation, the method was also applied to quantify the cell-associated ^{19}F content and calculate the mean fluorine payload per cell; measurements were performed on a Bruker Avance III HD 400 spectrometer (9.4 T, ^{19}F observe frequency ≈ 376 MHz).

Quantitative ^{19}F-NMR for Determination of PERFECTA Encapsulation Efficiency in NP Formulations

400 μL aliquots of nanoparticle suspension were transferred into standard 5 mm NMR tubes together with a coaxial insert containing 100 μL of the external fluorine reference (TFA). Trifluoroacetic acid (TFA, CF_3COOH, $M_w = 114.02\,\mathrm{g\,mol^{-1}}$, three chemically equivalent ^{19}F nuclei per molecule, $\delta \approx -75.5$ ppm) was used to prepare the external standard solution containing 10^{20} ^{19}F nuclei in total, corresponding to a final concentration $C_f = 10^{21}\,\mathrm{F\,mL^{-1}}$. Neat TFA at room temperature provides a stock concentration $C_i \approx 2.35 \times 10^{22}\,\mathrm{F\,mL^{-1}}$. The volume of stock to be diluted in deuterium oxide (D_2O, 99.9% atom %D) was calculated from $V_{stock} = C_f V_f / C_i$, yielding approximately 4.3 μL of TFA per 100 μL final volume in (D_2O) The filled coaxial capillary was sealed before insertion into the main NMR tube, that contains the NPs solution. This configuration keeps the analytical sample separate from the reference, so that the nanoparticle suspension can be recovered after the measurement and used in the subsequent cell labelling step. The acquired ^{19}F-NMR spectra were processed and quantified with MestReNova software as described below.

Quantitative ^{19}F-NMR for NPs uptake quantification after cell labeling

Quantification of the intracellular ^{19}F payload after CAR-T labelling requires cell lysis, to obtain a homogeneous sample, thereby minimizing magnetic susceptibility variations and facilitating accurate shimming during ^{19}F-NMR analysis. Cells recovered after the labelling steps and ^{19}F-MRI were lysed in Triton™ X-100, non-ionic detergent buffer,

to release intracellular PERFECTA without chemical degradation of the fluorinated probe.

The working lysis buffer was prepared to reach a final Triton X-100 concentration of 2.5% (v/v) in PBS1X in the cell suspension. Depending on the volume of labelled cells available after labeling step, a more concentrated intermediate stock of Triton X-100 in PBS was prepared first (e.g. 10% or 27%, v/v), and only the volume required to achieve 2.5% in the final mixture was added. The volume of intermediate solution (V_1) was calculated from the dilution relationship $C_1V_1 = C_2V_f$, where C_1 is the Triton concentration in the intermediate, $C_2 = 2.5\%$ (v/v) is the target concentration, and V_f is the final volume of the lysis mixture (400 μL). The mixture was vortexed to ensure complete lysis, and the lysate was transferred into the outer compartment of the NMR tube. The inner coaxial capillary was loaded with 100 μL of the TFA reference solution prepared as described above, but the TFA reference concentration in ^{19}F per mL was adjusted based on the fluorine quantification obtained from ^{19}F-MRI imaging.

Spectra were imported into MestReNova and processed by applying baseline correction and manual phase correction to obtain a well resolved profile. The integrated areas under the PERFECTA resonance ($\delta \approx -72.5$ ppm) and the TFA external reference ($\delta \approx -75.5$ ppm) were then measured. Because the integrated intensity of each resonance is proportional to the number of chemically equivalent ^{19}F nuclei contributing to that signal, the fluorine content in the analytical sample was determined relative to the known TFA standard by area ratio analysis. Denoting by A_s and A_{ref} the integrated areas of the sample and TFA peaks, respectively, the area ratio was defined as

$$R = \frac{A_s}{A_{ref}}, \tag{2.13}$$

with the TFA reference peak taken as the unit reference ($A_{ref} \equiv 1$). The total number of ^{19}F nuclei in the sample compartment, N_F, was obtained by scaling this ratio by the total number of fluorine atoms present in the coaxial TFA reference, $N_{F,ref}$:

$$N_F = R \times N_{F,ref}. \tag{2.14}$$

For lysed CAR-T samples, the mean intracellular fluorine payload per cell was finally calculated by dividing N_F by the number of labelled cells counted before lysis, N_{cells}:

$$^{19}\text{F/cell} = \frac{N_F}{N_{cells}}. \tag{2.15}$$

The same MestReNova workflow (Eqs. 2.13–2.14) was applied to nanoparticle suspensions to quantify the total encapsulated PERFECTA content before cell labelling.

2.4.6 Raman Spectroscopy

Raman spectroscopy is a label-free, non destructive vibrational technique based on the inelastic scattering of monochromatic light by molecular bonds [86]. When a sample is illuminated by laser radiation of frequency ν_0, the majority of photons are elastically scattered (Rayleigh scattering), with the same energy and wave length of incident light, while approximately $\frac{1}{10}$ of photons undergo inelastic scattering, as a result of the interaction between the incident light and the vibrational modes of the chemical bonds, characteristic of the analyte molecule. Because each chemical bond has its own vibrational frequency, the scattered photons emerge at a characteristic frequency that identifies the specific bond present in the sample.

The physical principle is summarized in the Jablonski Energy Diagram of Figure 2.10. In Rayleigh scattering, the molecule returns to the same vibrational level E_0 and the scattered photon has energy $h\nu_0$. In Stokes Raman scattering, the molecule is left in an excited vibrational state $E_0 + h\nu_m$ and the Stokes photon emerges with reduced energy $h(\nu_0 - \nu_m)$. In the less probable anti-Stokes process, scattering starts from an already populated vibrational level and the emitted photon gains energy, $h(\nu_0 + \nu_m)$. The Raman shift $\tilde{\nu} = (\nu_0 - \nu_{\text{scattered}})/c$ (reported in cm^{-1}) equals the vibrational frequency ν_m of the bond involved and is characteristic of the molecular species, independent of the excitation wavelength. Each compound therefore possesses a vibrational "fingerprint" that enables molecules identification.

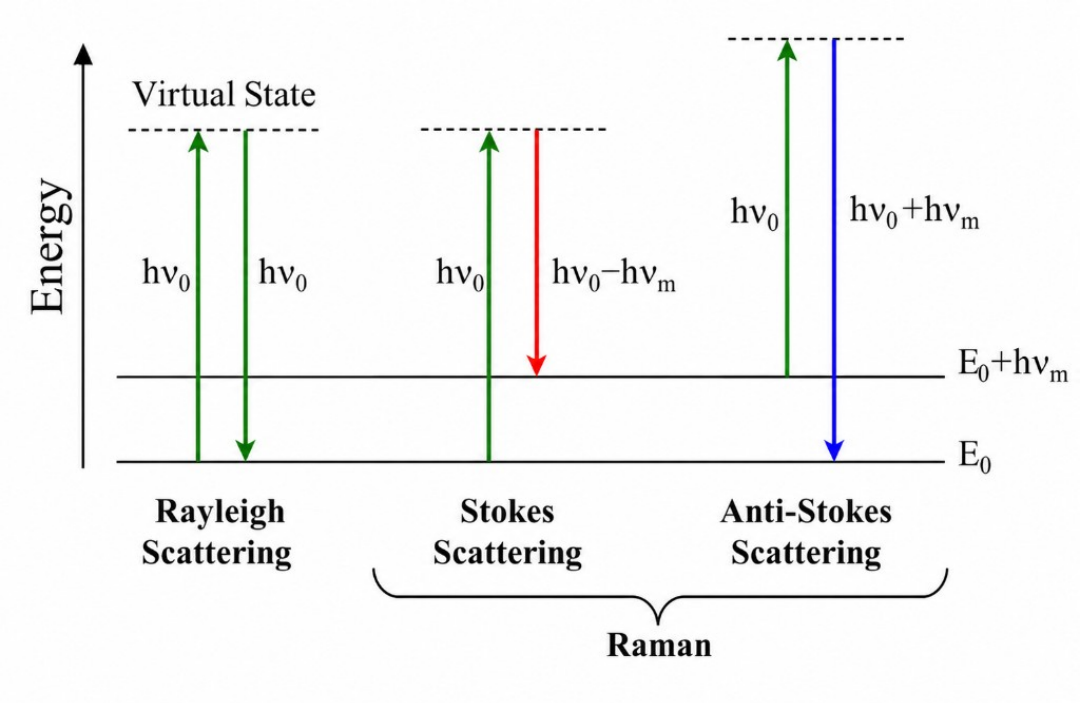

Figure 2.10: Jablonski Energy Diagram of Rayleigh, Stokes, and anti-Stokes Raman scattering (adapted from B&W Tek [86].)

In Raman microscopy, a tightly focused laser scans the sample and the Raman

spectrum is recorded at each pixel, building a hyperspectral map of chemical composition with lateral resolution typically between 250 nm and 1 μm, i.e. at micrometric and subcellular scale [63]. This spatial resolution is fundamentally different from that of ^{19}F-MRI, which encodes fluorine distribution over millimetre fields of view (1–2 mm in preclinical cell-tracking protocols) through nuclear spin precession in magnetic field gradients. The two modalities are **bimodal** and **multiscale** when applied to the same fluorinated reporter: PERFECTA can be detected by its single ^{19}F-NMR/^{19}F-MRI resonance ($\delta \approx -73.4$ ppm) and, independently, by its intense Raman band at $\sim$770 cm^{-1}, assigned to C–F stretching and bending modes of the symmetric perfluoro-*tert*-butyl groups (Figure 2.11) [63, 66]. Because mammalian cells and tissues lack endogenous Raman features in this spectral window, PERFECTA detection is **bioorthogonal**: the probe can be mapped inside cells without additional fluorescent or radioactive labels.

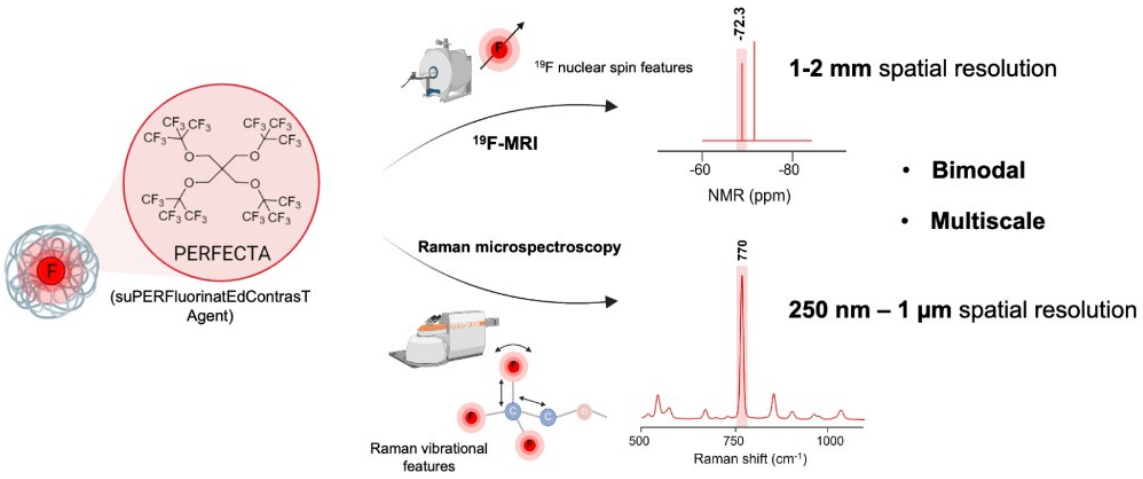

Figure 2.11: Complementary detection of PERFECTA by ^{19}F-MRI and Raman microscopy on the same contrast agent (concept adapted from Chirizzi *et al.* [63]). Together, the techniques provide a multiscale readout of nanoparticle uptake: ^{19}F-MRI quantifies the bulk fluorine payload in labelled cell populations, whereas Raman resolves whether PERFECTA remains encapsulated within NaC–PERFECTA@PLGA nanoparticles inside individual CAR-T cells and where the carrier is localized at subcellular level.

Raman spectroscopy is used for: (i) map where nanoparticles are located inside cells at micrometre scale, beyond the average fluorine content per cell; (ii) check whether PERFECTA remains inside NaC–PERFECTA@PLGA nanoparticles in labelled CAR-T cells, by matching the probe band at $\sim$770 cm^{-1} with PLGA Raman signals; (iii) at different time points after labelling, follow PLGA degradation and changes in PERFECTA signal over time. Measurements were carried out at the Department of Physics, Politecnico di Milano.

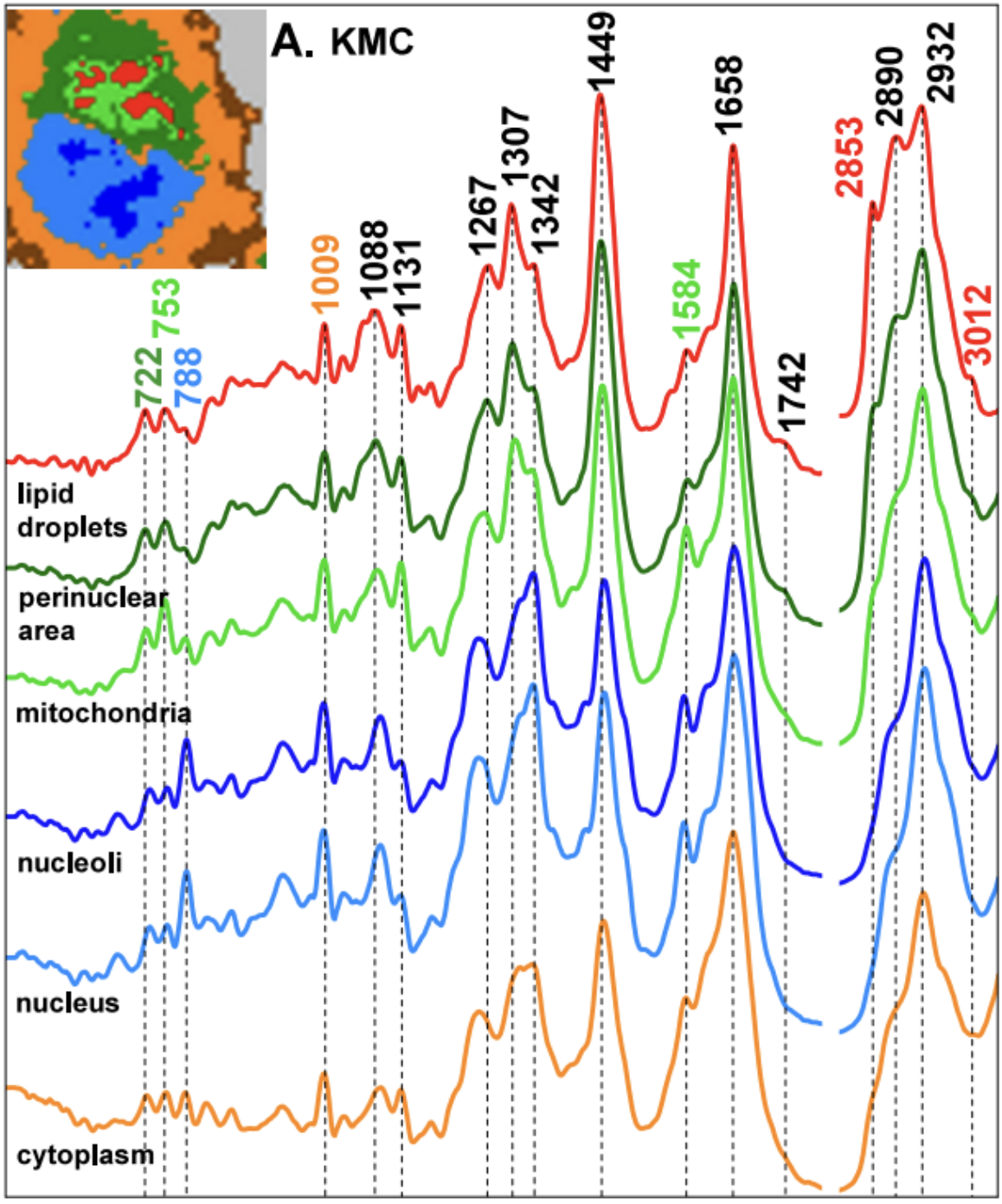

Figure 2.12: K-means clustering (KMC) of a hyperspectral Raman map of a living human aortic endothelial cell (HAEC): false-colour map of subcellular compartments and corresponding average Raman spectra in the fingerprint (∼600–1800 cm^{-1}) and high-wavenumber (∼2800–3100 cm^{-1}) regions for lipid droplets, perinuclear area, mitochondria, nucleoli, nucleus, and cytoplasm. Reproduced from Nowakowska *et al.* [87] (*The Raman Map of the Human Cell*, *Anal. Chem.* 2025, 97, 30, 16374–16382; DOI: `10.1021/acs.analchem.5c02035`; KMC map and compartment-averaged spectra as in Figure 2A and Supporting Information Figure S1). Without fluorescent labels, each pixel carries a full vibrational spectrum; KMC groups pixels with similar biochemical signatures and returns both a morphological map and compartment-specific mean spectra, whose peak pattern (e.g. lipid bands at 2853 and 3012 cm^{-1}, nucleic-acid features near 788 cm^{-1}, protein amide bands near 1658 cm^{-1}) acts as a molecular fingerprint of the underlying organelle. The same logic applies to labelled CAR-T cells in this thesis, where Raman is used to resolve whether PERFECTA and the PLGA carrier remain co-localized at subcellular scale.

Protocol Optimization for Raman Measurements

Raman microscopy requires single cells to remain adherent and optically accessible on a substrate that does not contribute intense background bands in the fingerprint region.

For this purpose, Petri dishes with quartz bottom have been employed. This type of Petri dish is Waken B Tech Co Japan Petri dish (35 mm as diameter) with quartz bottom (μ-Dish 12 mm), as shown in Figure 2.13.

Figure 2.13: Waken B Tech Co Japan Petri dish (35 mm as diameter) with quartz bottom (μ-Dish 12 mm).

Adhesion was promoted by coating the substrate with poly-D-lysine (PDL) approximately two hours before cell seeding. A stock solution (concentration $100\,\mu g\,mL^{-1}$), was UV-sterilized immediately before application. Under biological cabinet, a minimal volume of PDL solution (approximately 0.5 mL per dishes) was added to cover the entire substrate, incubated for 30 min at 37 °C, 5 % CO_2, and 95 % relative humidity (RH), aspirated, and followed by two to three rinses with sterile water. The slides were then left to air-dry for 30 min in the hood with caps open to complete the coating step before cell deposition.

CAR-T cells were seeded at 1×10^5 cells per dishes in a final volume of 1,2 mL of complete culture medium. To improve adhesion, the Petri dish was centrifuged at 200 g for 1 min with the brake off, rotated by 180°, and centrifuged again under the same conditions (Figure 2.14). Adhesion was verified after 24 hours with optical microscopy.

After 24 h, the medium was aspirated from each Petri dish and adhesion was confirmed by optical microscopy, retaining only samples in which cells were firmly attached to the quartz substrate. NaC–PERFECTA@PLGA nanoparticles were then applied at the Standard and Double ^{19}F/mL concentrations (as defined in Section 2.6.1) in a final volume of 150,μL of complete culture medium, directly onto the quartz surface and incubated for 6 h under the same culture conditions.

At the end of the incubation, samples were rinsed twice with PBS1X using gentle aspiration to avoid detaching adherent cells. Complete removal of free nanoparticles was verified by optical microscopy before proceeding to fixation. Cells were fixed by adding paraformaldehyde (PFA) 4% (v/v) and incubating for 20 min at room temper-

ature, to limit release of internalized nanoparticles before Raman acquisition. After fixation, the entire contents were aspirated, the substrate was washed with PBS1×, and samples were stored in PBS1× at 4,°C until Raman measurements.

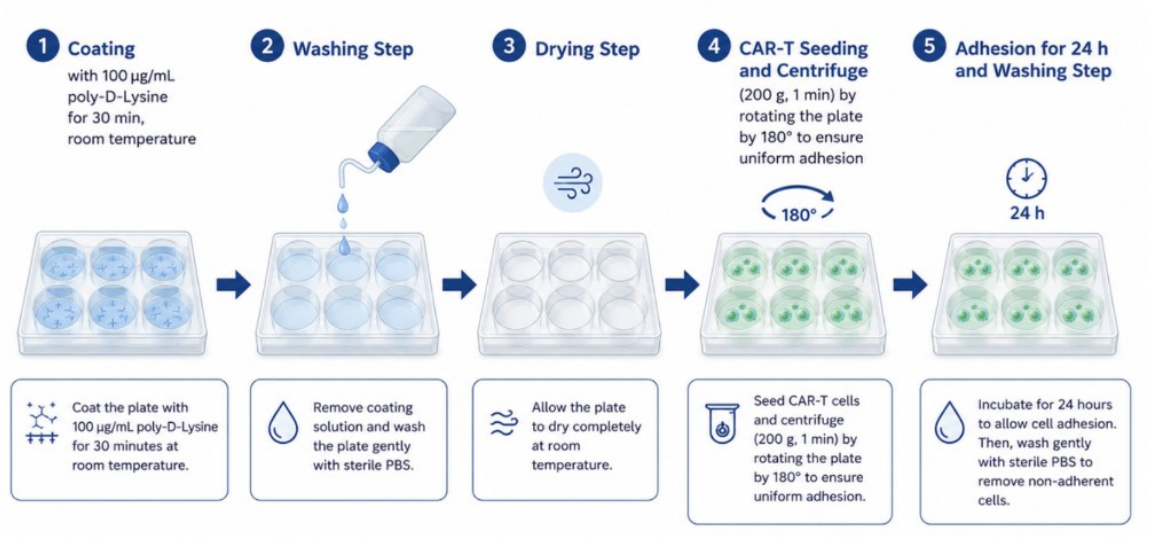

Figure 2.14: Workflow for CAR-T cell adhesion for Raman measurements.

Measurements were performed on a Raman microspectrometer at the Department of Physics, Politecnico di Milano. In order to do that, this home built experimental setup is composed by several main parts, which are fundamental for the recollection of the Raman signal. An image of the entire setup is reported in Figure 2.15.

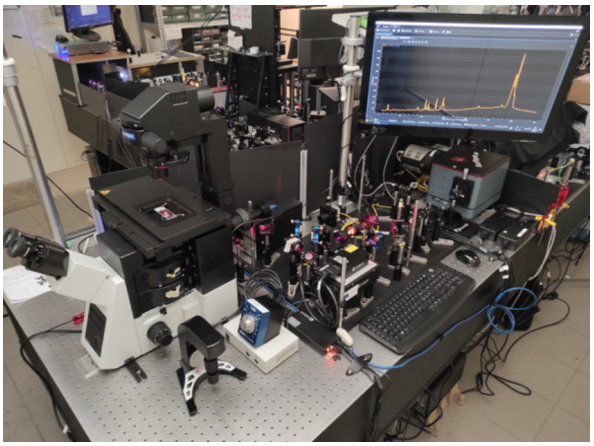

Figure 2.15: Home-built Raman microspectrometer: the setup is composed of microscope, laser, lens, filters and detectors for acquiring Raman signal.

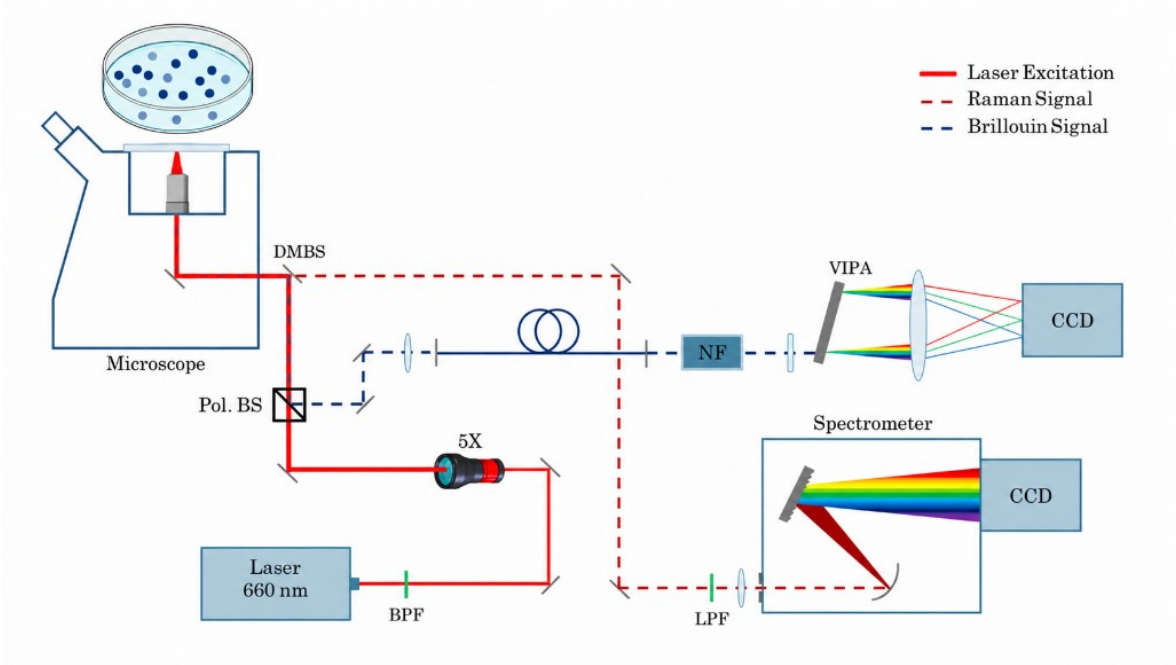

Figure 2.16: Experimental setup Raman and Brillouin signals: the five main components are present in the figure, the laser source, the microscope, the sample to be analyzed, the two spectrometers for recollecting the final signal, i.e. the VIPA for Brillouin analysis and the Princeton IsoPlane 160 spectrometer for Raman analysis. Adapted from Benedetta Gavazzoni, Master of Science Thesis.

For Raman acquisition, the optical path up to the sample includes five fundamental components: laser source, band-pass filter, telescope, dichroic mirror, and inverted microscope. After the light–sample interaction, in the Raman channel the backscattered signal passes again through the DMBS, is cleaned from the Rayleigh contribution by a long-pass filter, is focused by a lens, and is finally spectrally dispersed and detected by the CCD-based spectrometer.

Table 2.7: Main components of the Raman setup: specifications and function along the optical pathway.

Component	Main specifications	Function in the Raman setup
Laser source (Cobolt Flamenco)	Visible red, diode-based, continuous-wave laser; $\lambda = 660\,\text{nm}$; adjustable power 5–300 mW	Excites the sample and generates inelastic (Raman) scattering; it must be monochromatic and collimated. Power is optimized to avoid thermal damage/cellular alterations.
Band-pass filter (BPF)	Spectral selection around the useful laser line	Removes unwanted spectral components, improving incident beam purity and quality.
Optical telescope	5× magnification; spot expansion from ∼0.7 mm to ∼3.5 mm	Adjusts beam diameter/divergence for proper filling of the microscope optics and improved path alignment.
Dichroic Mirror Beam Splitter (DMBS)	Single-edge dichroic beam splitter; cut-off wavelength ∼660 nm	In excitation, it reflects radiation toward the sample; in collection, it transmits Raman-Stokes photons (>660 nm), separating them from the laser line.
Inverted microscope (Olympus) + objectives	Inverted configuration; objectives 5×, 20×, 50×, 60× WI; bright-field mode with white lamp	Focuses the laser on the sample and collects backscattered light; enables pre/post-acquisition imaging and live-cell analysis on quartz substrates under sterile conditions.
Long-pass edge filter (Raman)	Semrock RazorEdge LP02-664RU, 664 nm; edge steepness 3.3 nm; $T \approx 0\%$ at 660 nm, $T > 90\%$ above 670 nm	Suppresses residual Rayleigh signal and transmits the Raman-Stokes component to the spectrometer.
Spectrometer input lens	Collected-beam focusing optics	Concentrates the signal onto the diffraction grating, maximizing optical coupling and spectral throughput.
Raman spectrometer + detector	Princeton IsoPlane 160; 2D CCD camera (1024×256)	Disperses the signal by wavelength and records the Raman spectrum with spatial encoding on CCD pixels.

After each measurement, the acquired Raman datasets are post-processed (e.g., cosmic-ray removal, baseline correction, and intensity normalization) to reconstruct the Raman image and extract the corresponding Raman spectra.

2.4.7 ^{19}F-MRI

Cell samples labeled according to the established labeling protocol were visualized by ^{19}F-MRI, to verify the presence of nanoparticles inside the cells and enabling multimodal acquisition with the complementary Raman spectroscopic datasets.

Samples Preparation for ^{19}F-MRI Imaging

For ^{19}F-MRI analysis, both labeled-cell samples and NaF reference solutions were prepared following a standardized workflow.

Fixed cells obtained after cell labeling step with nanoparticles were resuspended to a final volume of 150 μL, in 0,2μL eppendorf. The suspension was centrifuged at 1500 rpm for 7 min, to obtained a compact pellet so that the cells were confined within

one, or at most two, ^{19}F-MRI slices. This maximized the fluorine signal in those slices, allowing subsequent analysis and quantification in these specific slices.

Reference standards were prepared by first estimating the expected fluorine content in the MRI slices from the average ^{19}F loading per cell and the total number of labeled cells obtained at the end of the labeling protocol, using the following equation:

$$^{19}F_{tot} = ^{19}F_{cell} \times N_{cells} \tag{2.16}$$

This provided an estimate of the expected fluorine concentration per mL in the sample region to be analyzed. Based on this estimate, sodium fluoride (NaF, $MM = 41.99\,\mathrm{g/mol}$) was dissolved in water to prepare reference solutions containing, in $50\,\mu$L, the same expected fluorine amount as the cellular sample.

Each reference tube contained $150\,\mu$L, corresponding to three $50\,\mu$L MRI slices at identical fluorine concentration. Therefore, each tube provided three internal slice equivalent measurements, enabling the ^{19}F signal from the cellular sample to be compared against three reference measurements (three technical replicates). To ensure robust quantification, reference concentrations were prepared to span a range $[\frac{1}{5}, 5]$ around the expected cellular fluorine content.

Subsequently, a 2% (w/v) agarose phantom was prepared to serve as a holder for Eppendorf tubes containing both cell samples and NaF references during MRI acquisition. The agarose matrix provides a homogeneous proton imaging background, minimizes magnetic susceptibility mismatch at tube interfaces, and stabilizes tube position throughout the scan. If the number of available samples is lower than the number of cavities in the phantom, the remaining cavities can be filled with Eppendorf tubes containing the same volume of water, in order to preserve geometric symmetry and reduce local field inhomogeneities and signal void artifacts.

Figure 2.17: Preparation of the agarose phantom insert used for MRI measurements. A polymeric negative mold was first produced by 3D printing. After cutting and immobilizing a 50 mL Falcon tube on the bench, a 2% (w/v) agarose solution was poured while keeping the negative mold fixed in position. The gel was allowed to set for approximately 2 h, then the mold was removed carefully to preserve cavity geometry. The resulting phantom insert was stored at 4°C and reused until noticeable shrinkage occurred due to water loss.

All experiments were performed on a 7 Tesla MRI scanner (Biospec; Bruker-Biospin, Ettlingen, Germany) using a dual-transmit receive $^{19}F/^{1}H$ volume coil (35×59 mm) for both proton and fluorine MRI acquisitions. ^{19}F-MR images were acquired at PERFECTA specific resonance frequency (-73.4 ppm). For all MRI acquisitions, a 3D turbo-spin echo sequence was used with the same field of view ($50 \times 28 \times 22$ mm) for ^{1}H-MRI (TR/TE = 250/15 msec, matrix = $128 \times 64 \times 8$, 6 averages) and for ^{19}F-MRI (TR/TE = 1600/5 msec, $64 \times 32 \times 8$, 80 averages).

^{19}F-MRI sensitivity experiments on CAR-T Labeled cells were performed and, after that, further checked through ^{19}F-NMR to confirm the fluorine content analyzed.

For each sample, the signal-to-noise ratio (SNR) was measured using the image analysis tools available in ParaVision 6.0 software (Bruker BioSpin). The total amount of ^{19}F atoms per cell was estimated from ^{19}F-MRI by signal-to-noise ratio (SNR) calibration against NaF reference tubes.

For each ROI, the SNR was computed as:

$$\mathrm{SNR} = \frac{S_{\mathrm{ROI}}}{\sigma_{\mathrm{noise}}} \tag{2.17}$$

where S_{ROI} is the mean ^{19}F signal measured within a region of interest drawn over each sample on the 19F image (ROI) and σ_{noise} is the average background noise measured in 3 noise regions outside the samples.

The ROI volume was calculated from ROI area and slice thickness:

$$V_{\mathrm{ROI}}(\mu\mathrm{L}) = A_{\mathrm{mm^2}} \times h \tag{2.18}$$

with $h = 2.7$ mm (slice thickness).

The total ^{19}F content in each reference ROI was calculated from the known reference concentration and ROI volume as:

$$^{19}F_{\mathrm{ROI,ref}} = \frac{C_{\mathrm{ref}} \times V_{\mathrm{ROI,ref}}(\mu\mathrm{L})}{1000} \tag{2.19}$$

where C_{ref} is the NaF reference concentration (^{19}F atoms mL^{-1}) and $V_{\mathrm{ROI,ref}}(\mu\mathrm{L})$ is the ROI volume of the reference tube.

Using the two NaF references, the fluorine content in each ROI was obtained by linear SNR scaling, using the following equations:

$$^{19}F_{\mathrm{ROI}} = {}^{19}F_{\mathrm{ROI,ref}} \times \frac{\mathrm{SNR}_{\mathrm{sample}}}{\mathrm{SNR}_{\mathrm{ref}}} \tag{2.20}$$

Finally, fluorine loading per cell was computed as:

$$^{19}F/\mathrm{cell} = \frac{^{19}F_{\mathrm{ROI}}}{N_{\mathrm{cells}}} \tag{2.21}$$

and the associated uncertainty was reported as the standard deviation between the two reference estimates. ($1–2 \times 10^{20}$ ^{19}F mL^{-1}.)

2.5 Biological Experiments

2.6 CAR-T cell culture

CAR-T cells employed in this study were generated by Dr Manuela Zingarelli in Prof. Serena Pellegatta's laboratory at the Fondazione IRCCS Istituto Neurologico Carlo Besta and kindly provided for the experimental activities conducted as part of this thesis. CAR-T cells must be cultured in their complete culture medium (TCM), consisting of 44% RPMI-1640 EUROCLONE, 44% Click's Medium, 1% P/S, 1% L-Glutamine v/v and 10% FBS-HyClone. Cells should be maintained at a density of 1×10^6 cells/mL, with a maximum of 3×10^7 cells per T25 flask.

CAR-T cells can be used either fresh (i.e., immediately after engineering) or after cryopreservation. Under standard conditions, cells are cryopreserved at day 7 of maturation in 90% FBS-Gibco and 10% DMSO (Dymethil Sulphoxide); therefore, after thawing, culture timing is resumed from day 7. Cells are preferentially used for labeling at day 10–13 of maturation.

In this work, it was chosen to use cryopreserved CAR-T cells.

Thawing and feeding of cryopreserved CAR-T cells: Cells were cryopreserved in cryovials in liquid nitrogen at approximately −196 °C, and are thawed 5 days before the labeling experiment. Upon thawing, the full volume of the cryovial was transferred and slowly dripped into a conical centrifuge tube (Falcon) containing FBS-Gibco, then-centrifuged at 1500 rpm for 5 min to remove dead cells, counted and resuspended at the standard density in TCM medium supplemented with Interleukins (ILs) at the following final concentrations in culture (Feeding Procedure):

- IL-7: 10 ng/mL (final dilution 1:10 000);
- IL-15: 5 ng/mL (final dilution 1:20 000).

Two days after thawing, a wash step is performed to remove dead cells: centrifugation at 1500 rpm for 5 min, removal of the supernatant containing non viable cells, resuspension in complete medium at 1×10^6 cells/mL, and subsequent feeding. Cell counts should be performed to monitor growth kinetics. Typically, the number of viable cells at thawing is approximately half of the number initially cryopreserved, whereas growth generally increases rapidly after the second feeding.

2.6.1 CAR-T labeling protocol

Human anti-B7H3 CAR-T cells were labelled *ex vivo* with NaC–PERFECTA@PLGA-Rhodamine B nanoparticles under sterile conditions at 37 °C, 5 % CO_2, and 95 % relative humidity, in T25 flask in 2–3 replicates for each conditions.

Two fluorine concentrations were used throughout this work, referred to as *Standard* and *Double* ^{19}F/mL:

- **Standard (1x):** $C_{\mathrm{f}} = 3.13 \times 10^{19}$ $^{19}\mathrm{F\,mL^{-1}}$;
- **Double (2x):** $C_{\mathrm{f}} = 6.26 \times 10^{19}$ $^{19}\mathrm{F\,mL^{-1}}$.

The standard concentration corresponds to that previously established and successfully used in PERFECTA@PLGA nanoparticle uptake experiments involving both immune and adherent cells.
For each batch, the volume of nanoparticle stock (C_{i}) to be added per flask was calculated from the dilution factor

$$\mathrm{FD} = \frac{C_{\mathrm{i}}}{C_{\mathrm{f}}}, \tag{2.22}$$

where C_{i} is the stock $^{19}\mathrm{F\,mL^{-1}}$ concentration of the nanoparticle suspension (the mean PERFECTA encapsulation efficiency across all nanoformulations was $\sim 1,92 \times 10^{20}$ $^{19}\mathrm{F\,mL^{-1}}$). The dilution factor (FD) of the nanoparticle stock suspension prepared for the protocol typically fell within the range [6–8]. The incubation times tested were 6 h (Standard) and overnight (∼18 h), to assess whether prolonged exposure increased nanoparticle uptake. Labelling was performed in T25 flasks at a final volume of 5 mL, containing CAR-T cells, nanoparticles at the target incubation concentration, and TCM without ILs.

Labelling procedure: CAR-T cells were recovered from T25 culture flasks, centrifuged at 1500 rpm for 5 min, resuspended in TCM without ILs, and counted. For each condition, 3.33×10^6 viable CAR-T cells were transferred to T25 Flask for labeling, together with the nanoparticle suspension (or an equivalent volume of sterile water for negative controls) and supplemented with TCM to $V_{\mathrm{f}} = 5\,\mathrm{mL}$.

Plates were incubated for the target time. At the end of incubation, the entire well content was collected by thorough pipetting, to separate cell clots and the flask was rinsed with an additional PBS1X. Each suspension was washed and resuspended in 1,6–2 mL of MACS® Staining Buffer and, then, counted. This cell count was performed *before* density gradient centrifugation to determine how many cells were present at the end of labeling (including any loss of viability during the labeling step) and to enable calculation of the recovery percentage in the subsequent purification step.

2.6.2 Optimization of Purification protocol of labeled cells

At the end of the *ex vivo* incubation with NaC–PERFECTA@PLGA nanoparticles, the cell suspension contains not only CAR-T cells with internalized fluorinated cargo, but also (i) nanoparticles remaining free in the medium and (ii) nanoparticles associated with the outer cell membrane, without true cytoplasmic internalization; these two fractions must be removed before reinfusion and ^{19}F-MRI readout. Because co-acquired anatomical ^{1}H-MRI cannot distinguish intracellular from extracellular fluorine, any residual free or surface-associated nanoparticles would contribute spurious signal in ^{19}F-MRI and bias quantitative estimates of labeled cell number and fluorine load *in vivo*. The purification step addressed in this subsection aims to isolate the population of truly labeled CAR-T cells while depleting non-internalized nanoparticles, so that the fluorine signal detected downstream reflects predominantly the intracellular ^{19}F payload of viable effector cells.

This separation was implemented by density gradient centrifugation, exploiting the different densities of lymphocytes and of the colloidal nanoparticle suspension. Two commercial media were compared in the optimization: Ficoll-Paque™ and Percoll® (Table 2.5). Although both are widely used for cell isolation, they differ markedly in chemical composition and in the density range that can be achieved.

- **Ficoll-Paque™:** aqueous medium with a fixed density of 1.077 ± 0.001 g/mL (at 20 °C), formulated for the isolation of human peripheral blood mononuclear cells (PBMCs) [88, 89]. It consists of Ficoll PM400, a highly branched, synthetic polymer of sucrose and epichlorohydrin ($M_r \approx 400\,000$ Da), combined with sodium diatrizoate. [89]. The polysaccharide component promotes aggregations of erythrocytes and facilitates depletion of granulocytes, whereas the iodinated salt sets the gradient density at which mononuclear cells band during centrifugation [88, 89].

- **Percoll®:** colloidal suspension of silica particles (∼15–30 nm) coated with a layer of polyvinylpyrrolidone (PVP), which stabilizes the particles in aqueous medium [90, 91]. Unlike Ficoll-Paque, Percoll is supplied at high density ($\rho \approx 1.135$ g/mL) and can be diluted with PBS to prepare iso-osmotic gradients, allowing the separation conditions to be tuned to the buoyant density of the cell type and of the particulate fraction to be removed [90, 91].

In the present work, both media were evaluated to identify which gradient best separates CAR-T cells from free and non-internalized NaC–PERFECTA@PLGA nanoparticles while preserving viability and recovery yield.

Density gradient centrifugation procedure with Ficoll-Paque and PBS1X: After the post-labelling cell count, each labelled CAR-T suspension was resuspended

in PBS1X to a final volume of $V_{\text{sample}} = 4\,\text{mL}$. For each replicate, Ficoll-Paque™ was dispensed into a 15 mL conical centrifuge tube (Falcon) at a volume determined by the sample:gradient ratio of 1:1.5 (v/v):

$$V_{\text{Ficoll}} = \frac{V_{\text{sample}}}{1.5}, \tag{2.23}$$

i.e. 2.67 mL of Ficoll-Paque for a 4 mL cell suspension. The cell suspension was then layered slowly onto the Ficoll cushion by inclining the tube and pipetting along the inner wall, so as to preserve a sharp density discontinuity.

Tubes were centrifuged at 2300 rpm for 20 min at room temperature, with the brake *off*. The cell ring, containing isolated CAR-T cells, was carefully recovered and transferred to a 1.5 mL microcentrifuge tube (Eppendorf). This fraction was centrifuged at 1800 rpm for 5 min with the brake *on*; the supernatant was collected and re-centrifuged under the same conditions to recover any cells remaining in suspension. The two resulting pellets were combined and resuspended in PBS1X to a final volume of $V_{\text{f}} = 300\,\mu\text{L}$. A post-Ficoll cell count was then performed on this suspension to quantify recovery percentage and viability after density gradient purification, relative to the pre-gradient count described in Section 2.6.1. Cell recovery after Ficoll-Paque purification was calculated as

$$\text{Recovery (\%)} = \frac{N_{\text{post-centrifugation}}}{N_{\text{pre-centrifugation}}} \times 100, \tag{2.24}$$

where $N_{\text{pre-centrifugation}}$ and $N_{\text{post-centrifugation}}$ denote the total number of viable CAR-T cells determined by trypan blue exclusion immediately before and after density gradient centrifugation, respectively.

Density gradient centrifugation procedure with Ficoll-Paque and Staining Buffer: The density gradient protocol described above was repeated under identical conditions:Ficoll ratio of 1:1.5 (v/v) (Equation 2.23), $V_{\text{sample}} = 4\,\text{mL}$, centrifugation at 2300 rpm for 20 min (brake off) and 1800 rpm for 5 min (brake on), final resuspension to $V_{\text{f}} = 300\,\mu\text{L}$, and recovery calculated according to Equation 2.24, but with a single modification: PBS1X was replaced throughout by MACS® Staining Buffer (Table 2.5). Labelled CAR-T cells were therefore resuspended in Staining Buffer before layering onto Ficoll-Paque, and the combined pellets were recovered in the same medium.

This variant was introduced to improve post-gradient cell recovery and to strengthen removal of free and peripherally associated NaC–PERFECTA@PLGA nanoparticles prior to ^{19}F-MRI imaging. Unlike PBS alone, Staining Buffer provides a protein and saline wash environment that more effectively isolated non-internalized nanoparticle fractions while preserving viable lymphocytes. **Bovine serum albumin (BSA)** saturates cell-surface binding sites and competes with opsonins and protein corona on NPs for adsorption onto the plasma membrane, thereby favouring detachment of nanopar-

ticles.

Ethylenediaminetetraacetic acid (EDTA), present in the Staining Buffer formulation, acts as a divalent cation chelator: by sequestering Ca^{2+} and Mg^{2+}, it disrupts short-range electrostatic bridges (e.g. calcium-mediated adhesion) between negatively charged nanoparticles and the cell surface, reduces cell– NPs aggregation during washing, and promotes release of peripherally bound nanoparticles into the supernatant, where they can be separated from CAR-T cells by the Ficoll density gradient. Together, these effects aim to maximize cell recovery percentage after density gradient centrifugation step and to minimize extracellular ^{19}F background that would otherwise confound quantitative MRI readout.

Density gradient centrifugation procedure with Percoll and Staining Buffer: Percoll® density gradients were prepared from Percoll stock. Two gradient formats were tested in parallel: a **multigradient** (four discrete layers 100%/80%/40%/30%) and a simplified **70%/30%** discontinuous gradient. In both cases, labelled cells were handled in MACS® Staining Buffer (Table 2.5) rather than PBS1X, following the rationale described for Ficoll-Paque purification.

Iso-osmotic Percoll (100%) was prepared by mixing Percoll® stock with PBS 10× in a 9:1 ratio (v/v). Working layers at different concentrations were obtained by diluting Percoll 100% with PBS1X. The two gradient formats tested are summarized in Table 2.8; in both cases, layers were sequentially underlaid in a 15 mL Falcon tube without disturbing the interfaces, and $V_{\text{sample}} = 2\,\text{mL}$ of labelled CAR-T suspension in Staining Buffer was layered slowly on top of the upper Percoll phase.

Table 2.8: Percoll density gradient formats tested for CAR-T/NPs separation.

Gradient type	**Preparation** (layers underlaid bottom → top)	**Cell collection**
Multigradient (100/80/40/30)	(i) 1 mL 100% iso-osmotic Percoll; (ii) 2 mL 80% (1.6 mL 100% Percoll + 0.4 mL PBS1X); (iii) 3 mL 40% (1.2 mL 100% Percoll + 1.8 mL PBS1X); (iv) 2 mL 30% (0.6 mL 100% Percoll + 1.4 mL PBS1X); then $V_{\text{sample}} = 2\,\text{mL}$ CAR-T in Staining Buffer on top	Cell ring at 30/40% interface
70/30 discontinuous	(i) 5 mL 70% (3.5 mL 100% Percoll+ 1.5 mL PBS1X); (ii) 5 mL 30% (1.5 mL 100% Percoll + 3.5 mL PBS1X); then $V_{\text{sample}} = 2\,\text{mL}$ CAR-T in Staining Buffer on top	Cell ring at 70/30% interface

For both gradient types, the entire labelling culture was collected from the T25 flask into a Falcon tube, following by a washing step of the flask, and centrifuged at 1500 rpm for 5 min. The supernatant was removed and the pellet was resuspended in Staining Buffer to $V_{\text{sample}} = 2\,\text{mL}$. A pre-Percoll viable cell count was performed (trypan blue exclusion). The cell suspension was layered onto the prepared Percoll gradient and centrifuged at $400\,g$ (rcf) for 10 min at room temperature, with the brake *off*. The cell ring at the target interface was carefully recovered and transferred to a

new Falcon tube; a pre-wash cell count was recorded on this fraction. To reduce Percoll viscosity before pelleting, the collected ring was diluted 10-fold with Staining Buffer (nine volumes of buffer per one volume of recovered interface). The diluted suspension was centrifuged at 1800 rpm for 8 min with the brake *on*; the supernatant was discarded and the pellet was resuspended in Staining Buffer to a final volume of $V_{\mathrm{f}} = 200\,\mu\mathrm{L}$ in a 1.5 mL microcentrifuge tube (Eppendorf). A post-Percoll count was performed on a 1:5 dilution (Bürker chamber). Recovery was calculated as in Equation 2.24, with $N_{\mathrm{pre-centrifugation}}$ and $N_{\mathrm{post-centrifugation}}$ referring to the pre- and post-Percoll viable cell counts, respectively.

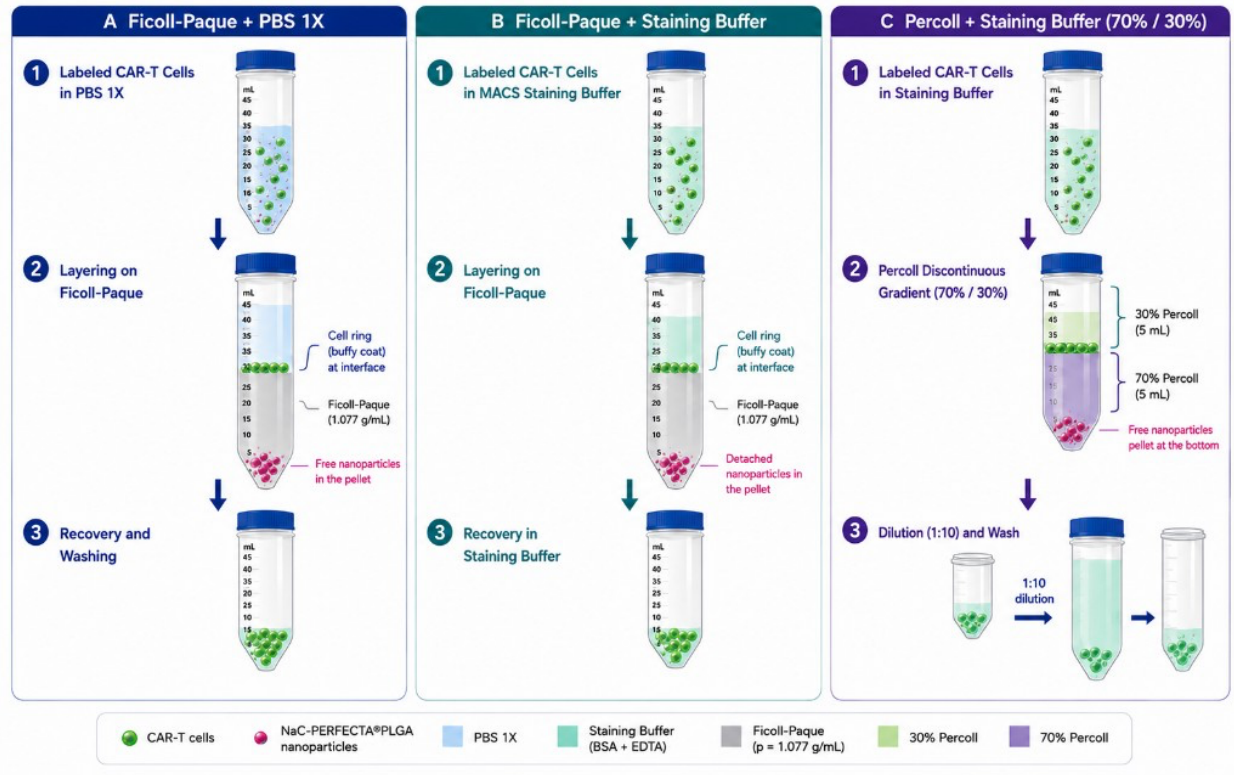

Figure 2.18: Optimization of the purification process of labeled CAR-T cells from free nanoparticles.

2.6.3 Flow cytometry for viability and uptake

Flow cytometry (FCM) is a technique for measuring dispersed cells carried in a liquid stream, enabling the simultaneous, multiparametric evaluation of individual cells that have been detached from their culture environment and, when required, labelled with fluorescent markers. Each cell passing through the instrument is recorded as a separate *event*, and up to $\sim 10^4$ events s^{-1} can be analysed; the measurable particle size range spans approximately 0.2–150 µm. FCM is primarily an *analytical* technique: cells are interrogated one by one to extract information, but the analysed cells are discarded and cannot be recovered unless the instrument is equipped with a fluorescence-activated cell sorter (FACS).

The cell suspension is aspirated from a sample tube and delivered to a coaxial flow chamber consisting of two concentric streams. In the inner channel flows the sample containing dispersed cells; in the outer channel, a sheath fluid moves at higher velocity, generating a traction force that prevents clogging and, through *hydrodynamic focusing*, aligns the cells in single file as they exit the nozzle and cross the laser beam. When incident light strikes a cell, part of the radiation is absorbed and part is transmitted or scattered. Light deviated at small forward angles (forward scatter, FSC; co-angular deviation 0–20°) is collected by a forward detector and is proportional to cell size. Light diffracted at ∼90° (side scatter, SSC) arises from internal refractive-index heterogeneities and reports on cytoplasmic granularity and structural complexity. Together, FSC and SSC provide label-free information on the cellular phenotype; for example, lymphocytes appear as a homogeneous cluster distinguishable from debris, erythrocytes, and granulocytes on an FSC/SSC plot, and allow unwanted events to be excluded before fluorescence-based quantification.

The measurement workflow is illustrated in Figure 2.19.

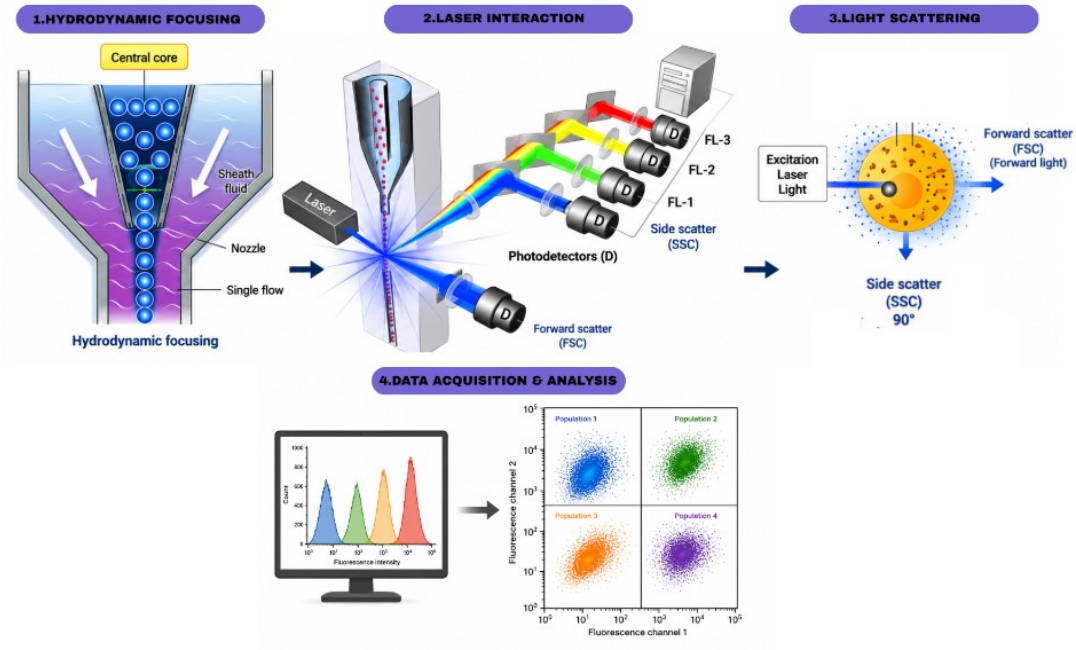

Figure 2.19: Flow cytometry workflow: (1)hydrodynamic focusing (sheath fluid, central core, single-file cells); (2)laser beam; (3)FSC, SSC, and fluorescence channels FL-1–3; (4)histogram and dot plot. Adapted from Prof. Gabriele Candiani lectures (2025).

Scatter alone cannot reveal the presence of specific surface markers or intracellular cargo. FCM therefore employs *fluorophores* (also called fluorochromes), molecules that absorb at one wavelength and, upon excitation, promote bound electrons from the ground state to an excited state; before returning to the ground state, part of the energy is dissipated as heat and the remainder is emitted radiatively as fluorescence at a longer wavelength, on a nanosecond timescale. Most benchtop cytometers are

equipped with a single excitation laser. Relatively few organic fluorophores absorb efficiently at one wavelength, which limits the number of spectrally separable probes available for direct excitation. To expand the usable emission palette, many commercial antibody conjugates employ FRET (fluorescence resonance energy transfer) dye pairs. These consist of a donor fluorophore and an acceptor fluorophore linked on the same macromolecule, typically within ∼10 nm of each other. Upon excitation of the donor at 488 nm, part of the energy is transferred non-radiatively to the acceptor, provided that the donor emission spectrum overlaps the acceptor absorption spectrum; the acceptor then emits at its own, longer wavelength. In this way, several probes can be resolved in distinct channels despite sharing the same excitation line. FRET efficiency depends on donor–acceptor distance, energy transfer, and dipole orientation, so the emitted colour may differ from that of the donor alone.

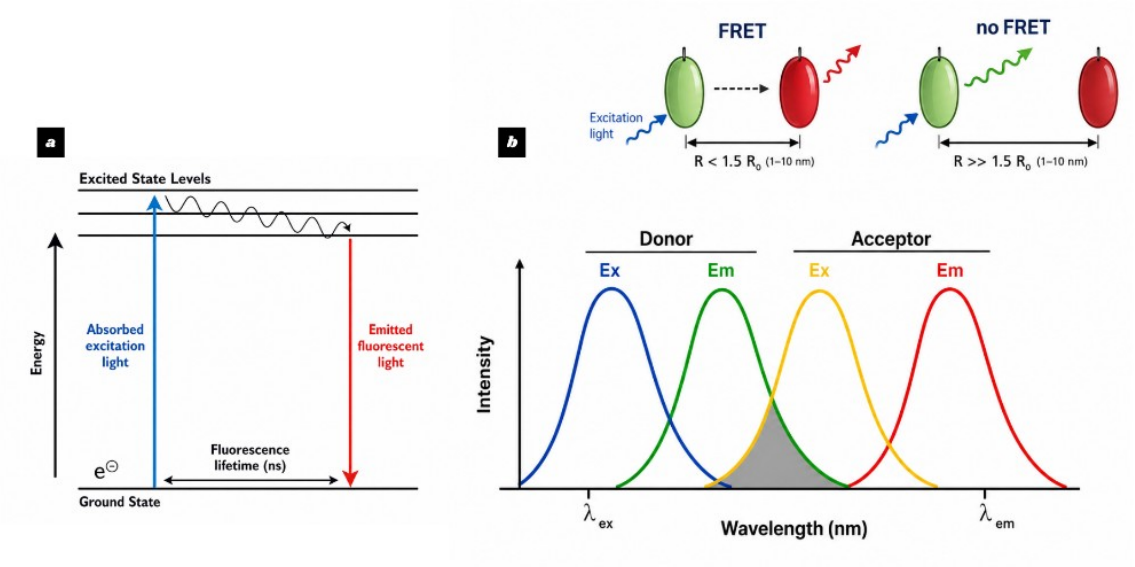

Figure 2.20: (a)Fluorescence Jablonski diagram: excitation, emission, nanosecond lifetime); (b)FRET (donor–acceptor energy transfer, distance dependence, spectral overlap). Adapted from Prof. Gabriele Candiani lectures (2025).

In flow cytometry, the fluorescent probe is typically conjugated to an antibody that recognizes a specific cluster-of-differentiation (CD) antigen on the cell surface, thereby enabling biochemical and biological measurements on individual events. Each CD marker can be tagged with a distinct fluorophore, so that the co-expression of up to four to six antigens can be assessed simultaneously on the same cell.

Fluorophore-conjugated antibodies can be used in two labelling strategies, classified according to how the antibody reagent is applied:

- **Direct labelling.** A primary antibody recognising the antigen of interest is directly conjugated to a fluorophore. Upon binding of the paratope to the epitope

on the target antigen, fluorescence emission from the attached fluorophore reports antigen presence on that cell. This approach is straightforward and minimizes the number of incubation steps.

- **Indirect labelling.** An unlabelled primary antibody binds the antigen of interest; a fluorophore-conjugated *secondary* antibody (anti-antibody) then binds the constant region of the primary immunoglobulin. Secondary antibodies are typically polyclonal and are raised by immunizing a second species with the constant domain of the primary antibody (cross-species immunization). Because several secondary molecules can bind one primary antibody, and each secondary can carry multiple fluorophores, the fluorescent signal is amplified, lowering the detection threshold and enabling visualization of low-abundance targets.

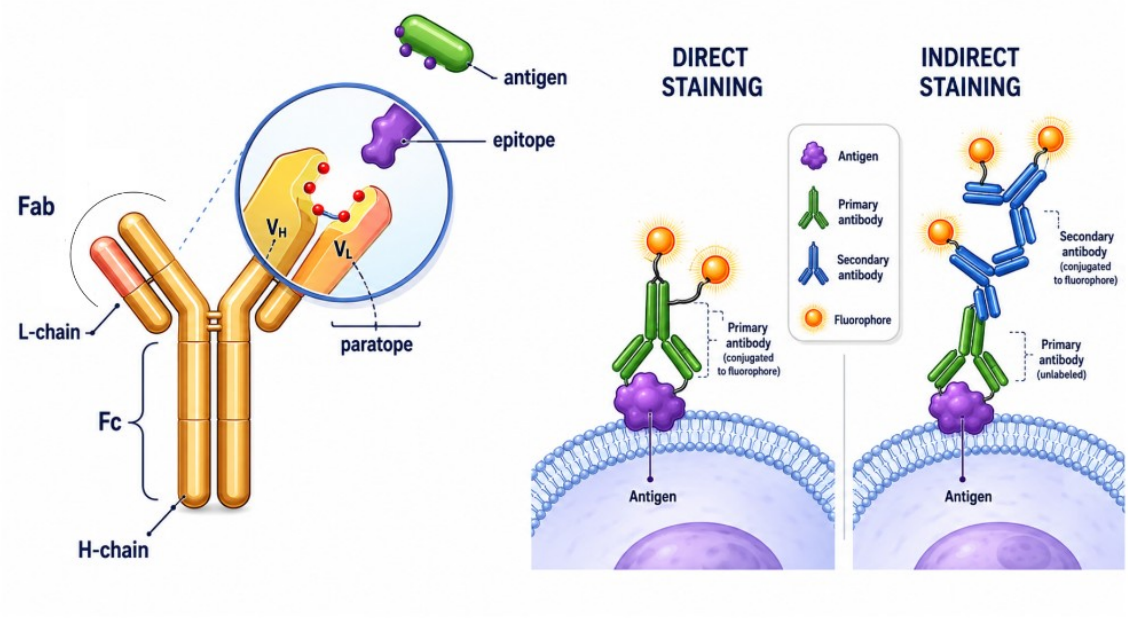

Figure 2.21: Antibody structure (Fab (fragment antibody binding domain), Fc (constant region), paratope–epitope binding) and direct vs. indirect immunofluorescence staining.Adapted from Prof. Gabriele Candiani lectures (2025).

Two-parameter dot plots (e.g. FSC versus SSC, or fluorescence versus scatter) display each event as a dot; homogeneous subpopulations are selected by drawing a *gate*, a delimiting region that excludes debris and aggregates. Within the gated population, the fraction of marker-positive cells is quantified by comparing fluorescence intensity against an unstained control sample, which defines the *background fluorescence* threshold above which events are scored as positive.

In this thesis, FCM was used to monitor the consequences of NaC–PERFECTA@PLGA-Rhodamine B labelling on CAR-T cell viability, cytotoxic function on glioblastoma target cells and to quantify nanoparticle uptake. Two conceptually different fluorescent reporters were employed: Viability™ 405/452 Fixable Dye, a membrane probe that labels cells with compromised plasma membranes (direct staining of non-viable cells) and Rhodamine B incorporated into the PLGA matrix during nanoparticle nanoformulation, which reports uptake because internalized carriers carry the fluorophore into the cytoplasm. Measurements were performed on a MACSQuant® Analyzer 16 equipped with a 488 nm laser and 579/34 nm filter for Rhodamine B detection in PE channel, and a 405 nm laser with a 450/50 nm VioBlue filter for Viability 405/452 detection.

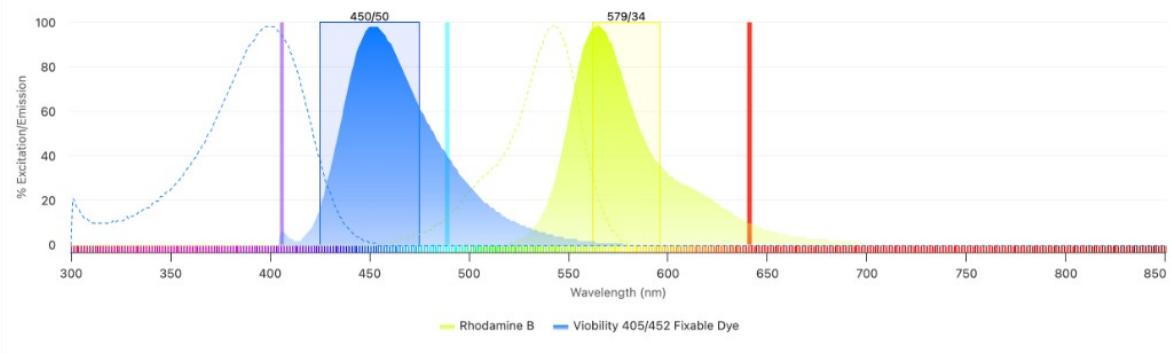

Figure 2.22: Emission spectra of Viability 405/452 Fixable Dye and Rhodamine B together with the detection windows of the MACSQuant® Analyzer 16. The fluorophores were selected to enable signal acquisition in the VioBlue (450/50 nm) and PE (579/34 nm) channels with minimal spectral overlap.

Viability Staining and Nanoparticle Uptake Detection: After density gradient purification (Section 2.6.2), 5×10^4 labelled CAR-T cells were transferred to 1.5 mL microcentrifuge tubes (Eppendorf) and resuspended in $V_f = 100\,\mu$L with PBS1X. Viobility staining was then performed by adding 1 μL Viability™ 405/452 Fixable Dye (stored at $-20\,^\circ$C) and incubating for 15 min at room temperature, protected from light. The reaction was ended by adding 1 mL MACS® Staining Buffer; samples were centrifuged at 1500 rpm for 5 min, the supernatant was discarded, and the pellet was resuspended in $V_f = 200\,\mu$L MACS® Staining Buffer before acquisition on the MACSQuant® Analyzer 16 (Section 2.6.3). For each sample, viability and uptake were quantified by gating lymphocyte on FSC/SSC and comparing fluorescence distributions against unstained controls processed in parallel.

2.6.4 Co-culture assay with glioblastoma neurospheres

To assess whether nanoparticle labelling alters CAR-T effector function against glioblastoma target cells, labelled and control CAR-T cells were co-cultured with adherent U-87 MG cells in 24-well plates. The assay was designed to compare four conditions in parallel: tumour cells alone (U-87 MG), U-87 MG co-cultured with non-transduced (NT) T activated cells, U-87 MG co-cultured with anti-B7-H3 CAR-T cells, and U-87 MG co-cultured with NaC–PERFECTA@PLGA-Rhodamine B-labelled CAR-T cells.

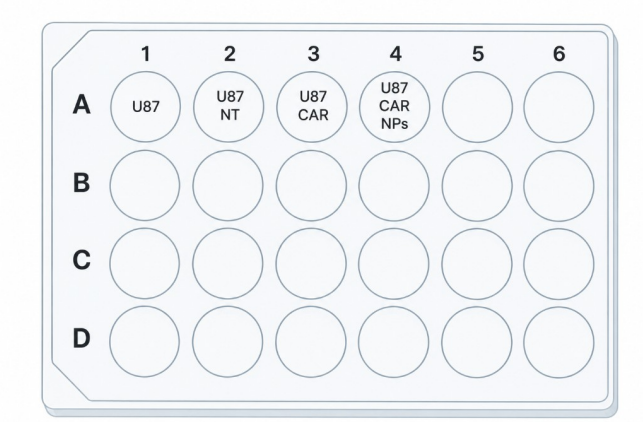

Figure 2.23: Layout of the 24-well plate used for the U-87 MG co-culture assay (row A, wells A1–A4). **A1:** U-87 MG alone (tumour cells control). **A2:** U-87 MG co-cultured with non-transduced (NT) T lymphocytes. **A3:** U-87 MG co-cultured with anti-B7-H3 CAR-T cells. **A4:** U-87 MG co-cultured with NaC–PERFECTA@PLGA-Rhodamine B-labelled CAR-T cells (NPs).

Because U-87 MG grows as adherent, tumour cells were seeded in advance (at least 4 hours above) so that they could adhere to the substrate before CAR-T cells were added. On the labeling experiment day morning, 1×10^5 U-87 MG cells were plated per well in $V = 1\,\mathrm{mL}$ TCM (without IL supplementation) and put to the incubator until the CAR-T fraction was ready.

The CAR-T cells used in this assay were those recovered immediately after the labelling and purification workflow described above (Section 2.6.2): labelled populations were collected from the Falcon tubes at the end of gradient purification (in MACS® Staining Buffer). From each labelled preparation, 5×10^4 cells were reserved for the post-labelling viability and uptake readout by flow cytometry (Section 2.6.3); the remaining cells were allocated to co-culture and to ^{19}F-MRI/^{19}F-NMR analyses. For co-culture, each well was brought to a final volume of $V_\mathrm{f} = 2\,\mathrm{mL}$ with a 1:1 effector-to-target ratio. For NT and CAR-T conditions, the number of effector cells plated was increased following the equation

$$N_\mathrm{effectorcells} = N_\mathrm{targetcells} \cdot \left(1 + \frac{100 - \eta_\mathrm{CAR-T}}{\eta_\mathrm{CAR-T}}\right), \tag{2.25}$$

where $\eta_\mathrm{CAR-T}$ is the CAR-T transduction efficiency (%). This correction compensates

for lymphocytes that did not undergo successful CAR transduction, so that the number of CAR-T effectors seeded per well remains comparable to the nominal 1×10^5 target used in the tumour control, rather than being underestimated by the non-transduced fraction. The remaining labeled CAR-T cells (at least 1×10^6) were processed according to the ^{19}F-MRI protocol.

Plates were incubated for 3 days under standard culture conditions (37 °C, 5% CO_2, 90% RH). At the end of the incubation, samples were collected and centrifuged at 1500 rpm for 5 min. For wells containing labelled CAR-T cells, the supernatant was retained to check, by flow cytometry, for nanoparticles released into the medium. Cell pellets were resuspended in $V_f = 100\,\mu$L PBS1X and counted.

For immunophenotypic analysis, cell viability was assessed first, following the Viability staining protocol described in Section 2.6.3. After the washing step, pellets were resuspended in $V = 50\,\mu$L of an antibody master mix prepared for each sample according to Table 2.9 (Figure 2.24).

Table 2.9: Composition of the 50 μL antibody master mix used to resospended the pellet for surface immunophenotyping of co-culture samples (one mix per sample). Reagents were combined in the order listed; detection channels refer to the MACSQuant® Analyzer 16 configuration (Section 2.6.3).

Reagent	**Target / role**	**Volume**	**Detection (MACSQuant® 16)**
PE-Vio® anti-human CD3	NT and CAR-T lymphocytes (CD3)	0.5 μL	Ex. 488 nm; Em. ∼615 nm; B3 (615/20 nm)
FITC anti-human B7-H3 (CD276)	Tumour antigen B7-H3	0.5 μL	Ex. 488 nm; Em. ∼519 nm; B1/FITC (525/50 nm)
APC anti-human CSPG4 (NG2)	Tumour antigen CSPG4	1.0 μL	Ex. 640 nm; Em. ∼660 nm; R1/APC (667/30 nm)
MACS® Staining Buffer	Diluent	48 μL	—
Total per sample			**50 μL**

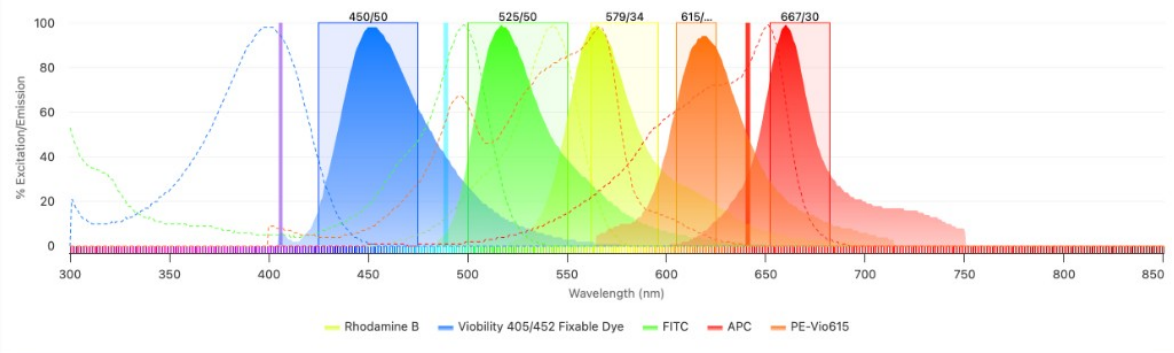

Figure 2.24: Excitation and emission spectra of the fluorophores employed in the co-culture immunophenotyping panel (Viability™ 405/452, FITC, Rhodamine B, PE-Vio® 615, and APC) together with the excitation laser lines and detection windows of the MACSQuant® Analyzer 16. Fluorophores were selected to enable signal acquisition in the VioBlue (450/50 nm), FITC (525/50 nm), PE (579/34 nm), B3 (615/20 nm), and APC (667/30 nm) channels with minimal spectral overlap.

Staining was carried out for 5 min at room temperature, protected from light. Each sample was then adjusted to $V_f = 200\,\mu$L with MACS® Staining Buffer and acquired on the MACSQuant® Analyzer 16. Gating on FSC/SSC and marker expression allowed the relative abundance of tumour and effector populations to be quantified and, in the labelled condition, the persistence of Rhodamine B signal during the time.

Chapter 3

Results and Discussion

3.1 Nanoparticles Formulation Scaling

As an initial step toward improving the scalability and translational potential of the nanoparticle platform, the first part of this thesis focused on the upscaling of the established formulation protocol. The aim was to increase nanoparticle batch yield while preserving the previously optimized emulsification workflow and avoiding major modifications to the preparation procedure.

Starting from the standard single-batch formulation described in Figure 2.1, which yielded 1 mL of final nanoparticle suspension, the production process was scaled up to obtain a four-fold larger final volume. As shown in Figure 2.2, this was achieved by processing two round-bottom flasks in parallel, each yielding 2 mL of final nanoparticle suspension, for a total production volume of 4 mL. For the NaC–PERFECTA@PLGA–Rhod-B formulations used in the *in vitro* experiments, the detailed preparation procedure is reported in (Section 2.3). Briefly, for each flask, the organic phase was prepared by dissolving PERFECTA, PLGA, and PLGA–Rhodamine-B in ethyl acetate, maintaining a final PLGA concentration of 20 mg/mL, a fluorescent polymer content of 2% w/w, and a PLGA/PERFECTA weight ratio of 1:1. The aqueous phase consisted of sodium cholate dissolved in mQ water. Emulsification, sonication, magnetic stirring were then performed according to the standard formulation protocol, while rotary evaporation was extended to ensure complete removal of the organic solvent from the larger volume. The washed nanoparticles were finally resuspended in mQw and characterized by dynamic light scattering (DLS).

Figure 3.1 shows the representative 90° measurement of correlation function in semi-log plot, normalized to the maximal intenisity value, indicating a homogeneous nanoparticle polydispersity (PDI <0.2) and the absence of aggregation (linear baseline). Moreover, the unweighted size distribution of the hydrodynamic radius shows a narrow peak at approximately 60 nm, confirming the homogeneous nature of the dispersion.

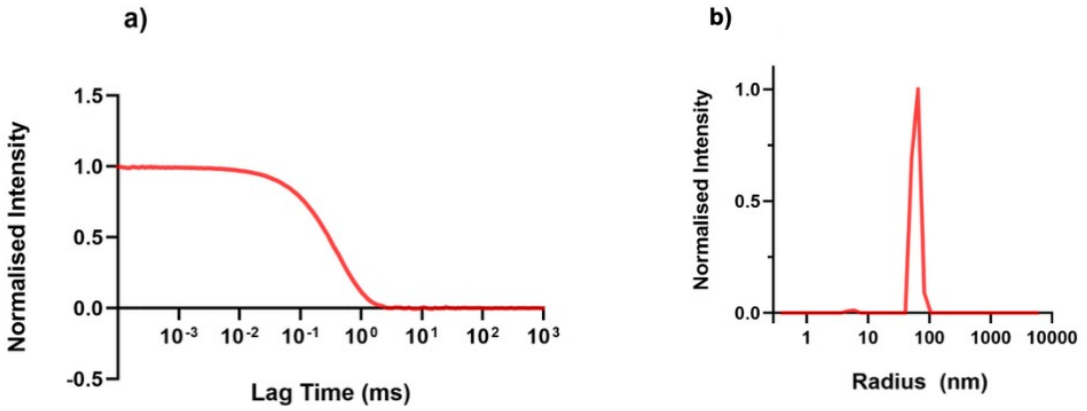

Figure 3.1: Representative DLS experiment's results: (a) autocorrelation functions in semi-log plot and (b) intensity-weighted size distribution of the NaC-PERFECTA@PLGA NPs upscaled formulation in aqueous solution measured at 90°

As shown in Figure 3.2, upscaling did not alter the hydrodynamic diameter (d_h) neither the polydispersity index (PDI) of NaC–PERFECTA@PLGA–Rhodamine-B nanoparticles. DLS measurements were performed on three independent upscaled batches and on the reference batch, acquiring data at four scattering angles (70°, 90°, 110°, and 130°). For each batch, d_h and PDI are reported as mean ± SD calculated on the four angular measurements. Across all formulations, d_h remained comparable between the 1 mL and upscaled NPs (approximately 124 nm), demonstrating the reproducibility of the upscaled protocol. In all cases, PDI values remained below 0.2, indicating a narrow, homogeneous size distribution and stable colloidal behaviour.

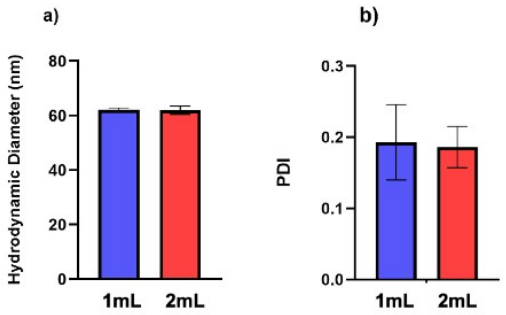

Formulation	Final volume	d_h (nm)	PDI
CCA31	2 mL	127 ± 3	0.190 ± 0.080
CCA32	2 mL	121 ± 3	0.180 ± 0.010
CCA33	2 mL	124 ± 3	0.190 ± 0.045
CCA118	1 mL	124 ± 1.38	0.190 ± 0.053

Figure 3.2: Effect of formulation upscaling on hydrodynamic diameter (d_h) and polydispersity index (PDI) of NaC–PERFECTA@PLGA–Rhodamine-B nanoparticles measured by DLS. **(a)** Mean ± SD of hydrodynamic diameter and **(b)** Mean ± SD of PDI of 1 mL (reference batch CCA118) and 2 mL upscaled batches (mean of three independent formulations: CCA31, CCA32, and CCA33). Comparable d_h (∼124 nm) and PDI values below 0.2 across all batches indicate that upscaling did not alter colloidal size, dispersity, or stability.

3.2 Nanoparticles Stability in Conditioned Media

The colloidal stability of NaC-PERFECTA@PLGA nanoparticles in biological media is a critical determinant of their behaviour during cell labelling, as rapid protein adsorption upon contact with serum supplemented culture medium leads to formation of a protein corona (PC) that can alter nanoparticle size, surface properties, and ultimately cellular uptake [70]. Building on the physicochemical characterization reported by Lobello [85], who monitored NaC-PERFECTA@PLGA nanoparticles in CAR-T-conditioned and unconditioned culture medium by dynamic light scattering (DLS), the present study aimed to confirm the temporal evolution of hydrodynamic diameter by nanoparticle tracking analysis (NTA). In that previous work, an increase in nanoparticle size was observed up to 6 h of incubation, followed by a return at 24 h to values comparable to those measured in water (CTRL sample), suggesting dynamic formation and subsequent reorganization of the protein corona without loss of colloidal integrity. In addition to confirm the previously observed results, we aimed to investigate whether the behavior described above was cell-type and/or culture-medium dependent, or whether it could be extended to other cellular models. For this reason, NIH-3T3 murine fibroblasts were introduced as an additional reference cell model, together with their corresponding culture medium, DMEM.

This confirmatory NPs–PC stability assay, described in Section 2.3.3, was therefore performed under identical incubation conditions, monitoring hydrodynamic diameter at 5 min, 1 h, 6 h, and 24 h after exposure of nanoparticles to CAR-T conditioned medium supplemented with serum.

On the basis of the parallel optimisation experiments with NIH-3T3-conditioned medium reported in the same section and shown in Figure 3.3, comparison of the two diluents applied before NTA measurements showed that dilution in phenol red-free DMEM better preserved protein corona stability by limiting osmotic shock, that could destabilize proteins adsorbed on the NPs surface.

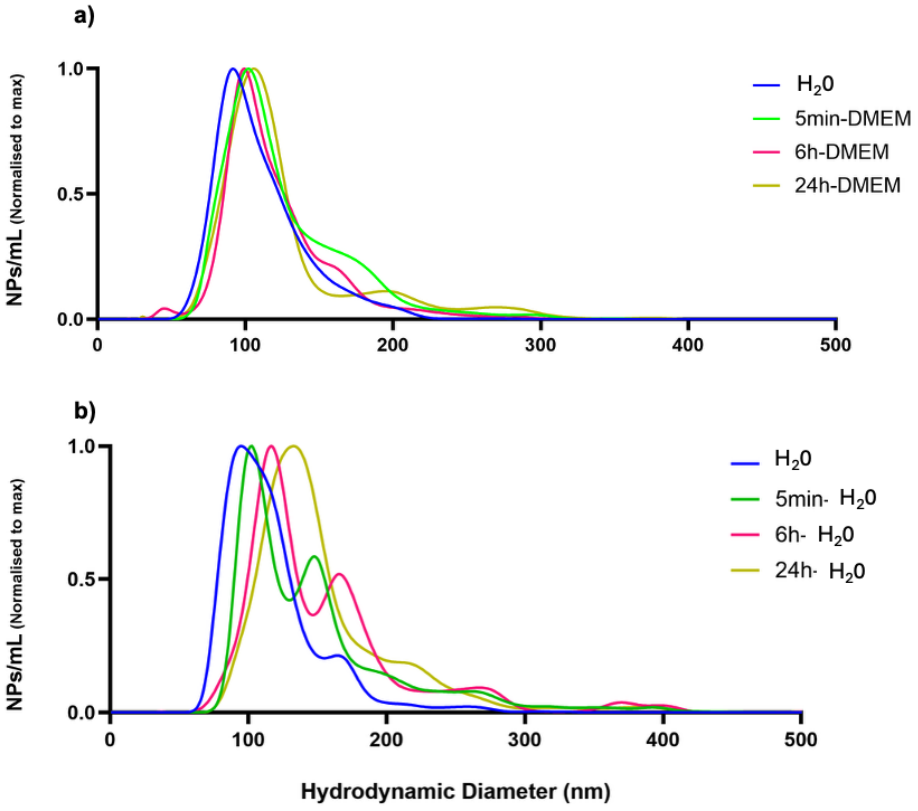

Figure 3.3: NTA size distributions of NaC–PERFECTA@PLGA nanoparticles after incubation in NIH-3T3-conditioned medium (conditioned for 6 h) at 5 min, 6 h, and 24 h. Normalised particle concentration is plotted as a function of hydrodynamic diameter (nm). Prior to analysis, samples were diluted 1:5000 in **(a)** DMEM without phenol red or **(b)** ultrapure water (H_2O). The control (H_2O) corresponds to nanoparticles, not incubated in NIH-3T3-conditioned medium, diluted in water.

Following NTA measurements of NPs-PC complex, obtained in CAR-T conditioned medium, were carried out after 1:5000 dilution exclusively in DMEM without phenol red. As shown in Figure 3.4, the hydrodynamic diameter of nanoparticles incubated in CAR-T-conditioned medium, increased during the first hour of incubation, consistent with initial protein adsorption and corona formation. At subsequent time points, at 24 h, the measured size progressively decreased, reaching values comparable to the reference measurement of NPs in water.

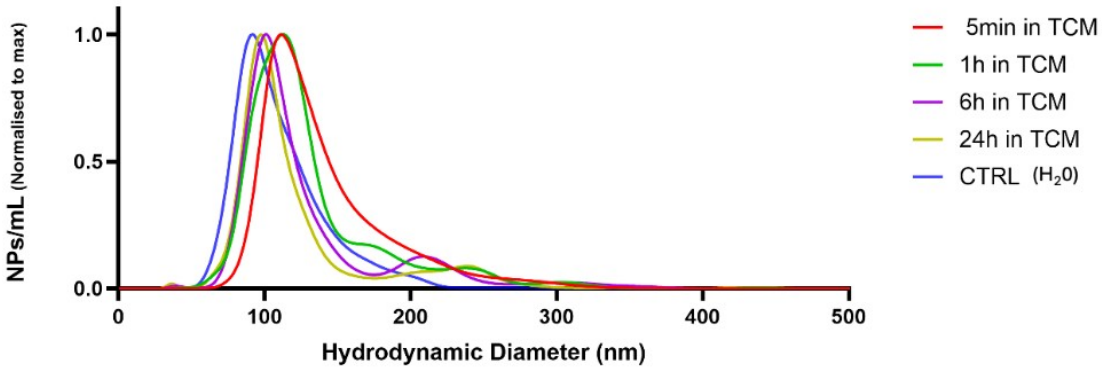

Figure 3.4: NTA size distributions in different time points of NaC–PERFECTA@PLGA–Rhodamine-B nanoparticles after incubation in CAR-T-conditioned medium supplemented with serum at 5 min, 1 h, 6 h, and 24 h. Prior to analysis, each sample was diluted 1:5000 in DMEM without phenol red. The control (CTRL) corresponds to nanoparticles diluted in ultrapure water (mQw). Normalised particle concentration is plotted as a function of hydrodynamic diameter.

Within the first 5min of incubation, the size distribution shifts toward larger diameters (+27.3% d_{h} relative to CTRL), consistent with early protein adsorption. By 24 h, the profile substantially overlaps with the water reference, yet a residual mean d_{h} increase of 11.3%.

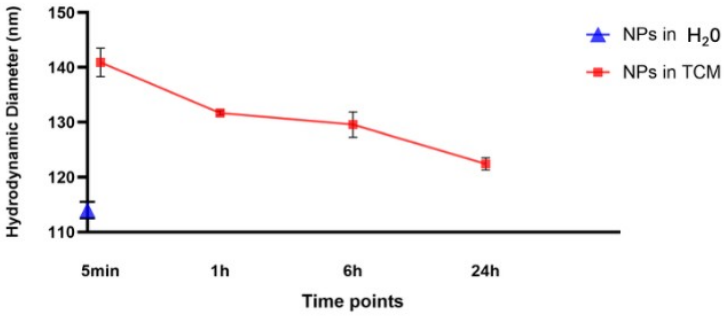

	D_h (nm)	SD (nm)
5 min TCM	140.9 ± 2.6	44.4 ± 2.6
1 h TCM	131.7 ± 0.4	48.8 ± 3.1
6 h TCM	129.6 ± 2.3	53.8 ± 0.9
24 h TCM	122.4 ± 1.1	50.5 ± 0.2
H_2O	110.4 ± 1.5	30.9 ± 1.2

Figure 3.5: Mean hydrodynamic diameter ($d_{\mathrm{h}} \pm$ SD) of NaC–PERFECTA@PLGA nanoparticles in CAR-T-conditioned medium at 5 min, 1 h, 6 h, and 24 h, compared with the water control (H_2O).

This residual offset is attributed to the formation of a stable protein corona around the nanoparticle surface. As described by Chirizzi *et al.* [70], the corona comprises two distinct components: the *hard corona* (HC), consisting of proteins tightly bound to the nanoparticle surface with slow exchange kinetics, and the *soft corona* (SC), formed by more weakly associated proteins in dynamic equilibrium with the surrounding medium. The temporal evolution of d_{h} is therefore consistent with an initial adsorption of loosely bound proteins, followed by progressive reorganization of intermolecular interactions within the adsorbed layer and consolidation of a compact protein corona architecture. When considered together with the parallel NIH-3T3 data (Figure 3.3), this dynamic temporal profile appears particularly evident and characteristic of nanoparticles exposed to T-cell-conditioned medium. By contrast, in NIH-3T3-conditioned DMEM,

mimicking culture medium of a model associated with greater uptake and phagocytic capacity, protein corona formation is rapid, already evident within the earliest phase of exposure, and remains stable over time, in agreement with the literature and with previous research reported by Chirizzi *et al.* [67, 70].

As expected, the formation and stabilization of the protein corona therefore appears to depend strongly on the culture medium, and not only on its protein composition. Indeed, the two conditioned media differ not only in the proteins they contain but also in their additives (salts, amino acids, and other small molecules), whose nature and concentration can markedly influence the stability of the adsorbed protein layer. [99].

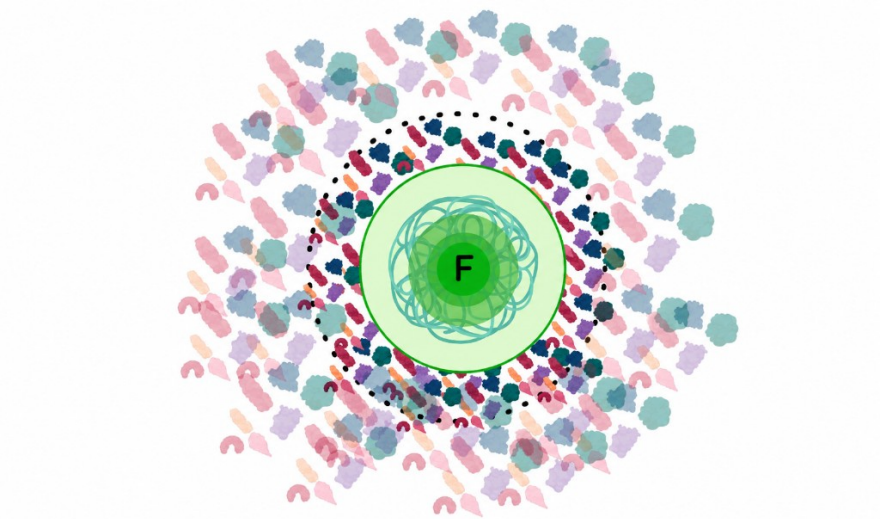

Figure 3.6: Schematic representation of the protein corona on a nanoparticle. The dashed boundary separates the Hard Corona (HC), whose proteins interact directly with the nanoparticle surface, from the Soft Corona (SC), which comprises proteins weakly bound to the HC layer. [70]

The progressive decrease in the hydrodynamic diameter of the nanoparticle–protein corona (NP–PC) complex over time may favour internalization by CAR-T cells. Unlike phagocytic cells, T lymphocytes possess a relatively small cytoplasmic volume and internalize nanoparticles primarily through receptor-mediated endocytic pathways rather than phagocytosis. Smaller NP–PC complexes are therefore more compatible with the uptake capacity of these cells. Moreover, adsorption of culture medium proteins onto the nanoparticle surface confers on the NP–PC complex a biological identity more closely resembling endogenous components of the cellular microenvironment, thereby reducing recognition as a foreign entity and promoting more efficient internalization during *ex vivo* labelling.

3.3 CAR-T Cell Labeling Efficiency and Viability

In this section are reported the results of five independent *ex vivo* labelling experiments on human anti-B7-H3 CAR-T cells incubated with PERFECTA@PLGA–Rhodamine B nanoparticles. In ^{19}F-MRI-based cell tracking, accurate removal of non-internalized nanoparticles is essential to avoid overestimating cellular labelling efficiency. This is particularly critical for cells in suspension, where residual free nanoparticles or nanoparticles bound to the cell surface may contribute to the measured ^{19}F signal. For this reason, labelled CAR-T cells require a stringent purification procedure before downstream NMR and MRI analyses.

3.3.1 CAR-T Cell Recovery with Density Gradient Purification

The purification protocol by density gradient centrifugation on Ficoll-Paque and Percoll, as described in Section 2.6.2, aims at maximizing cell recovery while reducing free and surface-associated nanoparticles, thereby improving the ^{19}F-MRI signal predominantly originating from intracellular fluorine. Cell recovery after density gradient purification was quantified according to Equation 2.24 as the percentage of viable CAR-T cells recovered after centrifugation relative to the pre-gradient count. To compare the purification strategies outlined in Section 2.6.2, recovery rates were analysed across three experimental groups. The workflow was designed to progressively evaluate different purification conditions, starting from the standard Ficoll-based procedure previously optimized and used throughout the initial experiments, followed by the introduction of an EDTA/BSA-containing Staining Buffer to improve cell handling and recovery, and finally by the assessment of Percoll as an alternative density-gradient purification strategy. For each experimental group, the control consisted of unlabelled CAR-T cells subjected to the same density gradient centrifugation procedure. Mean recovery and standard deviation (mean $\pm$ SD) are reported with the experimental details for each group described below.

1. For the reference protocol based on Ficoll-Paque and PBS 1X (Ficoll + PBS 1X), data from eight independent experiments were pooled, including experiments from Lobello's previous study [85] and from the present thesis.

2. To evaluate the effect of replacing PBS 1X with EDTA/BSA-containing staining buffer (SB), one additional labelling experiment was conducted in the present work using the Ficoll+ SB procedure. Crucially, in this same experiment the Ficoll+PBS 1X condition was processed in parallel on aliquots taken from the identical post-labelling cell suspension. This paired design allowed recovery to be compared between the two wash conditions, while keeping constant the upstream labelling step.

3. Finally, recovery was assessed in four independent experiments in which labelled CAR-T cells were purified using Percoll gradients and EDTA/BSA-containing Staining Buffer (Percoll+SB), following the gradient formats described in Section 2.6.2. In the first of these experiments, both Percoll configurations summarized in Table 2.8 were tested in parallel: the four layer multigradient (100/80/40/30%) and the simplified 70/30% discontinuous gradient. The simplified 70/30% format resulted in markedly higher cell recovery, reaching 67.3% compared with 31% obtained with the multigradient configuration.

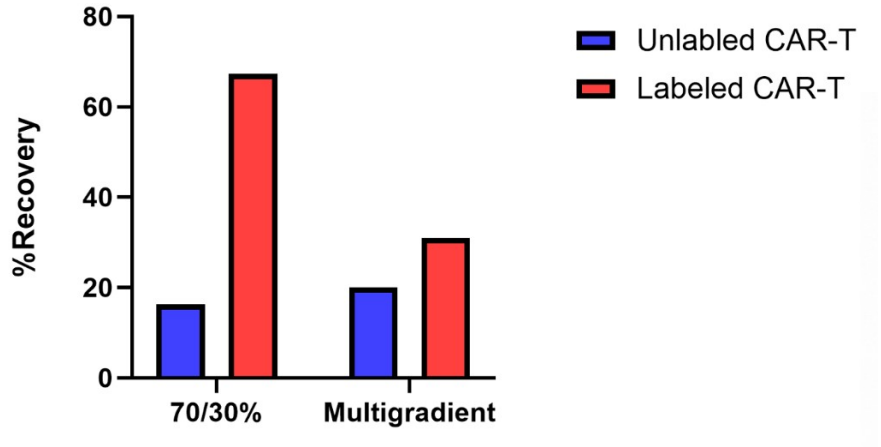

Figure 3.7: Comparison of CAR-T cell recovery (%) between the 70/30% discontinuous gradient and the four-layer multigradient, tested in parallel within the same experiment. Recovery is reported separately for unlabeled and labeled cells processed with the same gradient protocol.

This observation is attributed to the heterogeneity of the labelled CAR-T population, because internalization of nanoparticles increases the buoyant density of individual CAR-T cells proportionally; so cells labelled with different amounts of nanoparticles do not band at a single and well defined interface. Under the multigradient configuration, this density probably spreads and partitions the population across several interfaces (30/40% and 40/80%), producing thin cell rings that are difficult to recover and visualize. By contrast, the 70/30% gradient provides a single collection interface at which labelled cells with only modest differences in buoyant density can accumulate together, substantially improving recovery yield (Figure 3.8).

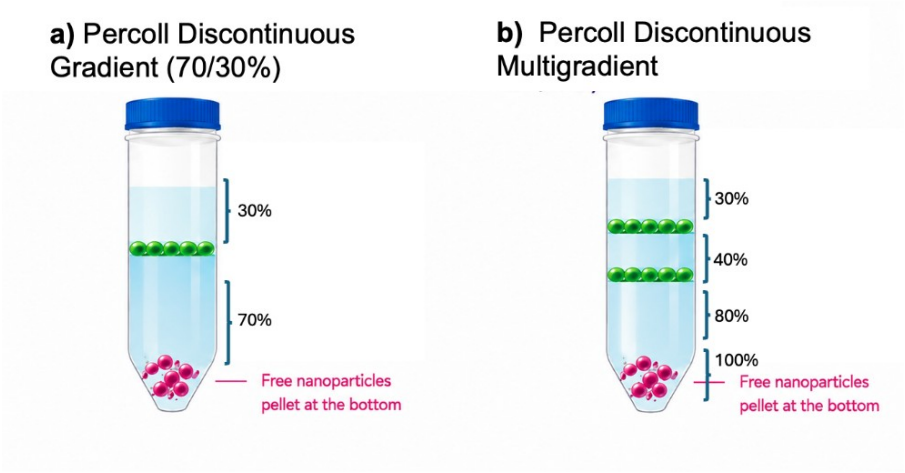

Figure 3.8: Schematic representation of CAR-T cell partitioning after Percoll + Staining Buffer centrifugation. **(a)** In the 70/30% discontinuous gradient, labelled CAR-T cells (green) band at a single interface between the 30% and 70% layers, whereas free nanoparticles (red) sediment to the pellet at the bottom of the tube. **(b)** In the four-layer multigradient, the density heterogeneity of the labelled population partitions cells across multiple interfaces (30/40% and 40/80%), while free nanoparticles again pellet at the bottom.

On the basis of this result, the subsequent three labeling experiments were performed exclusively with the 70/30% discontinuous Percoll gradient.

Figure 3.9 summarizes the recovery yields obtained across the three purification strategies described above. For each condition, mean recovery and standard deviation are reported separately for unlabeled and labeled CAR-T cells processed with the same density gradient protocol. Under Ficoll-Paque + PBS 1X, recovery was low for both populations, with a marked reduction for labeled cells. Replacement of PBS 1X with EDTA/BSA-containing Staining Buffer (Ficoll+SB) substantially improved recovery of unlabeled cells, whereas labeled cell recovery remained limited. Percoll+SB with the 70/30% discontinuous gradient provided the most balanced performance, yielding comparable recovery for unlabeled and labeled CAR-T cells.

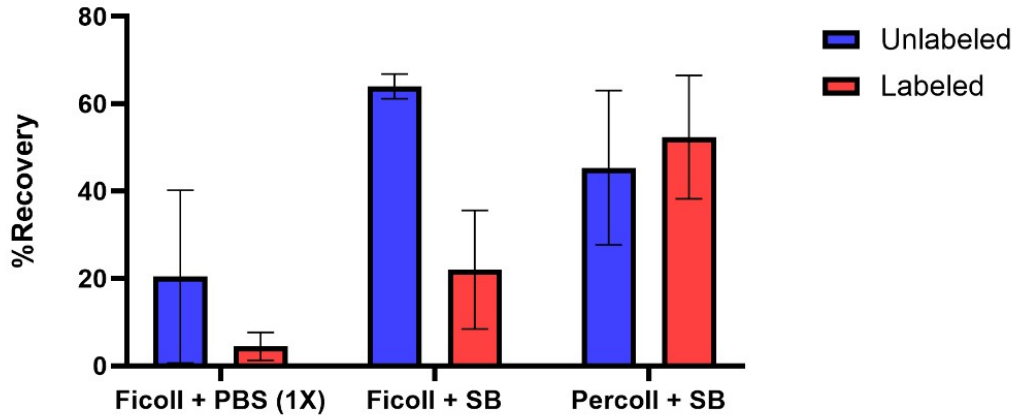

Figure 3.9: CAR-T cell recovery after density gradient purification (mean ± SD, %). Comparison across Ficoll-Paque + PBS 1X, Ficoll-Paque + Staining Buffer, and Percoll + Staining Buffer (70/30%) for unlabeled and labeled CAR-T cells.

Table 3.1: CAR-T cell recovery after density gradient purification (mean ± SD, %).

Purification condition	**Unlabelled CAR-T (%)**	**Labelled CAR-T (%)**
Ficoll-Paque + PBS 1X	20.44 ± 19.79	4.42 ± 3.21
Ficoll-Paque + Staining Buffer	64.00 ± 2.82	22.00 ± 13.57
Percoll + Staining Buffer (70/30%)	45.38 ± 17.65	52.36 ± 14.21

Taken together, the recovery data in Figure 3.9 and Table 3.1 support the purification rationale outlined in Section 2.6.2. The marked improvement observed upon replacing PBS 1X with MACS® Staining Buffer is therefore attributed primarily to the combined action of bovine serum albumin (BSA) and ethylenediaminetetraacetic acid (EDTA) in the buffer formulation. As described in Section 2.6.2, BSA saturates cell membrane binding sites and competes with opsonins and the nanoparticle protein corona for adsorption onto the plasma membrane, favouring detachment of non-internalized particles, whereas EDTA chelates Ca^{2+} and Mg^{2+}, disrupting calcium-mediated electrostatic bridges between negatively charged nanoparticles and the cell surface. The further gain achieved with Percoll is instead attributed to the tunable density architecture of Percoll®, which allows the gradient to be adapted to the buoyant density of labelled CAR-T cells. On this basis, Percoll with the 70/30% gradient + Staining Buffer was adopted as the optimized post-labelling purification protocol for subsequent experiments.

3.3.2 Assessment of Cell Viability with Flow Cytometry

The cytocompatibility of the labelling protocol was evaluated by monitoring CAR-T cell viability using trypan blue exclusion assay and flow cytometric analysis, as described in Section 2.6.1, comparing the gating on unlabelled and labelled CAR-T cell populations. The **Standard labeling condition** consisted of 3.33×10^6 anti-B7-H3 CAR-T cells labelled with NaC–PERFECTA@PLGA nanoparticles for 6 h under the *Standard* fluorine labelling concentration (3.13×10^{19} ^{19}F/mL, 1X).

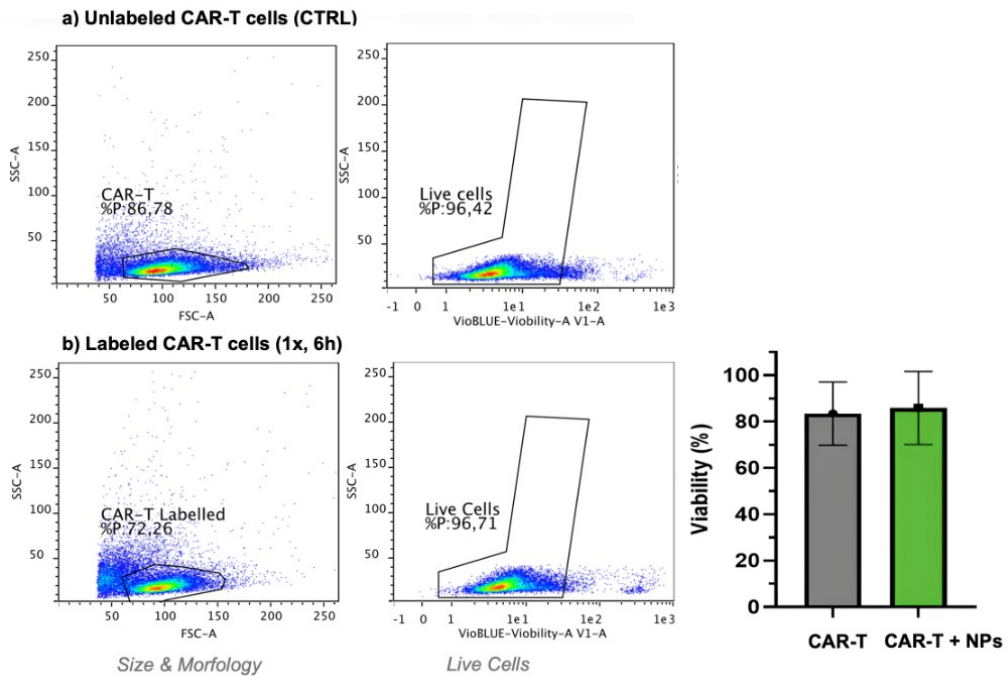

Figure 3.10: Flow cytometric assessment of CAR-T cell viability. **(a)** Representative gating of unlabelled CAR-T cells (CTRL) for size and morphology (FSC-A vs. SSC-A) and live-cell discrimination (VioBLUE-Viability-A vs. SSC-A). **(b)** Representative gating of labelled CAR-T cells under the 1×, 6 h condition. Summary bar chart comparing viability (%) of unlabelled CAR-T cells and CAR-T cells labelled with NaC–PERFECTA@PLGA nanoparticles (CAR-T + NPs).

Control cells processed through the same protocol, but without nanoparticles and with the addition of an equivalent volume of H_2O, showed comparable viability across all experiments. This confirmed that the handling procedures and Percoll-based purification did not inherently compromise cell health. The high viability of labelled cells across all experiments validated the cytocompatibility of the NaC–PERFECTA@PLGA nanoparticle formulation at the tested concentrations.

A second labelling experiment was then performed using the same number of anti-B7-H3 CAR-T cells incubated for 6 h with NaC–PERFECTA@PLGA nanoparticles at the *Doubled* fluorine labelling concentration, corresponding to 6.26×10^{19} ^{19}F/mL (2x (6 h)). In the same experiment, additional cells were labelled for 18 h using either the *Standard* or the *Doubled* fluorine concentration, referred to as 1x (18 h) and 2x (18 h), respectively. The four labelling conditions and their corresponding abbreviations are summarized in Table 3.2.

Table 3.2: Summary of CAR-T labelling conditions tested by flow cytometry.

Condition	Labeling concentration (^{19}F/mL)	CAR-T cell number
1×, 6 h	3.13×10^{19}	3.33×10^{6}
2×, 6 h	6.26×10^{19}	3.33×10^{6}
1×, 18 h	3.13×10^{19}	3.33×10^{6}
2×, 18 h	6.26×10^{19}	3.33×10^{6}

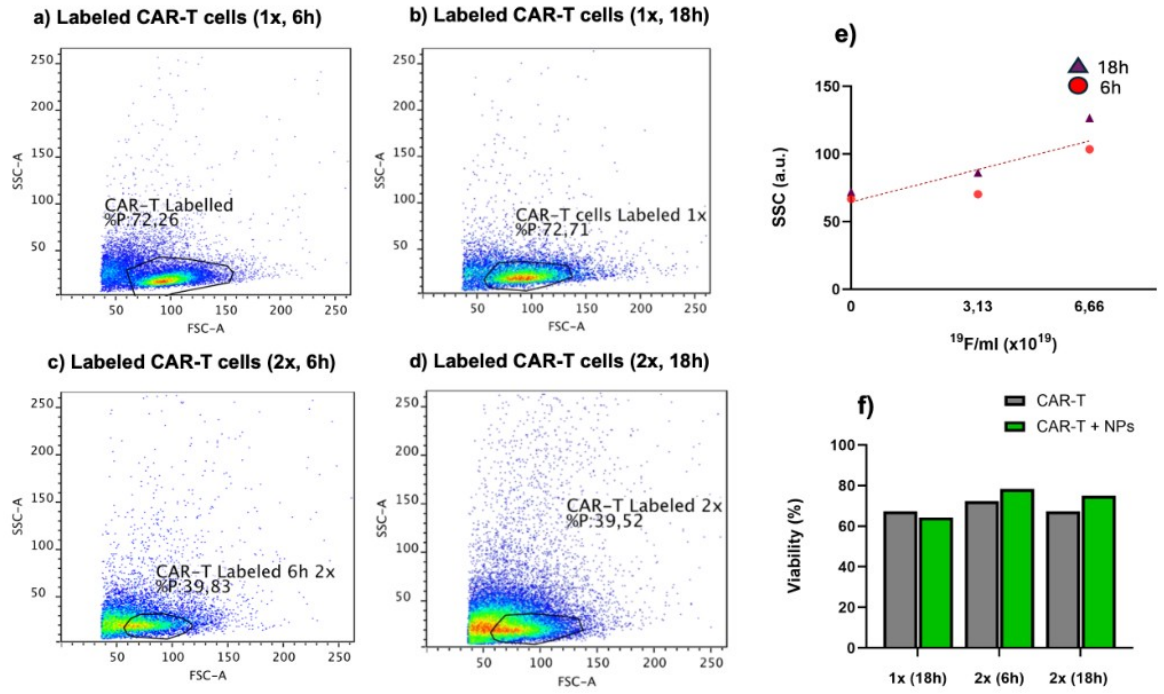

Figure 3.11: Flow cytometry size & morphology representation of a) CAR-T cells labeled in standard fluorine concentration for 6 h; b) CAR-T cells labeled in standard fluorine concentration for 18 h; c) CAR-T cells labeled in doubled fluorine concentration for 6 h; d) CAR-T cells labeled in doubled fluorine concentration for 18 h; e) simple linear regression of intracellular granulosity increase SSC-A (a.u.) over different ^{19}F/mL concentrations, f) viability percentage among all conditions calculated by flow cytometry, in CAR-T morphological gate.

As highlighted in Figure 3.11, the viability percentage remains comparable between the unlabelled control condition and the labelled population, despite the improvement in nanoparticle uptake. This confirms the cytocompatibility of the NaC–PERFECTA@PLGA nanoparticle formulation under alternative labelling conditions.

The increased nanoparticle uptake trend was further supported by linear regression analysis of intracellular granulosity, quantified within the CAR-T morphological gate, as a function of labelling fluorine concentration. Flow cytometry analysis showed that SSC, reflecting cell granularity/internal complexity, increased with fluorine concentration, as indicated by the positive slopes of the fitted regression lines. Comparison of 6h (circles) and 18h (triangles) incubation times showed higher granulosity after prolonged labelling, in line with enhanced nanoparticle uptake during extended exposure. Furthermore, the 1x (18h) condition exhibited slightly lower granulosity than 2x conditions.

3.3.3 Assessment of nanoparticle uptake by flow cytometry

A primary assessment of nanoparticle uptake was carried out by flow cytometric analysis of Rhodamine-B fluorescence within labelled cells (Section 2.6.3). Under the **Standard labeling condition**, labelling efficiency reached 100% when quantified within

the live-cell population included in the CAR-T morphological gate. (Figure 3.12). To normalize fluorescence intensity values across experiments, nanoparticle uptake was additionally expressed as Mean Fluorescence Intensity (MFI) fold change, calculated as the ratio between the MFI of the gated labelled population and the corresponding unlabelled control acquired under identical settings:

$$\text{Fold Change MFI} = \frac{\text{MFI}_{\text{labelled}} - \text{MFI}_{\text{unlabelled}}}{\text{MFI}_{\text{unlabelled}}}, \tag{3.1}$$

where MFI denotes the arithmetic mean of the fluorescence intensity values recorded for all events within the selected gate. A fold change of unity indicates how much a quantity changes between the analysed condition and the respectively control, whereas values around 50 indicates that the mean fluorescence of the labelled population was 50 times that of the unlabelled control, confirming successful nanoparticle uptake.

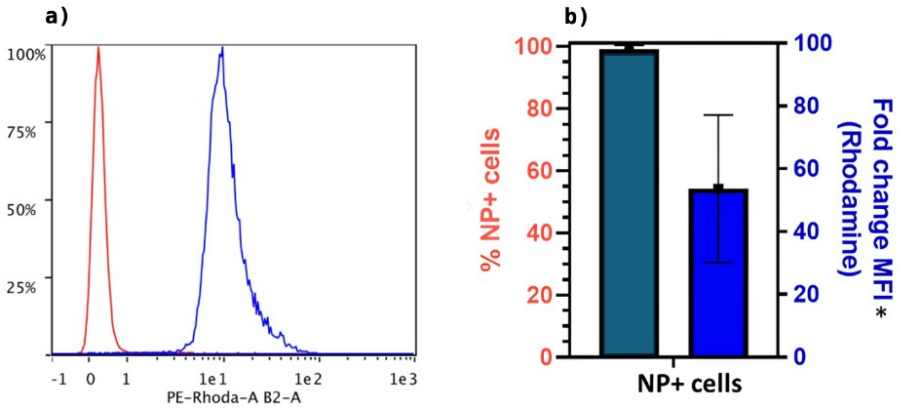

Figure 3.12: Flow cytometry assessment of nanoparticle uptake under the Standard labeling condition. **(a)** Representative histogram of Rhodamine-B fluorescence (PE channel) for unlabelled (red) and labelled (blue) CAR-T cells, shifted to the positive decades. **(b)** Percentage of nanoparticle-positive (NP^+) cells and fold change in mean fluorescence intensity (Fold Change MFI) relative to the unlabelled control.

Subsequently, Rhodamine-B fluorescence was assessed by flow cytometry for the **Doubled labeling condition** at 6 h and 18 h, and for the **Standard labeling condition** at 18 h. The results are shown in Figure 3.13.

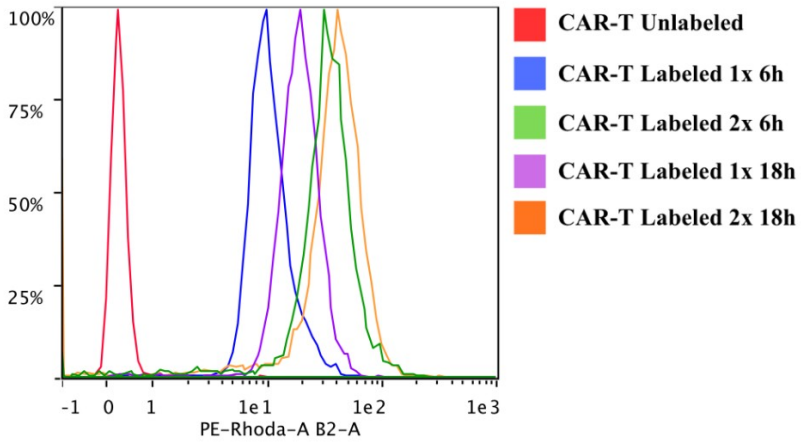

Figure 3.13: Rhodamine-B fluorescence histograms (PE channel) comparing unlabelled CAR-T cells (red) with labelled populations under Standard (1×) and Doubled (2×) fluorine concentrations at 6 h and 18 h incubation times.

As shown in Figure 3.13, doubling the labelling concentration produced a further rightward shift of the fluorescence signal toward higher decades, indicating increased Rhodamine-B fluorescence and, consequently, greater nanoparticle uptake. Likewise, extending the incubation time from 6 h to 18 h resulted in an additional shift relative to the corresponding 6 h condition, consistent with progressive nanoparticle internalization during prolonged exposure. Importantly, labelling efficiency reached 100% of the population in all labeled conditions, when quantified on live cells within the CAR-T morphological gate.

3.4 ^{19}F-MRI imaging and ^{19}F loading quantification

CAR-T cells labeled under the **Standard labeling condition**, corresponding to the *Standard* fluorine concentration and incubation time, were imaged by ^{19}F-MRI to verify the presence of the PERFECTA signal. Although this protocol achieved a cellular fluorine uptake higher than values reported in the literature for CAR-T cells labelled with other nanoparticle systems or fluorinated agents, the PERFECTA signal was not detectable above background. This was likely due to the limited number of labelled cells available for imaging, with cell pellets containing approximately $1-1.5\times10^5$ cells, remaining below the MRI detection threshold.

For this reason, alternative labelling conditions were explored to increase the ^{19}F content per cell by extending the incubation time and/or increasing the fluorine concentration. These conditions enabled the detection of a visible ^{19}F-MRI signal, as shown in Figure 3.14.

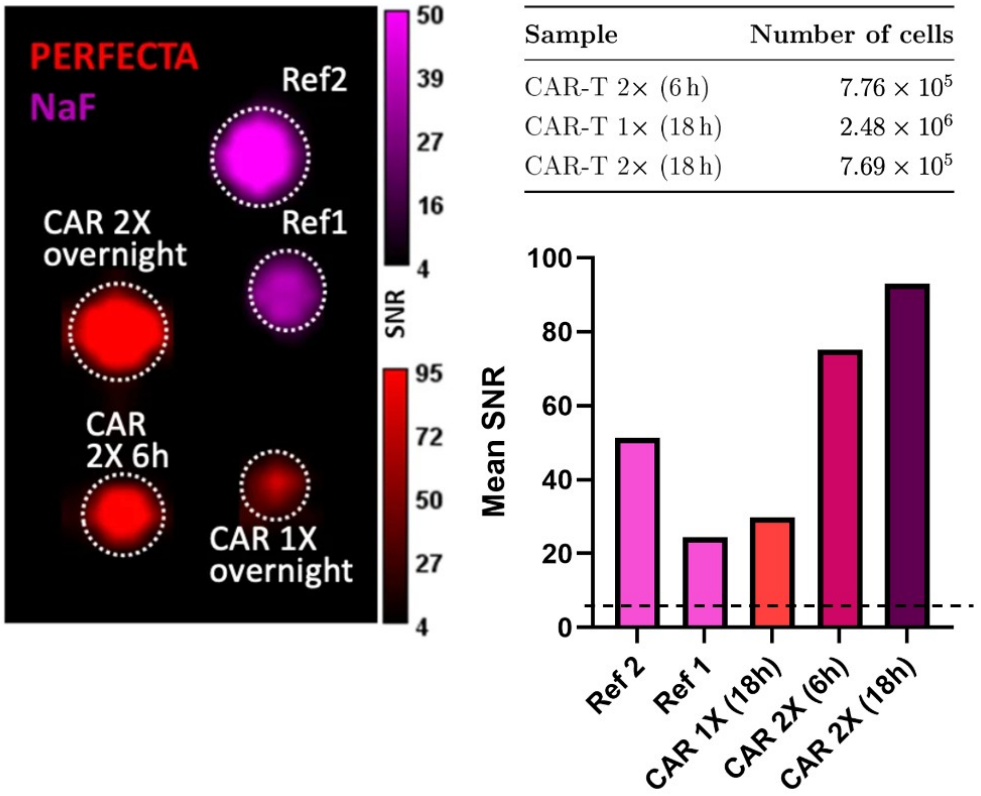

Figure 3.14: ^{19}F-MRI imaging of labelled CAR-T cell samples and NaF reference tubes. **Left:** ^{19}F-MRI images of labelled CAR-T cell pellets (red) and NaF references (magenta). **Top right:** number of cells per sample. **Bottom right:** mean signal-to-noise ratio (SNR) for cellular samples and reference tubes; the horizontal dashed line indicates the SNR detection threshold, below which the ^{19}F signal would no longer be reliably distinguishable from background noise; **Reference NaF 1:** $C_{\mathrm{ref},1} = 1 \times 10^{20}$ ^{19}F mL^{-1}; **Reference NaF 2:** $C_{\mathrm{ref},2} = 2 \times 10^{20}$ ^{19}F mL^{-1}.

The PERFECTA resonance was particularly prominent in the two samples labelled at doubled fluorine concentration (2×), in agreement with the higher intracellular payload fluorescence, whereas the signal from the standard fluorine concentration (1×) overnight, was slightly lower. In all cases, the measured SNR values were well above the detection threshold, enabling clear visualisation of all labelled cell pellets. According to the protocol described in Section 2.3.7, the fluorine content of each sample was quantified from the two MRI slices in which the cellular pellet was concentrated and therefore the ^{19}F signal was maximal. The results are summarized in Table 3.3.

Table 3.3: ^{19}F/cells content quantified by ^{19}F-MRI from the two pellet containing slices under alternative labelling conditions.

Sample	**^{19}F/cells**
CAR-T 2× (6 h)	1.6×10^{13}
CAR-T 1× (18 h)	2.06×10^{12}
CAR-T 2× (18 h)	2.08×10^{13}

3.4.1 ^{19}F quantification with ^{19}F-NMR

According to the protocol described in Section 2.3.5, after completion of the imaging analyses, the cellular samples were lysed and subjected to quantitative ^{19}F-NMR to obtain an independent confirmation of the actual fluorine content extrapolated from the ^{19}F-MRI images. A representative result from one of the labelling experiments conducted under the standard condition (1×, 6 h) is reported in Figure 3.15. Under this condition, a fluorine loading of 8.48×10^{11} ^{19}F/cell was obtained, calculated relative to 300×10^3 cells.

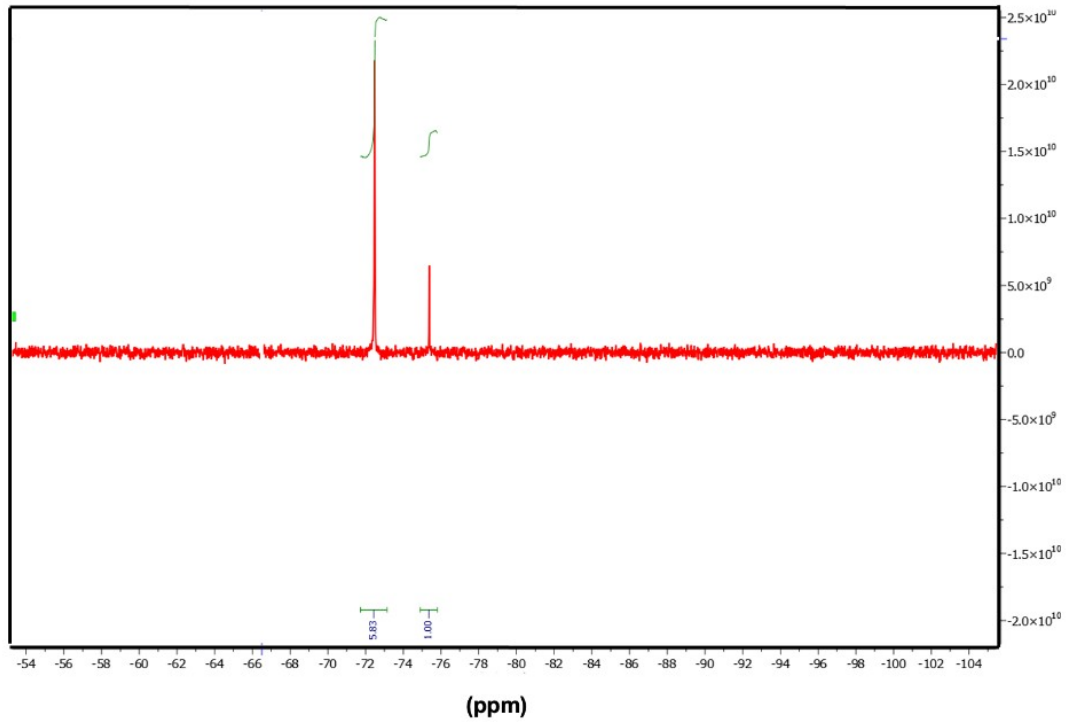

Figure 3.15: Representative quantitative ^{19}F-NMR spectrum of the CAR-T sample labelled under the standard fluorine concentration for 6 h (1×). The resonance at $\delta \approx -72.5$ ppm corresponds to intracellular PERFECTA released after cell lysis; the sharp signal at $\delta \approx -75.5$ ppm is the TFA external reference. $C_{\text{ref}} = 1.6 \times 10^{18}$ ^{19}F mL^{-1}.

Across all experiments performed under the standard labelling condition (1×, 6 h), the mean intracellular fluorine content was 9.39×10^{11} $\pm 5.5 \times 10^{11}$ ^{19}F/cell.

Quantitative ^{19}F-NMR was also performed on the samples from the last labelling experiment conducted under the alternative conditions, (Section 2.6.1). A representative ^{19}F-NMR spectrum of the CAR-T sample labelled at doubled fluorine concentration for 18 h is shown in Figure 3.16, where a fluorine loading of 1.73×10^{13} ^{19}F/cell was obtained, calculated relative to 769×10^3 cells.

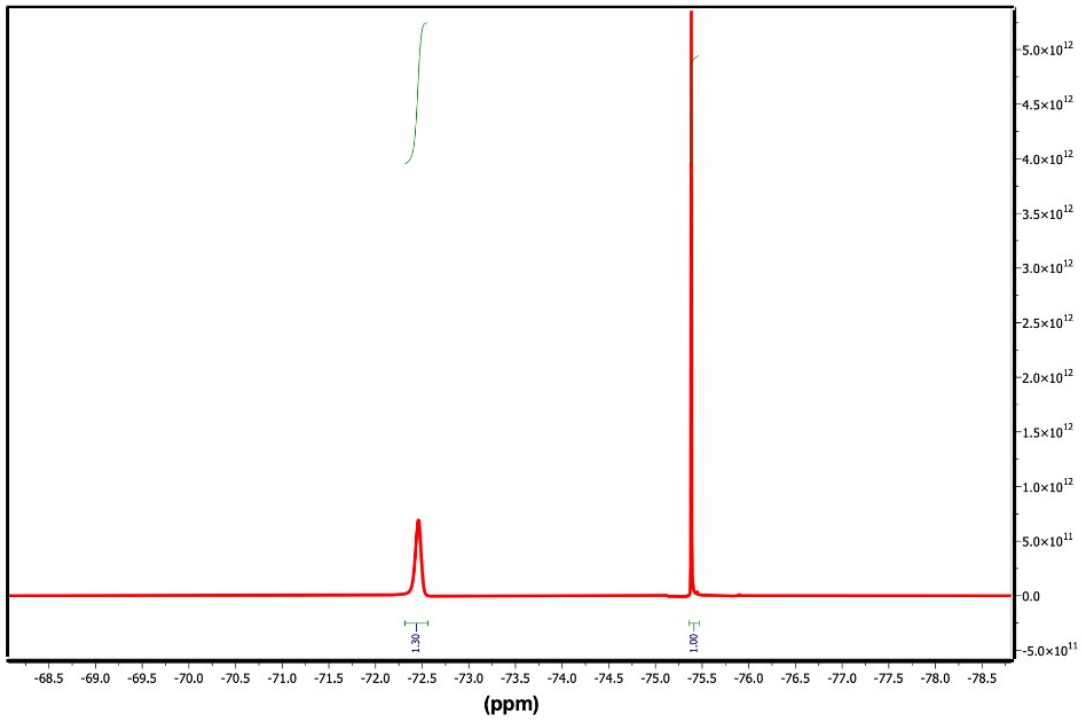

Figure 3.16: Representative quantitative ^{19}F-NMR spectrum of the CAR-T sample labelled at doubled fluorine concentration for 18 h (2×). The resonance at $\delta \approx -72.5$ ppm corresponds to intracellular PERFECTA released after cell lysis; the sharp signal at $\delta \approx -75.5$ ppm is the TFA external reference. Integrated peak areas (green) were used for fluorine quantification. $C_{\mathrm{ref}} = 2 \times 10^{20}$ ^{19}F mL^{-1}.

Across all experiments performed under the alternative labelling conditions, the mean intracellular fluorine content per cell quantified by ^{19}F-NMR is summarized in Table 3.4.

Table 3.4: ^{19}F/cell content quantified by ^{19}F-NMR from the samples labelled under alternative conditions.

Sample	**^{19}F/cell**
CAR-T 2× (6 h)	4.38×10^{12}
CAR-T 1× (18 h)	1.23×10^{11}
CAR-T 2× (18 h)	1.82×10^{13}

The ^{19}F-NMR quantification for the CAR-T 1× (18 h) condition is excluded from the analysis because it represents an outlier inconsistent with the corresponding ^{19}F-MRI measurement (Table 3.3); for this condition, only the ^{19}F-MRI quantification is considered reliable.

3.4.2 Assessment of nanoparticle uptake by Raman microscopy

Flow cytometry and ^{19}F-MRI/^{19}F-NMR quantify nanoparticle uptake at the population level, but neither modality alone can verify the correctly internalization of nanoparticles inside CAR-T cells and localize them at the subcellular level. For this reason, Raman imaging was employed as a complementary assay capable of resolving the spatial distribution of PERFECTA within individual CAR-T cells at micrometre scale (Section 2.3.6). Proof-of-concept Raman experiments were performed on CAR-T cells labelled under **Standard labeling condition**, 6 h incubation at the standard fluorine concentration (Section 2.6.1), to verify where the nanoparticles were located inside the cells.

Raman mapping requires single cells to remain firmly adherent and optically accessible on a suitable substrate. For this purpose, a preliminary adhesion assay was carried out on quartz bottom Petri dishes coated with poly-D-lysine (PDL), following the protocol described in Section 2.3.6 and illustrated in Figure 2.14. There were assessed five different time points (2 h, 4 h, 18 h, 24 h, 48 h) to discover which best achieved the maximum attachment of cells on the substrate. At each selected time point, non-adherent cells were removed through gentle washing steps using culture medium and PBS. The degree of cell adhesion was qualitatively assessed by bright-field microscopy based on the number of cells remaining attached to the well surface after washing. The optimal results was achieved after 24 hours of incubation, as illustrated in Figure 3.17.

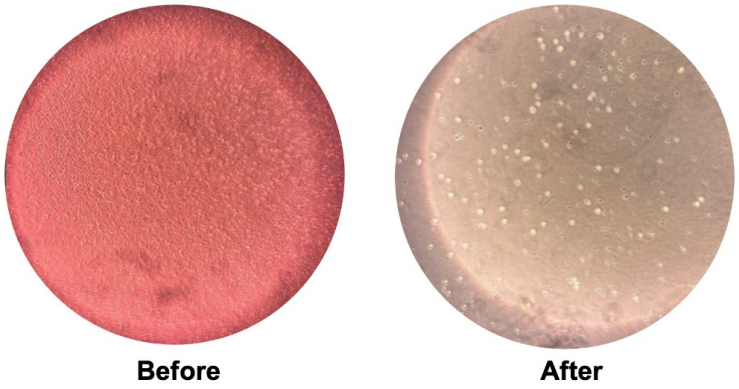

Figure 3.17: Representative bright-field microscopy images of CAR-T cell adhesion on poly-D-lysine (PDL)-coated quartz-bottom Petri dishes, acquired after 24 h incubation. **Before:** cells prior to washing, showing a densely packed population on the substrate. **After:** population of cells that remaining firmly attached after the washing step.

Analyses performed on individual cells, according to the protocol described in Section 2.3.6, showed hyperspectral Raman maps from which representative spectra could be extracted, enabling quantification of the PERFECTA signal across the mapped pixels (magenta in Figure 3.18).

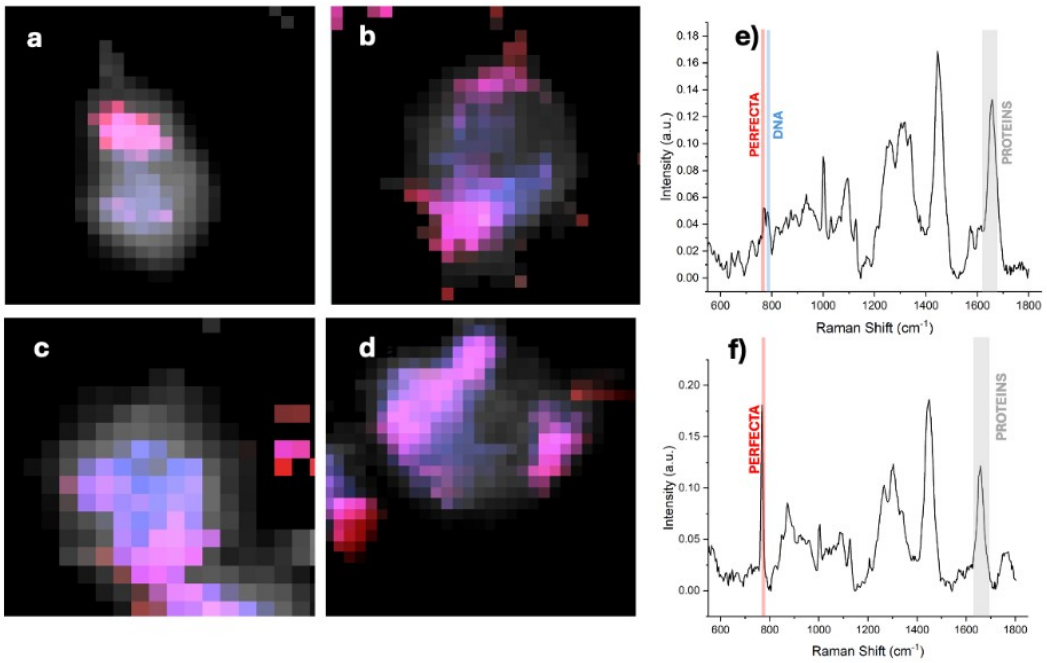

Figure 3.18: Raman imaging of labelled CAR-T cells. **(a–d)** False-colour Raman maps of individual CAR-T cells showing the spatial distribution of PERFECTA (magenta), DNA (blue), and proteins (grey). **(e)** Representative Raman spectrum of a labelled CAR-T cell (image a) in the fingerprint region (600–1800 cm^{-1}), with vertical markers at the PERFECTA band (∼770 cm^{-1}), the DNA contribution (∼790 cm^{-1}), and the protein amide region (∼1650 cm^{-1}). **(f)** Representative Raman spectrum of a labelled CAR-T cell (image d).

The PERFECTA signal is localized inside the cell, within the cytoplasmic region, in the perinuclear region. As shown in panel (f), the PERFECTA peak associated with the magenta pixels is clearly visible. In panel (e), by contrast, the peak appears very close to the DNA region, indicating that, because the image is two-dimensional, the signal may arise from nanoparticles positioned in correspondence with the nucleus, while still remaining within the cytoplasmic compartment. Taken together, this complementary approach confirms that nanoparticle internalization occurred correctly and that PERFECTA is detected within the intracellular compartment.

3.5 Functional Validation of CAR-T cells in Cytotoxicity Assays

Following the CAR-T cell labelling experiments performed under the different conditions described above, each labelling condition was functionally validated to assess whether nanoparticle labelling affected the targeted cytotoxic activity of CAR-T cells. Specifically, the assay was designed to verify that labelled CAR-T cells retained their ability to recognize and kill B7-H3-expressing glioblastoma tumour cells. Five co-culture experiments were therefore performed, in which labelled CAR-T cells were co-cultured with U-87 glioblastoma cells at a 1:1 effector to target ratio (cell number ratio)

for 3 days, according to the protocol described in Section 2.5.4. For each condition, controls were represented by Non Trasduced T-cells (NT), to evaluate whether anti-B7-H3 CAR-T cells exert superior cytotoxic activity against glioblastoma target cells, and CAR-T cells unlabeled (CAR-T) to evaluate the eventually influence of nanoparticles on the cytotoxicity activity. Co-culture experiments were primarily performed under the **Standard labeling condition**, (6 h at the standard ^{19}F labelling concentration; Section 2.6.1), as reported in Figure 3.19 and Table 3.5.

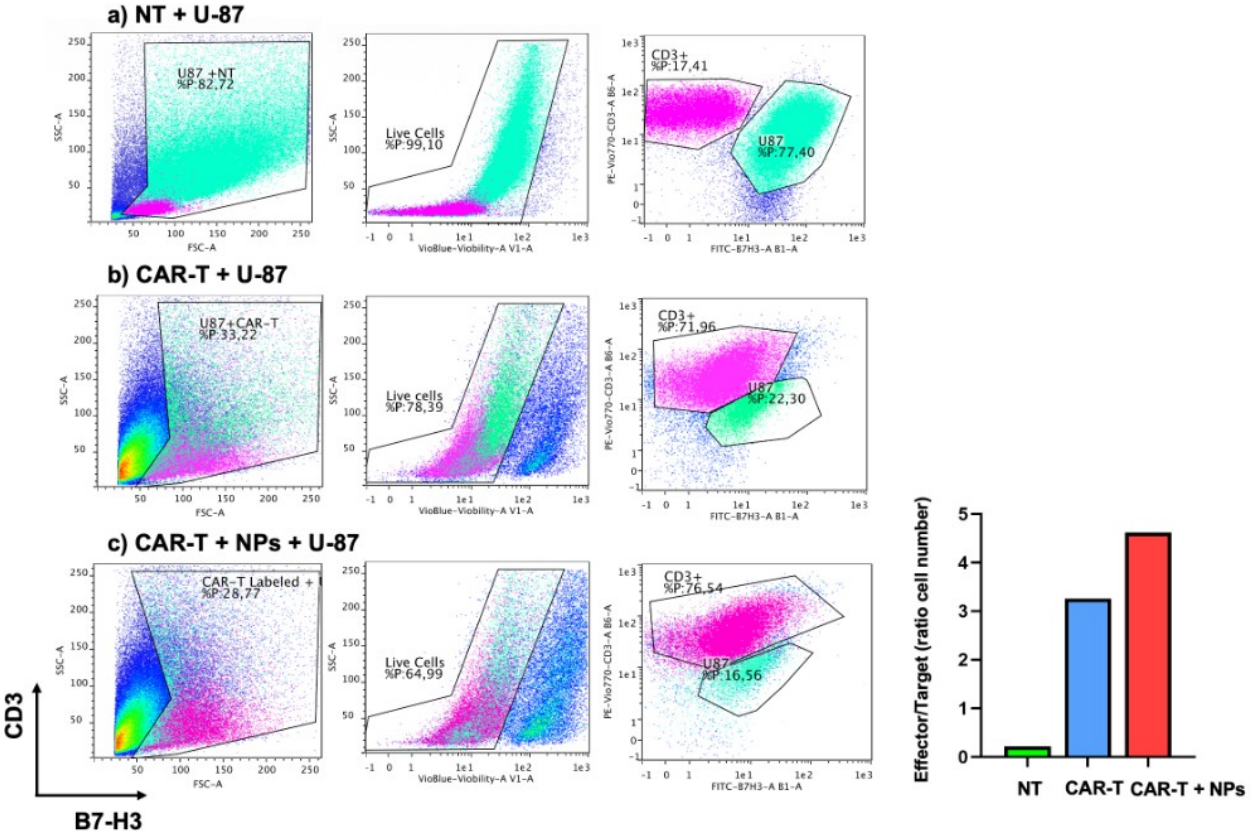

Figure 3.19: Flow cytometry analysis of co-culture conditions after 3 days: **(a)** non-transduced T cells and U-87 target cells; **(b)** CAR-T cells and U-87 target cells; **(c)** labelled CAR-T cells and U-87 target cells. Gating strategy: FSC-A vs. SSC-A, viability, and immunophenotyping (CD3 on the y axis, B7-H3 on the x axis). Bar chart (right): effector to target cell ratio for each condition (NT, CAR-T, CAR-T + NPs).

Table 3.5: Cell counts measured in co-culture cytotoxicity assays.

Cells sample	**Target (cell/μL)**	**Effector (cell/μL)**
a) NT	552,29	124,23
b) CAR-T	56,57	182,52
c) CAR-T + NPs	31,96	147,75

From the extrapolated cell density values (cells/μL) reported in Table 3.5 and from

the effector to target ratio, the killing activity exerted by effector cells over the 3-day co-culture period can be undesrtood. In the first condition, Non Trasduced T cells (NT) against U-87 cells, cytotoxic activity was markedly limited; the U-87 population density remained comparatively high and the effector to target ratio was below unity (0.22). In the second condition, CAR-T cells against U-87 cells, killing was substantially amplified, yielding a ratio > 1, indicating that effector cells outnumbered target cells by a factor of 3.26. In the third condition, labeled CAR-T cells against U-87 cells, cytotoxic activity was not compromised; on the contrary, effector cells slightlyexceeded target cells by a factor of 4.62, reflecting the strongest reduction in target cell density among the three conditions. Taken together, these results therefore confirm that nanoparticle labelling under the standard labelling condition did not impair the cytotoxic activity of CAR-T cells against U-87 glioblastoma target cells.

The last co-culture experiment was carried out under the other labeling conditions described above to verify if the killing activity was preserved, following the protocol described in Section 2.5.4, as shown in Figure 3.21. First of all, the morphological appearance of the cells was assessed by microscopy, as shown in Figure 3.20.

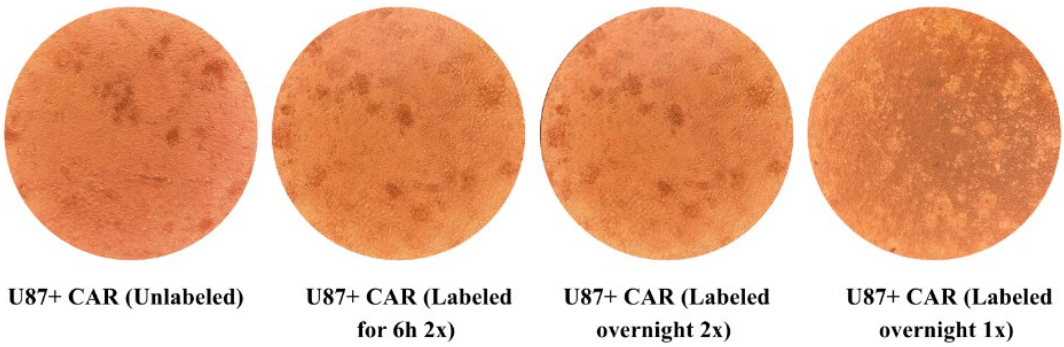

Figure 3.20: Morphological assessment of U-87 and CAR-T co-cultures after 3 days, acquired by optical microscopy. From left to right: **(1)** U-87 + unlabelled CAR-T; **(2)** U-87 + CAR-T labelled for 6 h under the doubled fluorine concentration (2×); **(3)** U-87 + CAR-T labelled overnight (18 h) under the doubled fluorine concentration (2×); **(4)** U-87 + CAR-T labelled overnight (18 h) under the standard fluorine concentration (1×).

Bright-field microscopy observations revealed the formation of CAR-T cell clusters in all co-culture conditions, including both unlabelled and labelled effector populations. These clonal-like aggregates are consistent with CAR-T cells activation and proliferative expansion following antigen recognition and engagement in the killing assay, providing morphological evidence that labelled cells retain functional responsiveness against U-87 glioblastoma target cells.

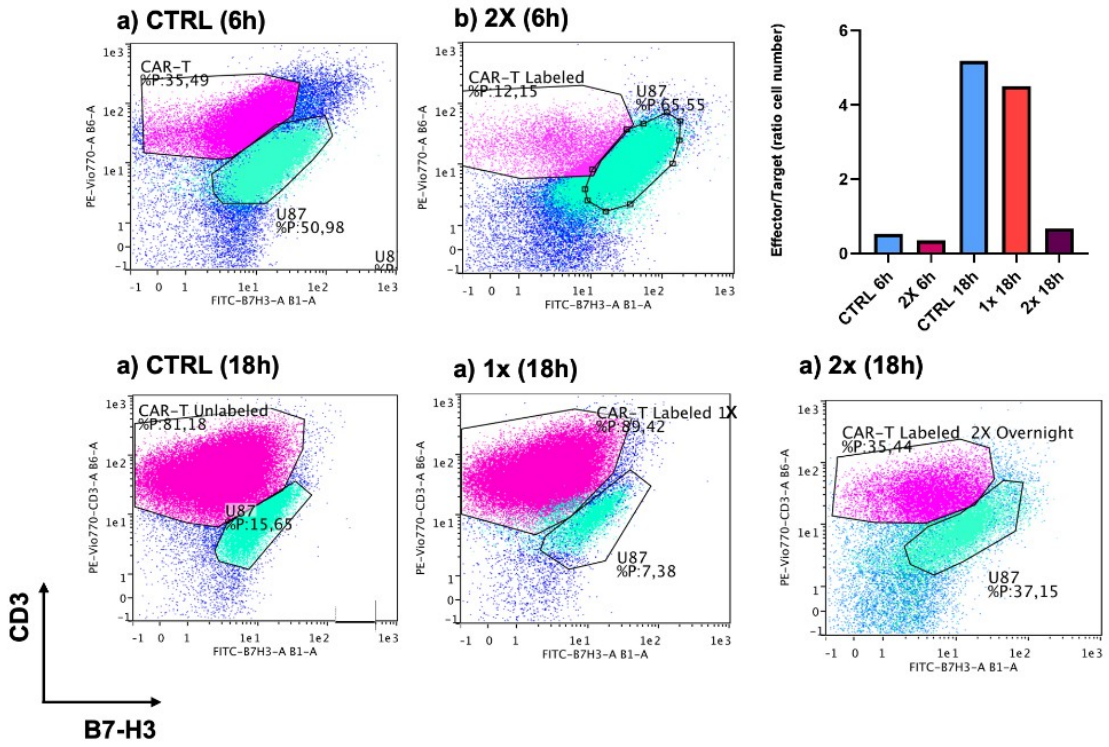

Figure 3.21: Flow cytometry analysis of co-culture conditions after 3 days under alternative labelling protocols: **(a)** unlabelled CAR-T control at 6 h; **(b)** CAR-T labelled for 6 h under the doubled fluorine concentration (2×); **(c)** unlabelled CAR-T control at 18 h (overnight); **(d)** CAR-T labelled overnight (18 h) under the standard fluorine concentration (1×); **(e)** CAR-T labelled overnight (18 h) under the doubled fluorine concentration (2×). Gating strategy: immunophenotyping (CD3 on the y axis, B7-H3 on the x axis). Bar chart (right): effector to target cell ratio for each condition.

For the 6 h labelling condition at the doubled fluorine concentration (2×), an experimental issue was encountered. Indeed, even the unlabelled CAR-T control showed an effector to target ratio < 1, despite unlabelled CAR-T cytotoxicity against U-87 being well established in the 4 previous co-culture experiments and yielding strong killing under standard conditions. (Figure 3.19). These results are therefore considered invalid for this labelling protocol.

For overnight (18 h) labelling, both the unlabelled control and the standard (1×) concentration preserved effector to target ratios above unity. In the control, effector cells outnumbered target cells by a factor of 5.18, whereas CAR-T cells labelled overnight at the standard concentration exceeded target cells by a factor of 4.5. By contrast, overnight labelling at the doubled (2×) concentration yielded a ratio below unity.

Flow cytometry analysis suggested that B7-H3 signal remained associated with the CD3-positive population, in particular under 2x conditions, consistent with ongoing killing in which CAR-T cells retain target antigen on the membrane during active cytotoxic engagement. It is therefore possible that cytotoxicity under these alternative labelling conditions is not impaired but merely delayed. Extending the co-culture

period to 5 days could be explored to verify whether killing eventually reaches the levels observed under the standard labelling protocol.

3.5.1 Assessment of ^{19}F Labeling Stability over Time

During the cytotoxicity experiment assessment, flow cytometry was also used to evaluate Rhodamine-B fluorescence in live CAR-T cells gated within the CAR-T morphological region. After 3 days of co-culture, in the 1x (6h) condition, the histogram showed a partially reduction in fluorescence intensity, with a leftward shift towards negative control decades. To verify that this decrease was not attributable to nanoparticle exocytosis into the culture medium, complementary quantitative ^{19}F-NMR analyses were performed on both the cellular pellet and the retained supernatant, following the protocol described in Section 2.3.5 (Figure 3.22).

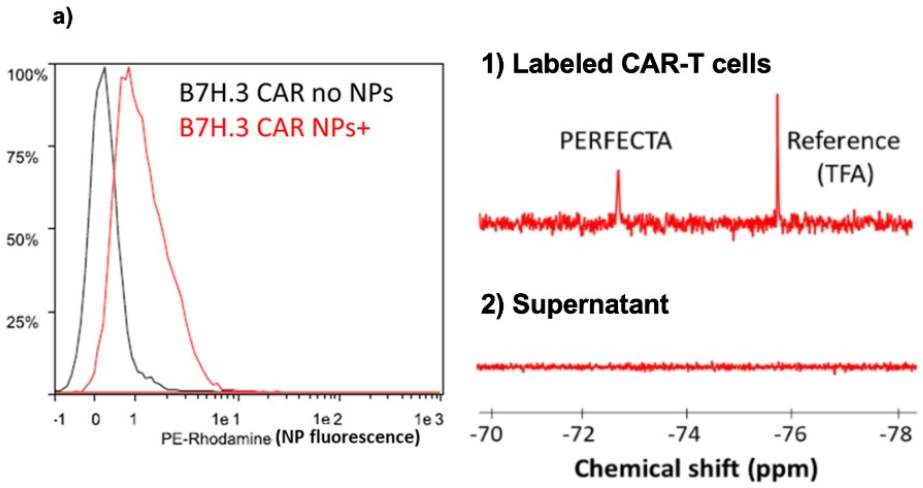

Figure 3.22: Assessment of Rhodamine-B fluorescence and intracellular ^{19}F retention in labelled CAR-T cells after 3 days of co-culture. **a)** flow cytometry histogram of Rhodamine-B fluorescence (PE channel): unlabeled cells (black) and labeled cells (red). **Right:** quantitative ^{19}F-NMR spectra of the cellular pellet (**1**) and supernatant (**2**).

As can be observed from the ^{19}F-NMR spectrum, the PERFECTA signal remains detectable in the cellular pellet ($\delta \approx -72.8\,\text{ppm}$, 8.41×10^{10} ^{19}F/cell in 1.76×10^5 cells), whereas no fluorine signal is observed in the supernatant, suggesting that the fluorescence decrease is unlikely to arise from nanoparticle exocytosis. A more plausible explanation is the progressive dilution of the intracellular fluorine payload and, consequently, of the Rhodamine-B fluorescence readout, among daughter CAR-T cells generated during co-culture. Indeed, CAR-T effectors must proliferate to sustain cytotoxic killing, and this expansion was confirmed by a positive net increase in the CAR-T population over the 3-day assay. The proliferative gain was quantified as

$$\Delta N_{\text{CAR-T}} = N_{\text{CAR-T,end}} - N_{\text{CAR-T,start}} = 61 \times 10^3 \text{ cells}, \tag{3.2}$$

where $N_{\mathrm{CAR-T,start}}$ is the number of labelled CAR-T cells seeded at the beginning of co-culture and $N_{\mathrm{CAR-T,end}}$ is the number of CAR-T cells recovered at the end of the 3-day incubation.

Fluorescence signal reduction was subsequently assessed under the alternative labelling conditions described above (Figure 3.23).

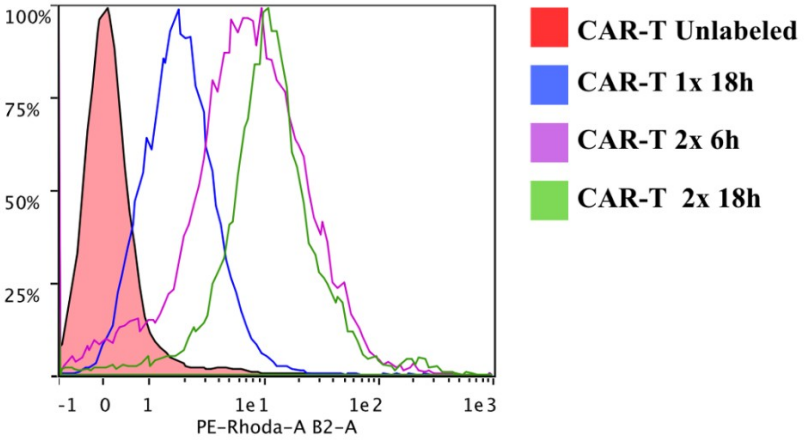

Figure 3.23: Rhodamine-B fluorescence histograms (PE channel) of live CAR-T cells after 3 days of co-culture under alternative labelling protocols: unlabelled negative control (red); CAR-T labelled overnight (18 h) at standard fluorine concentration (1×, blue); CAR-T labelled for 6 h at doubled fluorine concentration (2×, purple); CAR-T labelled overnight (18 h) at doubled fluorine concentration (2×, green).

As can be seen, fluorescence signal reduction was lower for the both doubled fluorine concentration (2×) than for the standard fluorine concentration (1×) overnight, within the same 3 days monitoring period. This further supports increased nanoparticle internalization under the doubled fluorine concentration (2×) conditions. Accordingly, fluorescence signal reduction over the same 3 day monitoring period appeared less pronounced; however, this likely reflects a larger initial intracellular payload available for dilution among proliferating daughter cells.

3.6 Critical Discussion and Methodological Limits

The progressive optimization of the *ex vivo* labelling protocol identified the standard fluorine concentration 3.13×10^{19} ^{19}F/ml with overnight incubation (18 h) for 3.33×10^{6} anti B7-H3 CAR-T cells, as the most balanced condition among those tested. This condition achieved a detectable ^{19}F-MRI signal (Figure 3.14), an intracellular mean loading of $2.06 \times 10^{12} \pm 8.06 \times 10^{10}$ ^{19}F/cell, and preserved killing activity (effector to target ratio of 4.5), while maintaining $> 65\%$ viability. This condition therefore represents the best compromise between labelling efficiency, cellular viability, and retained anti-tumour function.

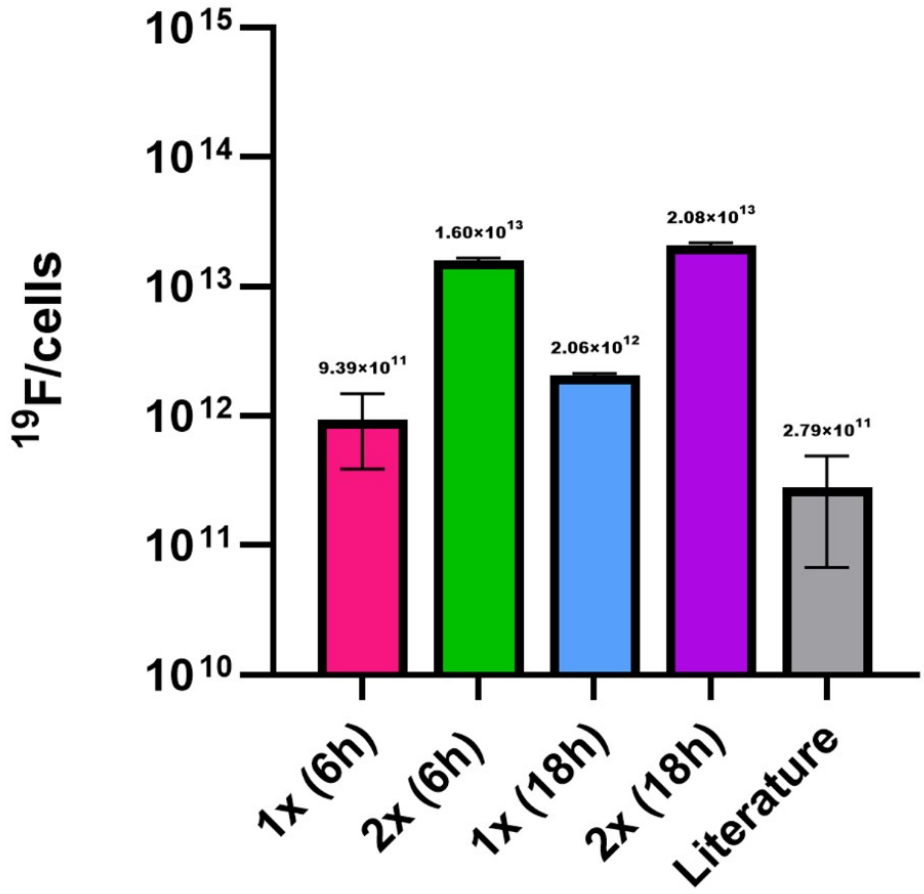

Figure 3.24: Mean intracellular ^{19}F loading per cell across the four labelling conditions tested in this work and a literature reference value (mean ± SD; ^{19}F/cell). **1× (6 h):** $9.39 \times 10^{11} \pm 5.5 \times 10^{11}$ ^{19}F/cell; **2× (6 h):** $1.66 \times 10^{13} \pm 6.51 \times 10^{11}$ ^{19}F/cell; **1× (18 h):** $2.06 \times 10^{12} \pm 8.06 \times 10^{10}$ ^{19}F/cell; **2× (18 h):** $2.08 \times 10^{13} \pm 8.13 \times 10^{11}$ ^{19}F/cell; **Literature:** $2.79 \times 10^{11} \pm 2.11 \times 10^{11}$ ^{19}F/cell.

As summarized in Figure 3.24, all four labelling protocols tested in this work exceeded the ^{19}F loading per CAR-T cell reported in the literature, whose reference value was calculated as the mean ± standard deviation of the loading values reported across published studies [47, 92]. Relative to this benchmark, the standard 6 h condition (1×) already provided approximately a 3.4 fold increase, whereas the optimized 1× (18 h) protocol reached roughly 4.3 fold higher loading. Under the higher loading conditions (2×, 6 h and 2×, 18 h), intracellular fluorine content increased by approximately 37 and 68 fold, respectively, reaching $\sim 10^{13}$ ^{19}F/cell. Of note, fluorine loading values in the same order of magnitude of those obtained here with the 1× (18 h) protocol, have previously been reported using nanoparticle formulations incorporating cell-penetrating peptides, reaching $1.23 \pm 0.85 \times 10^{12}$ ^{19}F/cell [98]. In this context, achieving comparable or higher labelling efficiency without the need for a cell-penetrating peptide represents an important advantage, as it reduces formulation complexity and may

limit peptide-associated effects, including membrane perturbation, cytotoxicity, immunogenicity, or additional variability in cell handling. These values are comparable in order of magnitude to those historically achieved in phagocytic cell lines, such as the murine microglial BV-2 line, which after 4 h of incubation with PERFECTA@PLGA nanoparticles reached approximately 5.8×10^{13} ^{19}F/cell [67]. This is the translational relevant point of the study, because CAR-T lymphocytes are non phagocytic effector cells, and are characterized by a comparatively reduced cytoplasmic compartment relative to phagocytic cells, for which efficient *ex vivo* loading has long been considered challenging [45, 57]. It is also important to note that, in this work, higher labelling levels were achieved even after applying a purification protocol that removes free nanoparticles or those weakly adhered to the cell surface, which could otherwise contaminate the measured signal. In this way, the quantified signal can be directly attributed to the intracellular fluorine load. This improvement is attributed primarily to PERFECTA, whose 36 magnetically equivalent ^{19}F nuclei contribute coherently to a single intense NMR/MRI resonance, and to its encapsulation within NaC stabilized PLGA nanoparticles optimized for *ex vivo* uptake [67, 66]. In contrast, PFPE and related PFC tracers used in literature labelling studies typically rely on emulsions with lower effective fluorine payload per particle and more complex spectral signatures, which limits both uptake efficiency and quantitative readout in non phagocytic lymphocytes [92].

Taken together, the results obtained across the physicochemical, biological, and imaging considerations form a coherent translational workflow. Colloidal stability and protein corona formation in CAR-T-conditioned medium (Figures 3.4) confirmed that NaC–PERFECTA@PLGA nanoparticles retain structural integrity during exposure to serum supplemented culture fluids, while undergoing the spatial reorganization of the adsorbed protein layer. This behaviour is relevant because labelling is performed in a biological medium and because corona composition can modulate uptake by non phagocytic lymphocytes. Post-labelling purification was then optimized systematically, comparing Ficoll-Paque and Percoll gradients, showing that Percoll 70/30% combined with EDTA/BSA-containing Staining Buffer provided the most balanced recovery of labelled CAR-T cells while depleting free and surface associated nanoparticles (Figure 3.9; Table 3.1), a prerequisite for attributing the downstream ^{19}F signal predominantly to intracellular cargo. Functional readouts demonstrated that labelled effectors retained cytotoxic activity against U-87 target cells, in particular in the optimized condition, and co-culture experiments further indicated that the apparent reduction in Rhodamine-B fluorescence over three days was accompanied by retention of ^{19}F atoms in the cellular pellet rather than by nanoparticle release into the supernatant (Figure 3.22), probably caused by the dilution of the cargo among proliferating daughter cells during active killing. Complementary Raman imaging supported intracellular localization of PERFECTA within labelled CAR-T cells at subcellular resolution (Figure 3.18), reinforcing

the multimodal rationale of combining bulk ^{19}F-MRI quantification with chemical subspatial mapping of the same contrast agent.

The comparison across labelling conditions also clarifies why overnight incubation at the standard fluorine concentration (1×, 18 h) emerged as the preferred protocol, despite the substantially higher intracellular loads achieved under doubled concentrations. Although the 2× conditions delivered up to two orders of ^{19}F magnitude more per cell, they were associated with delayed cytotoxic function (Figures 3.21). By contrast, the 1× (18 h) protocol preserved effector activity while crossing the ^{19}F-MRI detection threshold. Notably, the initial 1× (6 h) condition already exceeded published CAR-T loading benchmarks by NMR yet remained invisible in MRI, whereas overnight labelling at the same nanoparticle concentration produced a detectable image with only a modest increase in mean loading. This pattern indicates that successful cell tracking will depend on the interplay between fluorine content per cell, labelling yield after purification, the spatial distribution of labelled cells in 1 or 2 slices at the time of MRI acquisition, retained killing function and not only on intracellular loading, while manteining efficient and clinically translatable manufacturing workflow.

Viewed against the rationale developed in the Introduction, this work addresses the first link in the chain required for non-invasive monitoring of adoptive cell therapy in glioblastoma: it establishes that human anti-B7-H3 CAR-T cells can be labelled *ex vivo* with superfluorinated PLGA nanoparticles, purified to enrich truly internalized cargo, quantified by complementary ^{19}F-NMR and ^{19}F-MRI readouts, and functionally validated without loss of cytotoxic activity. Bridging the historical sensitivity gap in ^{19}F-MRI in non-phagocytic therapeutic lymphocytes is therefore the principal conceptual advance of the thesis and a necessary step toward biodistribution imaging in solid-tumour immunotherapy.

Methodological limitations. Despite the encouraging labelling performance, several limitations should be acknowledged. **First**, although killing was preserved under 1× (18 h) labelling, a slight attenuation of cytotoxic activity was observed at the 3 day co-culture endpoint compared with the unlabelled CAR-T control (effector to target ratio of 4.5 *versus* 5.18; Figure 3.21). Flow cytometry further suggested that cytotoxic engagement may be delayed rather than abolished under alternative labelling conditions; extending the observation window to 5 days of co-culture could clarify whether effector function recovers after an initial lag phase. **Second**, structurally important limitation concerns the ^{19}F-MRI readout itself. Under the initial standard protocol (1×, 6 h), intracellular fluorine was quantifiable by ^{19}F-NMR yet remained below the MRI detection threshold, whereas overnight labelling at the same fluorine concentration (1×, 18 h) yielded a clearly visible signal with only a modest increase in mean loading. This discrepancy indicates that detectability is governed not only by the

number of fluorine atoms per cell, but also by the number of labelled cells recovered after purification and by their spatial compaction into a dense pellet confined to one or two imaging slices. In the present work, the strongest imaging performance was therefore obtained under conditions that concentrate fluorine into a small pellet volume within an agarose phantom. Accordingly, this thesis demonstrates the feasibility of efficient *ex vivo* CAR-T labelling and of quantitative ^{19}F detection at the cellular level, but not yet the feasibility of clinical imaging of sparsely distributed therapeutic lymphocytes within the brain tumor area. Translation to *in vivo* biodistribution would introduce variables that remain untested here, including progressive signal dilution upon CAR-T proliferation and potential ^{19}F signal arising from free PERFECTA released after PLGA matrix degradation. **Third**, functional validation was likewise restricted to a simplified tumour model. Cytotoxicity was assessed in co-culture with adherent U-87 MG cells rather than with glioblastoma neurospheres or patient derived models discussed in the Introduction. This two-dimensional monolayer system lacks the three-dimensional architecture and immunosuppressive microenvironment of glioblastoma *in vivo*. Preserved killing under these permissive conditions should therefore be interpreted as proof of retained effector function after labelling and not specifically as evidence of therapeutic efficacy in the clinical tumour setting. **Fourth**, from a manufacturing perspective, post-labelling purification on Percoll 70/30% recovered approximately 52% of labelled CAR-T cells (Table 3.1), meaning that nearly half of the cellular product is lost before reinfusion or imaging. This yield has direct implications for GMP scalability. **Fifth**, Long-term cytocompatibility should be further addressed in future studies. In particular, PLGA biodegradation could be evaluated over time, potentially using Raman microscopy to monitor residual polymeric material within labelled cells. In addition, the persistence and clearance of encapsulated PERFECTA and Rhodamine-B-containing components should be investigated to better define the intracellular fate of the labelling platform. This would help assess whether residual carrier material may affect CAR-T cell phenotype, including differentiation state, memory phenotype, exhaustion markers, or potential immunogenicity.

Chapter 4

Conclusions and Future Perspectives

Future perspectives. Several lines of investigation could further strengthen and extend the platform developed in this thesis. Intermediate labelling parameters, for example a 1.5× fluorine concentration and parallel incubation times of 12 h and 18 h, should be explored to map more finely the trade-off between uptake, viability, and effector function, while uptake kinetics should be characterized by flow cytometry at multiple time points during labelling to identify the incubation window that maximizes intracellular PERFECTA loading without exceeding the viability threshold. The labelling strategy should be extended beyond the anti-B7-H3 CAR-T product characterized here to dual-target B7zCS CAR-T cells directed against both B7-H3 and CSPG4, a construct under active development for glioblastoma that may offer improved coverage of residual disease [37, 16]. Parallel application to other cellular products would further broaden the impact of the platform across personalized adoptive therapies [93, 94]. A complementary ^{19}F-MRI sensitivity study could be performed by progressively reducing the number of cells labelled under the most performant protocol identified in this work, namely 1× (18 h). Such a titolational experiment would allow estimation of the minimum number of labelled cells required for reliable detection and would help define the practical detection limit of the methodology in preparation for *in vivo* biodistribution studies.

At the functional level, co-culture assays should be prolonged to 5 days under the current 1× (18 h) labelling protocol, to determine whether any initial delay in CAR-T killing reflects transient functional impairment, followed by recovery, as suggested by the flow-cytometry profiles. The effector to target ratio should also be revisited systematically, increasing the proportion of tumour cells to a 3:1 target to effector configuration, which would better approximate the burden of residual glioblastoma cells expected after surgical resection. Complementary Raman imaging of co-cultured samples would clarify the fate of the PLGA carrier and of PERFECTA itself, during time windows, and answer the questions whether the probe remains within CAR-T cells, relocalizes subcellularly, or is transferred to tumour targets during killing activity.

After *in vitro* refinement along these axes, the platform should be advanced to *in vivo* biodistribution and persistence studies, building on the quantitative ^{19}F-MRI readout already established at the cellular level.

From a nanoparticle perspective, an important next step is to pre-incubate NaC–PERFECTA@PLGA nanoparticles in patient conditioned medium prior to contact with therapeutic cells, thereby allowing controlled pre-formation of the protein corona before labelling and infusion to scale the process at clinical level. On the manufacturing side, efforts should focus on improving large scale production and cell recovery after purification, so that fluorinated labelling can be integrated into personalized, patient-specific ACT manufacturing in the vein-to-vein chain [23].

Conclusions. The ultimate aim of this work is to enable non-invasive, quantitative monitoring of adoptive cellular therapies in glioblastoma patients who have undergone maximal safe tumour resection and are candidates for intracatheter reinfusion of engineered lymphocytes into the surgical cavity. In this clinical scenario, CAR-T cells are delivered locoregional, typically via intracatheter administration into the resection area, to target residual infiltrative tumor cells that cannot be removed surgically and constitutes the principal source of local recurrence. Without molecular imaging, clinicians cannot determine whether therapeutic failure reflects loss of effector function, insufficient persistence, or inadequate distribution within the tumour compartment. The rationale of this thesis is therefore to optimize *ex vivo* labelling of ACT products with superfluorinated nanoparticles so that, once reinfused, their fate can be followed longitudinally by ^{19}F-MRI and interpreted in biological rather than exclusively clinical terms.

Against this background, the present study demonstrates that the first essential step of that translational chain is feasible. Superfluorinated PLGA nanoparticles encapsulating PERFECTA were synthesized, scaled to large production and cell-culture compatible volumes, and shown to remain colloidally stable in CAR-T conditioned medium. Human anti-B7-H3 CAR-T cells could be labelled *ex vivo*, purified to obtained a pure intracellular fluorine signal, and analysed by complementary ^{19}F-NMR, ^{19}F-MRI, flow cytometry, and Raman imaging while retaining cytotoxic activity against glioblastoma targets. Overnight labelling at the standard fluorine concentration (1×, 18 h) emerged as the best operational compromise, combining MRI detectability, intracellular loading approximately fourfold above published CAR-T benchmarks [92], and preserved effector function. So, the study supplies a methodological foundation for addressing the fate of reinfused effectors in the post-resection setting. More broadly, the ^{19}F-based labelling platform developed in this thesis could be extended to other therapeutic cell products used in cellular therapies across diverse diseases, including stem and progenitor cells, dendritic cells, and additional lymphocyte subsets.

The next stage is to connect these endpoints to *in vivo* biodistribution in post-resection glioblastoma animal models and, ultimately, to patient, monitoring them during locoregional ACT. If successfully translated, NaC–PERFECTA@PLGA labelling could provide clinicians with a non-invasive tool to visualize the distribution and persistence of therapeutic immune cells in the resection cavity, supporting a more personalized medicine in immunotherapy in glioblastoma.

Bibliography

[1] Jr. Freitas, Robert A. What is nanomedicine? *Nanomedicine*, 1(1):2–9, 2005.

[2] Suphiya Parveen, Ranjita Misra, and Sanjeeb K. Sahoo. Nanoparticles: a boon to drug delivery, therapeutics, diagnostics and imaging. *Nanomedicine*, 8(2):147–166, 2012.

[3] Monica Zoppè. Towards a perceptive understanding of size in cellular biology. *Nature Methods*, 14(7):662–665, 2017.

[4] Xiangjun Han, Ke Xu, Olena Taratula, and Khashayar Farsad. Applications of nanoparticles in biomedical imaging. *Nanoscale*, 11(3):799–819, 2019.

[5] David N. Louis, Arie Perry, Pieter Wesseling, Daniel J. Brat, Ian A. Cree, Dominique Figarella-Branger, Cynthia Hawkins, Ho-Keung Ng, Stefan M. Pfister, Guido Reifenberger, Riccardo Soffietti, Andreas von Deimling, and David W. Ellison. The 2021 who classification of tumors of the central nervous system: a summary. *Neuro-Oncology*, 23(8):1231–1251, 2021.

[6] Patrick Y. Wen, Michael Weller, Eudocia Q. Lee, Brian M. Alexander, Jill S. Barnholtz-Sloan, Floris P. Barthel, Tracy T. Batchelor, E. Antonio Chiocca, et al. Glioblastoma in adults: a society for neuro-oncology (sno) and european society of neuro-oncology (eano) consensus review on current management and future directions. *Neuro-Oncology*, 22(8):1073–1113, 2020.

[7] Quinn T. Ostrom, Nirav Patil, Gino Cioffi, Kristin Waite, Carol Kruchko, and Jill S. Barnholtz-Sloan. CBTRUS statistical report: Primary brain and other central nervous system tumors diagnosed in the united states in 2013–2017. *Neuro-Oncology*, 22(12 Suppl 2):iv1–iv96, 2020. Erratum: Neuro Oncol. 2022;24(7):1214. doi: 10.1093/neuonc/noaa269.

[8] Ji-Yong Sung and Kihwan Hwang. Glioblastoma: epidemiology, molecular pathogenesis, diagnosis, management, and therapeutic resistance. *Molecular Biomedicine*, 7(1):63, 2026.

[9] Roger Stupp, Monika E. Hegi, Warren P. Mason, Martin J. van den Bent, Martin J. B. Taphoorn, Roger C. Janzer, Samuel K. Ludwin, Anouk Allgeier, Barbara Fisher, Karl Belanger, Peter Hau, Alba A. Brandes, Johanna Gijtenbeek, Christine Marosi, Charles J. Vecht, Karima Mokhtari, Pieter Wesseling, Elizabeth Eisenhauer, Thierry Gorlia, Michael Weller, Denis Lacombe, J. Gregory Cairncross, and Rene-Olivier Mirimanoff. Effects of radiotherapy with concomitant and adjuvant temozolomide versus radiotherapy alone on survival in glioblastoma in a randomised phase iii study: 5-year analysis of the eortc-ncic trial. *The Lancet Oncology*, 10(5):459–466, 2009.

[10] Roger Stupp, Sophie Taillibert, Andrew Kanner, William Read, David Steinberg, Benoit Lhermitte, Steven Toms, Ahmed Idbaih, Manmeet S. Ahluwalia, Karen Fink, et al. Effect of tumor-treating fields plus maintenance temozolomide vs maintenance temozolomide alone on survival in patients with glioblastoma: A randomized clinical trial. *JAMA*, 318(23):2306–2316, 2017.

[11] Quinn T. Ostrom, Luc Bauchet, Faith G. Davis, Isabelle Deltour, James L. Fisher, Chelsea E. Langer, Melike Pekmezci, Judith A. Schwartzbaum, Michelle C. Turner, Kyle M. Walsh, Margaret R. Wrensch, and Jill S. Barnholtz-Sloan. The epidemiology of glioma in adults: a "state of the science" review. *Neuro-Oncology*, 16(7):896–913, 2014.

[12] Daniela F. Quail and Johanna A. Joyce. The microenvironmental landscape of brain tumors. *Cancer Cell*, 31(3):326–341, 2017.

[13] Chao Lin, Ning Wang, and Chengyan Xu. Glioma-associated microglia/macrophages (gams) in glioblastoma: immune function in the tumor microenvironment and implications for immunotherapy. *Frontiers in Immunology*, 14:1123853, 2023.

[14] Michael Weller, Martin van den Bent, Matthias Preusser, Emilie Le Rhun, Jörg C. Tonn, Giuseppe Minniti, Martin Bendszus, Carmen Balana, Olivier Chinot, Linda Dirven, Pim French, Monika Hegi, Asgeir S. Jakola, Michael Platten, Patrick Roth, Roberta Rudà, et al. Eano guidelines on the diagnosis and treatment of diffuse gliomas of adulthood. *Nature Reviews Clinical Oncology*, 19(5):357–358, 2022.

[15] Xin Tang, Shasha Zhao, Yang Zhang, Yuelong Wang, Zongliang Zhang, Meijia Yang, Yanyu Zhu, Guanjie Zhang, Gang Guo, Aiping Tong, and Liangxue Zhou. B7-h3 as a novel car-t therapeutic target for glioblastoma. *Molecular Therapy Oncolytics*, 14:279–287, 2019.

[16] D. Nehama, N. Di Ianni, S. Musio, H. Du, M. Patané, B. Pollo, G. Finocchiaro, J. J. H. Park, D. E. Dunn, D. S. Edwards, J. S. Damrauer, H. Hudson, S. R. Floyd, S. Ferrone, B. Savoldo, S. Pellegatta, and G. Dotti. B7-h3-redirected chimeric antigen receptor t cells target glioblastoma and neurospheres. *EBioMedicine*, 47:33–43, 2019.

[17] Davor Babić, Ivana Jovčevska, and Alja Zottel. B7-h3 in glioblastoma and beyond: significance and therapeutic strategies. *Frontiers in Immunology*, 15:1495283, 2024.

[18] Steven A. Rosenberg and Nicholas P. Restifo. Adoptive cell transfer as personalized immunotherapy for human cancer. *Science*, 348(6230):62–68, 2015.

[19] Sarwish Rafiq, Christopher S. Hackett, and Renier J. Brentjens. Engineering strategies to overcome the current roadblocks in car t cell therapy. *Nature Reviews Clinical Oncology*, 17(3):147–167, 2020.

[20] Francisco Garrido, Natalia Aptsiauri, Elisabeth M. Doorduijn, Ángel M. García Lora, and Thorbald van Hall. The urgent need to recover mhc class i in cancers for effective immunotherapy. *Current Opinion in Immunology*, 39:44–51, 2016.

[21] Carl H. June and Michel Sadelain. Chimeric antigen receptor therapy. *The New England Journal of Medicine*, 379(1):64–73, 2018.

[22] Robert C. Sterner and Rosalie M. Sterner. Car-t cell therapy: current limitations and potential strategies. *Blood Cancer Journal*, 11(4):69, 2021.

[23] Jessica Hartmann, Martina Schüßler-Lenz, Attilio Bondanza, and Christian J. Buchholz. Clinical development of car t cells—challenges and opportunities in translating innovative treatment concepts. *EMBO Molecular Medicine*, 9(9):1183–1197, 2017.

[24] Jayapriya Jayaraman, Michael P. Mellody, Andrew J. Hou, Ruchi P. Desai, Audrey W. Fung, An Huynh Thuy Pham, Yvonne Y. Chen, and Weian Zhao. Car-t design: Elements and their synergistic function. *eBioMedicine*, 58:102931, 2020.

[25] Sophie Depil, Philippe Duchateau, Stephan A. Grupp, Ghulam Mufti, and Laurence Poirot. 'Off-the-shelf' allogeneic car t cells: development and challenges. *Nature Reviews Drug Discovery*, 19(3):185–199, 2020.

[26] Yang Xu, Ming Zhang, Carlos A. Ramos, April Durett, Enli Liu, Olga Dakhova, Hao Liu, Chad J. Creighton, Adrian P. Gee, Helen E. Heslop, Cliona M. Rooney, Barbara Savoldo, and Gianpietro Dotti. Closely related t-memory stem cells correlate with in vivo expansion of car.cd19-t cells and are preserved by il-7 and il-15. *Blood*, 123(24):3750–3759, 2014.

[27] James N. Kochenderfer, Markus E. Dudley, Sadik H. Kassim, Robert P. T. Somerville, Robert O. Carpenter, Maryalice Stetler-Stevenson, et al. Chemotherapy-refractory diffuse large b-cell lymphoma and indolent b-cell malignancies can be effectively treated with autologous t cells expressing an anti-cd19 chimeric antigen receptor. *Journal of Clinical Oncology*, 33(6):540–549, 2015.

[28] David L. Porter, Bruce L. Levine, Michael Kalos, Adam Bagg, and Carl H. June. Chimeric antigen receptor–modified t cells in chronic lymphoid leukemia. *The New England Journal of Medicine*, 365(8):725–733, 2011.

[29] Renier J. Brentjens, Marco L. Davila, Isabelle Riviere, Jae Park, Xiuyan Wang, Lindsay G. Cowell, Shirley Bartido, Jonathan Stefanski, Clare Taylor, Malgorzata Olszewska, et al. CD19-targeted t cells rapidly induce molecular remissions in adults with chemotherapy-refractory acute lymphoblastic leukemia. *Science Translational Medicine*, 5(177):177ra38, 2013.

[30] Jennifer N. Brudno and James N. Kochenderfer. Chimeric antigen receptor t-cell therapies for lymphoma. *Nature Reviews Clinical Oncology*, 15(1):31–46, 2018.

[31] Sattva S. Neelapu, Frederick L. Locke, Nancy L. Bartlett, Lazaros J. Lekakis, David B. Miklos, Caron A. Jacobson, Igor Braunschweig, Olalekan O. Oluwole, Tanya Siddiqi, Yi Lin, et al. Axicabtagene ciloleucel CAR t-cell therapy in refractory large b-cell lymphoma. *The New England Journal of Medicine*, 377(26):2531–2544, 2017.

[32] Yang Zhao, Jiangqing Chen, Massimo Andreatta, Bing Feng, Yu-Qing Xie, Mathias Wenes, Yi Wang, Min Gao, Xiaomeng Hu, Pedro Romero, et al. IL-10-expressing CAR t cells resist dysfunction and mediate durable clearance of solid tumors and metastases. *Nature Biotechnology*, 42(11):1693–1704, 2024.

[33] Paulo Martins, Rochelle C. J. D'Souza, Niclas Skarne, Lea Lekieffre, Shane Horsefield, Madusha Ranjankumar, Xiang Li, Thuy T. Le, et al. EphA3 CAR t cells are effective against glioblastoma in preclinical models. *Journal for ImmunoTherapy of Cancer*, 12(8):e009403, 2024.

[34] Stephen J. Bagley, Arati S. Desai, Joseph A. Fraietta, Dana Silverbush, Daniel Chafamo, Nelson F. Freeburg, Gayathri Konanur Gopikrishna, Andrew J. Rech, Ali Nabavizadeh, Linda J. Bagley, et al. Intracerebroventricular bivalent CAR t cells targeting EGFR and IL-13Ralpha2 in recurrent glioblastoma: a phase 1 trial. *Nature Medicine*, 31(8):2778–2787, 2025.

[35] Changsong Qi, Chang Liu, Jifang Gong, Dan Liu, Xicheng Wang, Panpan Zhang, Yanru Qin, Sai Ge, et al. Claudin18.2-specific CAR t cells in gastrointestinal cancers: phase 1 trial final results. *Nature Medicine*, 30(8):2224–2234, 2024.

[36] Gaetano Finocchiaro and Serena Pellegatta. NG2/CSPG4 in glioblastoma: about flexibility. *Neuro-Oncology*, 21(6):697–698, 2019.

[37] Serena Pellegatta, Barbara Savoldo, Natalia Di Ianni, Cristina Corbetta, Yuhui Chen, Monica Patanè, Chuang Sun, Bianca Pollo, Soldano Ferrone, Francesco DiMeco, Gaetano Finocchiaro, and Gianpietro Dotti. Constitutive and TNFα-inducible expression of chondroitin sulfate proteoglycan 4 in glioblastoma and neurospheres: Implications for CAR-T cell therapy. *Science Translational Medicine*, 10(430):eaao2731, 2018.

[38] Filippo Galli, Michela Varani, Chiara Lauri, Guido Gentiloni Silveri, Livia Onofrio, and Alberto Signore. Immune cell labelling and tracking: implications for adoptive cell transfer therapies. *EJNMMI Radiopharmacy and Chemistry*, 6(1):7, 2021.

[39] Peter J. Gawne, Francis Man, Philip J. Blower, and Rafael T. M. de Rosales. Direct cell radiolabeling for in vivo cell tracking with PET and SPECT imaging. *Chemical Reviews*, 122(11):10266–10318, 2022.

[40] Michelle L. James and Sanjiv S. Gambhir. A molecular imaging primer: Modalities, imaging agents, and applications. *Physiological Reviews*, 92(2):897–965, 2012.

[41] Dale L. Bailey, David W. Townsend, Peter E. Valk, and Michael Maisey, editors. *Positron Emission Tomography: Basic Sciences*. Springer, London, 2 edition, 2005.

[42] Alberto Signore, François Jamar, Ora Israel, John Buscombe, Joan Martin-Comin, and Eleonora Lazzeri. Clinical indications, image acquisition and data interpretation for white blood cells and anti-granulocyte monoclonal antibody scintigraphy: An EANM procedural guideline. *European Journal of Nuclear Medicine and Molecular Imaging*, 45(10):1816–1831, 2018.

[43] Michael D. Farwell, Raymond F. Gamache, Hasan Babazada, Matthew D. Hellmann, James J. Harding, Ron Korn, Alessandro Mascioni, William Le, Ian Wilson, Michael S. Gordon, Anna M. Wu, Gary A. Ulaner, Jedd D. Wolchok, Michael A. Postow, and Neeta Pandit-Taskar. CD8-targeted PET imaging of tumor-infiltrating t cells in patients with cancer: A phase I first-in-humans study of ^{89}Zr-df-iab22m2c, a radiolabeled anti-CD8 minibody. *Journal of Nuclear Medicine*, 63(5):720–726, 2022.

[44] Francis Man, Peter J. Gawne, and Rafael T. M. de Rosales. Nuclear imaging of liposomal drug delivery systems: A critical review of radiolabelling methods and applications in nanomedicine. *Advanced Drug Delivery Reviews*, 143:134–160, 2019.

[45] Eric T. Ahrens and Jeff W. M. Bulte. Tracking immune cells in vivo using magnetic resonance imaging. *Nature Reviews Immunology*, 13(10):755–763, 2013.

[46] Jesús Ruiz-Cabello, Brad P. Barnett, Paul A. Bottomley, and Jeff W. M. Bulte. Fluorine (19f) MRS and MRI in biomedicine. *NMR in Biomedicine*, 24(2):114–129, 2011.

[47] Vincent P. Dubois, Oliver C. Sehl, P. Jonathan Foster, and John A. Ronald. Visualizing CAR-T cell immunotherapy using 3 tesla fluorine-19 MRI. *Molecular Imaging and Biology*, 24(2):298–308, 2022.

[48] Robert W. Brown, Y.-Ch. Norman Cheng, E. Mark Haacke, Michael R. Thompson, and Ramesh Venkatesan. *Magnetic Resonance Imaging: Physical Principles and Sequence Design*. Wiley-Blackwell, Hoboken, NJ, 2 edition, 2014.

[49] Saioa Alzola-Aldamizetxebarria, Laura Fernández-Méndez, Daniel Padró, Jesús Ruiz-Cabello, and Pedro Ramos-Cabrer. A comprehensive introduction to magnetic resonance imaging relaxometry and contrast agents. *ACS Omega*, 7(42):36905–36917, 2022.

[50] G. N. Holland, P. A. Bottomley, and W. S. Hinshaw. ^{19}F magnetic resonance imaging. *Journal of Magnetic Resonance*, 28(1):133–136, 1977.

[51] Michael A. Ibrahim, Bita Hazhirkarzar, and Arthur B. Dublin. Gadolinium magnetic resonance imaging. StatPearls, 2023. Updated 2023 Jul 3; Bookshelf ID NBK482487.

[52] Houshang Amiri, Mangala Srinivas, Andor Veltien, Mark J. van Uden, I. Jolanda M. de Vries, and Arend Heerschap. Cell tracking using 19F magnetic resonance imaging: Technical aspects and challenges towards clinical applications. *European Radiology*, 25(3):726–735, 2015.

[53] Peter Caravan. Strategies for increasing the sensitivity of gadolinium based MRI contrast agents. *Chemical Society Reviews*, 35(6):512–523, 2006.

[54] T. L. Watson, U. Estenberg, and M. Kristoffersen Wiberg. Clinical experience of the use of gadolinium contrast agents for T1-weighted 3D high-resolution neurological imaging, 2007.

[55] Y.X. Wang, S. M. Hussain, and G.P. Krestin. Superparamagnetic iron oxide contrast agents: physicochemical characteristics and applications in MR imaging. *European Radiology*, 11(11):2319–2331, 2001.

[56] Ralph Weissleder, Daniel D. Stark, Brian L. Engelstad, Bradley R. Bacon, Carolyn C. Compton, Daniel L. White, Paula Jacobs, and Jacky Lewis. Superparamagnetic iron oxide: pharmacokinetics and toxicity. *AJR American Journal of Roentgenology*, 152(1):167–173, 1989.

[57] Alvja Mali, Eric L. Kaijzel, Hildo J. Lamb, and Luis J. Cruz. 19F-nanoparticles: Platform for in vivo delivery of fluorinated biomaterials for 19F-MRI. *Journal of Controlled Release*, 338:870–889, 2021.

[58] Hao-Li Liu, Po-Hong Hsu, Po-Chun Chu, Yau-Yau Wai, Jin-Chung Chen, Chia-Rui Shen, Tzu-Chen Yen, and Jiun-Jie Wang. Magnetic resonance imaging enhanced by superparamagnetic iron oxide particles: Usefulness for distinguishing between focused ultrasound-induced blood–brain barrier disruption and brain hemorrhage. *Journal of Magnetic Resonance Imaging*, 29(1):31–38, 2009.

[59] Eric T. Ahrens and Jian Zhong. In vivo MRI cell tracking using perfluorocarbon probes and fluorine-19 detection. *NMR in Biomedicine*, 26(7):860–871, 2013.

[60] Mangala Srinivas, Arend Heerschap, Eric T. Ahrens, Carl G. Figdor, and I. Jolanda M. de Vries. ^{19}F MRI for quantitative in vivo cell tracking. *Trends in Biotechnology*, 28(7):363–370, 2010.

[61] K. C. Partlow, Junjie Chen, Jason A. Brant, Aaron M. Neubauer, Todd E. Meyerrose, Matthew H. Creer, Jan A. Nolta, Shelton D. Caruthers, Gregory M. Lanza, and Samuel A. Wickline. 19f magnetic resonance imaging for stem/progenitor cell tracking using multiple unique perfluorocarbon nanobeacons. *FASEB Journal*, 21(8):1647–1654, 2007.

[62] Cristina Chirizzi, Davide De Battista, Ilaria Tirotta, Pierangelo Metrangolo, Giancarlo Comi, Francesca Baldelli Bombelli, and Linda Chaabane. Multispectral MRI with dual fluorinated probes to track mononuclear cell activity in mice. *Radiology*, 291(2):351–357, 2019.

[63] Cristina Chirizzi, Carlo Morasso, Alessandro Aldo Caldarone, Matteo Tommasini, Fabio Corsi, Linda Chaabane, Renzo Vanna, Francesca Baldelli Bombelli, and Pierangelo Metrangolo. A bioorthogonal probe for multiscale imaging by ^{19}f-MRI and raman microscopy: From whole body to single cells. *Journal of the American Chemical Society*, 143(31):12253–12260, 2021.

[64] Ilaria Tirotta, Valentina Dichiarante, Claudia Pigliacelli, Gabriella Cavallo, Giancarlo Terraneo, Francesca Baldelli Bombelli, Pierangelo Metrangolo, and Giuseppe Resnati. ^{19}f magnetic resonance imaging (MRI): From design of materials to clinical applications. *Chemical Reviews*, 115(2):1106–1129, 2015.

[65] Alexa R. Heaton, Lawrence M. Lechuga, Montira Tangsangasaksri, Kai D. Ludwig, Sean B. Fain, and Sandro Mecozzi. A stable, highly concentrated fluorous nanoemulsion formulation for in vivo cancer imaging via ^{19}f-MRI. *NMR in Biomedicine*, 37(5):e5100, 2024.

[66] Ilaria Tirotta, Alfonso Mastropietro, Chiara Cordiglieri, Lara Gazzera, Fulvio Baggi, Giuseppe Baselli, Maria Grazia Bruzzone, Ileana Zucca, Gabriella Cavallo, Giancarlo Terraneo, Francesca Baldelli Bombelli, Pierangelo Metrangolo, and Giuseppe Resnati. A superfluorinated molecular probe for highly sensitive in vivo ^{19}f-MRI. *Journal of the American Chemical Society*, 136(24):8524–8527, 2014.

[67] Cristina Chirizzi, Lodovico Gatti, María Sancho-Albero, Victor Sebastian, Manuel Arruebo, Laura Uson, Giulia Neri, Jesús Santamaría, Pierangelo Metrangolo, Linda Chaabane, and Francesca Baldelli Bombelli. Optimization of superfluorinated PLGA nanoparticles for enhanced cell labelling and detection by ^{19}f-MRI. *Colloids and Surfaces B: Biointerfaces*, 220:112932, 2022.

[68] Giacomo Mandriota, Nicoletta Depalo, Elisabetta Fanizza, Marta Rosati, Cristina Chirizzi, Valentina Dichiarante, Rosario Oliva, Pompea Del Vecchio, Francesca Baldelli Bombelli, Maria Lucia Curri, Chiara Ingrosso, and Pierangelo Metrangolo. Encapsulation of PERFECTA fluorinated probe in a core–shell nanostructured lipid carrier for ^{19}f-MRI molecular imaging. *ACS Applied Nano Materials*, 9(8):3679–3688, 2026.

[69] Alexander H. J. Staal, Katrin Becker, Oya Tagit, N. Koen van Riessen, Olga Koshkina, Andor Veltien, Pascal Bouvain, Kimberley R. G. Cortenbach, Tom Scheenen, Ulrich Flögel, Sebastian Temme, and Mangala Srinivas. In vivo clearance of ^{19}f MRI imaging nanocarriers is strongly influenced by nanoparticle ultrastructure. *Biomaterials*, 261:120307, 2020.

[70] Lodovico Gatti, Cristina Chirizzi, Giulia Rotta, Pietro Milesi, María Sancho-Albero, Victor Sebastián, Anna Mondino, Jesús Santamaría, Pierangelo Metrangolo, Linda Chaabane, and Francesca Baldelli Bombelli. Pivotal role of the protein corona in the cell uptake of fluorinated nanoparticles with increased sensitivity for ^{19}f-MR imaging. *Nanoscale Advances*, 5(14):3749–3760, 2023.

[71] Bruce J. Berne and Robert Pecora. *Dynamic Light Scattering: With Applications to Chemistry, Biology, and Physics*. Dover Publications, Mineola, NY, 2000.

[72] Dennis E. Koppel. Analysis of macromolecular polydispersity in intensity correlation spectroscopy: The method of cumulants. *The Journal of Chemical Physics*, 57(11):4814–4820, 1972.

[73] Malvern Panalytical. Dynamic light scattering: An introduction in 30 minutes. Technical note TN101104, 2010. Principles of DLS, speckle pattern, cumulants analysis, and size distributions.

[74] Steven W. Provencher. CONTIN: A general purpose constrained regularization program for inverting noisy linear algebraic and integral equations. *Computer Physics Communications*, 27(3):229–242, 1982.

[75] Particle Metrix GmbH. Introduction to nanoparticle tracking analysis (NTA): Measurement principle of ZetaView. White paper, Particle Metrix GmbH, 2016. Principles of NTA, Brownian sizing, 90° ultra-microscopy detection, and hydrodynamic diameter in the 10–1000 nm range; PDF hosted by Analytik Ltd (UK distributor).

[76] Vasco Filipe, Andrea Hawe, and Wim Jiskoot. Critical evaluation of nanoparticle tracking analysis (NTA) by NanoSight for the measurement of nanoparticles and protein aggregates. *Pharmaceutical Research*, 27(5):796–810, 2010.

[77] Malvern Panalytical. NTA: Principles and methodology. White paper WP150312, Malvern Panalytical, 2015. Optical configuration, Brownian sizing, concentration measurement, and fluorescence NTA.

[78] Hans Saveyn, Bernard De Baets, Olivier Thas, Patrick Hole, Jeremy Smith, and Paul Van der Meeren. Accurate particle size distribution determination by nanoparticle tracking analysis based on 2-D Brownian dynamics simulation. *Journal of Colloid and Interface Science*, 352(2):593–600, 2010.

[79] Francesco Cellesi. Colloidal stability. Lecture slides, Nanomedicine and Pharmaceutical Innovation (058013), 2024. Academic year 2024/2025; DLVO theory, zeta potential, and stability criteria; (course material).

[80] Robert J. Hunter. *Zeta Potential in Colloid Science: Principles and Applications*. Academic Press, London, 1981.

[81] Boris V. Derjaguin and Lev D. Landau. Theory of the stability of strongly charged lyophobic sols and of the adhesion of strongly charged particles in solutions of electrolytes. *Acta Physicochimica*, 14:633–662, 1993.

[82] E. J. W. Verwey and J. Th. G. Overbeek. *Theory of the Stability of Lyophobic Colloids: The Interaction of Sol Particles Having an Electric Double Layer*. Elsevier, Amsterdam, 1948.

[83] Duncan J. Shaw. *Introduction to Colloid and Surface Chemistry*. Butterworth-Heinemann, Oxford, 4 edition, 1992.

[84] Malvern Panalytical. Zeta potential: An introduction in 30 minutes. Technical note MRK654-01, Malvern Panalytical, 2001. Electrical double layer, slipping plane, electrophoresis, and colloidal stability guidelines ($|\zeta| \gtrsim 30\,\mathrm{mV}$).

[85] Raffaella Lobello. Design and characterization of fluorinated nanoparticles for CAR-T cell labelling and ^{19}f MRI tracking in glioblastoma therapy. Tesi di laurea magistrale, Politecnico di Milano, 2026. Relatore: Baldelli Bombelli, Francesca; correlatori: Chirizzi, Cristina and Pellegatta, Serena. Academic year 2025/2026.

[86] B&W Tek. Theory of raman scattering. B&W Tek Spectroscopy Knowledge, 2026. Jablonski diagram of Rayleigh, Stokes, and anti-Stokes scattering (Figure R-4).

[87] Anna M. Nowakowska, Agnieszka Pieczara, Wojciech Korona, Alicja Borek-Dorosz, Adrianna Adamczyk, Piotr Dawiec, Paweł Leszczenko, Justyna Orleanska, Ewa Machalska, Barbara Orzechowska, Stanisława Orzechowska, Karol Brzozowski, Witold Krynicka, Katarzyna Majzner, Kamila Malek, and Malgorzata Baranska. The Raman map of the human cell. *Analytical Chemistry*, 97(30):16374–16382, 2025.

[88] Arne Bøyum. Separation of leukocytes from blood and bone marrow. *Scandinavian Journal of Clinical and Laboratory Investigation*, 21(Suppl. 97):77–89, 1968.

[89] Cytiva. Ficoll-paque plus. Product data sheet, Cytiva Life Sciences, 2024. Ficoll-Paque consists of Ficoll PM400 and sodium diatrizoate; density 1.077 g/mL for mononuclear cell isolation.

[90] Håkan Pertoft, Torvard C. Laurent, Torgny Låås, and Lennart Kågedal. Density gradients prepared from colloidal silica particles coated by polyvinylpyrrolidone (Percoll). *Analytical Biochemistry*, 88(1):271–282, 1978.

[91] Cytiva. Cell separation media: Methodology and applications. Handbook, Cytiva Life Sciences, 2024. Percoll: colloidal silica coated with polyvinylpyrrolidone; iso-osmotic gradients adjustable from 1.0 to 1.3 g/mL.

[92] F. Chapelin, S. Gao, Hideho Okada, et al. Fluorine-19 nuclear magnetic resonance of chimeric antigen receptor T cell biodistribution in murine cancer model. *Scientific Reports*, 7:17748, 2017.

[93] Martina Maffezzini, Silvia Musio, Natalia Di Ianni, Agnese Rumolo, Monica Patanè, Andrea Galluzzo, Irene Sambruni, Arianna Berlendis, Domenico Aquino, Giacomo Baso, Manuela Zingarelli, Manuel Facciolla, Luisa Maddaloni, Serena Pellegatta, et al. Polyclonal expansion of functional tumor-reactive lymphocytes infiltrating glioblastoma for personalized cell therapy. *Nature Communications*, 16:7279, 2025.

[94] Mark E. Dudley, John R. Wunderlich, James C. Yang, Richard M. Sherry, Suzanne L. Topalian, Nicholas P. Restifo, Richard E. Royal, Udai Kammula, Donald E. White, Sharon A. Mavroukakis, Linda J. Rogers, Gerald J. Gracia, Stephanie A. Jones, David P. Mangiameli, Michelle M. Pelletier, Juan Gea-Banacloche, Michael R. Robinson, David M. Berman, Armando C. Filie, Andrea Abati, and Steven A. Rosenberg. Adoptive cell transfer therapy following non-myeloablative but lymphodepleting chemotherapy for the treatment of patients with refractory metastatic melanoma. *Journal of Clinical Oncology*, 23(10):2346–2357, 2005.

[95] María Sancho-Albero, Nazeeha Ayaz, Victor Sebastián, Cristina Chirizzi, Miguel Encinas-Gimenez, Giulia Neri, Linda Chaabane, Lluís Luján, Pilar Martin-Duque, Pierangelo Metrangolo, Jesús Santamaría, and Francesca Baldelli Bombelli. Superfluorinated extracellular vesicles for in vivo imaging by ^{19}f-MRI. *ACS Applied Materials & Interfaces*, 15(7):8974–8985, 2023.

[96] Pietro Milesi, Beatrice Lucia Bona, Cristina Chirizzi, Marco Campanile, Pompea Del Vecchio, Marc Schmutz, Valerie Sartor, Debora Berti, Pierangelo Metrangolo, Francesca Baldelli Bombelli, and Barbara Lonetti. PERFECTA loaded lipid cubosomes for ^{19}f-MRI: Physico-chemical characterization. *Chemistry – A European Journal*, 2026.

[97] Nazeeha Ayaz, Valentina Dichiarante, Claudia Pigliacelli, Jacopo Repossi, Lara Gazzera, Marta Boreggio, Daniele Maiolo, Cristina Chirizzi, Greta Bergamaschi, Linda Chaabane, Elisa Fasoli, Pierangelo Metrangolo, and Francesca Baldelli Bombelli. Hydrophobin-coated solid fluorinated nanoparticles for ^{19}f-MRI. *Advanced Materials Interfaces*, 9(18):2101677, 2022.

[98] Dina V. Hingorani, Fanny Chapelin, Emma Stares, Stephen R. Adams, Hideho Okada, and Eric T. Ahrens. Cell penetrating peptide functionalized perfluorocarbon nanoemulsions for targeted cell labeling and enhanced fluorine-19 MRI detection. *Magnetic Resonance in Medicine*, 83(3):974–987, 2020.

[99] Ting Mao, Xufeng Xu, Pamina M. Winkler, Cécilia Siri, Ekaterina Poliukhina, Paulo Jacob Silva, Nan Xu, Yu Hu, Karim Al Zahabi, Rémi La Polla, Zhi Luo, Quy Ong, Alfredo Alexander-Katz, and Francesco Stellacci. Stabilizing effect of amino acids on protein and colloidal dispersions. *Nature*, 645(8082):915–921, 2025.

Acknowledgements

Arrivare alla fine di questo percorso mi porta a guardare indietro con gratitudine e con un'emozione che va oltre le parole scritte in queste pagine. Ogni esperimento, ogni dubbio e ogni piccola scoperta portano con sé il calore di chi mi ha accompagnata, giorno dopo giorno, in un viaggio che è stato molto più di una tesi di laurea.

Desidero ringraziare innanzitutto la **prof.ssa Francesca Baldelli Bombelli**, che mi ha offerto l'opportunità di intraprendere questo percorso di ricerca su un progetto per me di grande interesse. La sua fiducia ha aperto davanti a me porte che non immaginavo, e in ogni momento ha saputo accogliere e comprendere la mia passione per la ricerca con generosità e supporto costante fin dall'inizio.

Un ringraziamento speciale va alla **Dr. Cristina Chirizzi**, che mi ha visto crescere giornalmente in questo percorso. Mi ha accolto nel progetto, mi ha insegnato un mestiere e con pazienza me ne ha trasmesso l'entusiasmo. Ti ringrazio per essere stata molto più di una supervisore, una collega e un'amica con cui condividere ogni momento lavorativo, ogni pausa, pranzi e anche gite in macchina. Ti ringrazio per avermi inclusa in progetti che andavano oltre ciò che la laurea avrebbe richiesto, e per aver visto quella luce che muove la mia passione per la ricerca. Ti ringrazio per aver creduto in me e per avermi aiutata a guardare al mio futuro. Per tutto questo, grazie di cuore.

Ringrazio la **prof.ssa Serena Pellegatta** per avermi ospitata nel suo laboratorio e per avermi guidata scientifica in ogni fase del percorso.

Un grazie immenso va a Martina P., Martina M., Manuela, Manuel, Valentina, Andrea, Silvia, Chiara, Giulia, Carlotta e Alessia, che hanno reso questi mesi un'esperienza memorabile. Per ogni mio dubbio hanno lasciato da parte le proprie attività per sostenermi, senza mai far pesare la richiesta. Mi hanno offerto supporto tecnico e, nei pochi minuti di pausa, quelle chiacchiere che sapevano ricaricare le energie. Con gentilezza mi hanno aperto le porte delle loro attività, permettendomi di imparare e osservarli nei momenti liberi dal mio progetto: piccoli doni di tempo e di cura che custodirò per sempre.

Ringrazio Domenico ed Elena, per aver visto il mio impegno sin dal Capstone Project e avermi messa in contatto con questa opportunità, vedendo la luce della passione che nutro per la ricerca. Vi ringrazio, insieme a Riccardo, Alice, JP, Duzzo, Anna, Giuseppe, Lorenzo, Agostino per aver reso le giornate laorative piu leggere, per

ogni pranzo condiviso, per il caffe al 7 tesla che rigenera lo spirito. Custodirò nel mio cuore ognugno di questi piccoli momenti. Un ringraziamento speciale va a Federica. In te ho ritrovato delle parti molto simili di me e la tua empatia e semplicità mi ha colpito molto. Ti ringrazio per essere stata il primo sguardo aprendo la porta dell'ufficio e spesso l'ultimo della giornata. Completerò i proverbi riservando un bellissimo ricordo dei tuoi.

Ringrazio Benedetta e il Dr. Renzo Vanna, per il supporto con le misurazioni Raman e per avermi inclusa nel loro progetto.

A tutti voi va la mia più sincera gratitudine: avete trasformato la ricerca in un'avventura condivisa, e questo lavoro porta il vostro segno in ogni sua pagina.